

# Transparent Antennas for Indoor Communications



**Yu Yao**

Department of Electronic and Electrical Engineering  
University of Sheffield

Supervisors: Prof. Jie Zhang, Prof. Xiaoli Chu

This thesis is submitted for the approval of the  
*Doctor of Philosophy*

February 2023



*Dedicated to my beloved family.*

Without their unconditional love, support and encouragement,  
I would not be the person I am today.



## **Acknowledgements**

I would like to show my best appreciation to my supervisor, professor Jie Zhang, for the powerful aid in academic research and consistent guidance on my life. His cultivation concepts of integrity, endeavour and critical thinking have pivotal influence on my doctoral career.

I would like to show my special gratitude to Dr. Yu Shao and Dr. Jiliang Zhang for their selfless guidance and advice on my project. They carried me through every stage with their persistent motivation, enthusiasm and immense knowledge.

I would like to express my sincere gratitude to my family for their love, encouragement and accompany. Without their support, I would not possible to complete my Ph.D.

Addition grateful to all colleagues in our group who gave me many supports in the past three years.



## **Abstract**

The explosive growth of indoor traffic requires evolved wireless equipment. Smart cities and homes led by the 5G and beyond urgently need densely distributed indoor base stations (BSs). However, the current antennas for indoor deployment rarely consider integration with the environment. To integrate multi-function for various applications, indoor BSs will inevitably increase in size. To avoid the inconvenience caused by the indoor BSs in a limited space, using transparent antennas (TAs) suitable for indoor communication to improve space utilisation and reduce visual crowding is optimal. In the thesis, six TAs using different materials or mechanisms are designed and verified. Firstly, the glass-integrated antenna sandwiched by double-layer glass achieves triple band resonances for GSM, WLAN and 5G low-frequency band. Secondly, the 4-element MM TA array achieves high gain and high efficiency at 2.4 GHz. Thirdly, a 4-element wired MM TA firstly achieves ultra-wideband (UWB) and multiple-input multiple-output (MIMO). A parasitic decoupling structure for the MM antenna is proposed. The antenna achieves high isolation and comparable gain and efficiency to the conventional metal antenna while achieving high transparency. Fourthly, a UWB MIMO TA using transparent conductive film (TCF) is designed with low coupling. Fifthly, a double-layer Fabry-Perot cavity (FPC) TA achieves breakthrough high gain and efficiency of TCF antennas. Finally, the first all-dielectric transparent lens (ADTL) antenna is proposed. The lens uses the mechanism of the optic that can provide adjustable beamforming according to indoor environment needs, including gain enhancement, flat-top beam and dual beam. This thesis comprehensively demonstrates the research methods of various TAs, verifies the feasibility and provides strong guidance for the application of commercial TAs in the future.



# List of Publications

## Published

- [1] **Y. Yao**, Y. Shao, J. Zhang and J. Zhang, "A transparent antenna using metal mesh for UWB MIMO applications," *IEEE Trans. Antennas Propag.*, Feb. 2023, accepted.
- [2] **Y. Yao**, Y. Shao, J. Zhang and J. Zhang, "UWB MIMO optical transparent antenna based on ITO film," *IEICE Electronics Express (ELEX)*, Feb. 2023, accepted.
- [3] **Y. Yao**, B. Wu, Y. Shao, J. Zhang and J. Zhang, "CPW-fed transparent antenna array using metal mesh," *2023 Eur Conf Antennas Propag. (EUCAP)*, Mar. 2023.
- [4] **Y. Yao**, Y. Shao, J. Zhang and J. Zhang, "Design of glass-integrated grid antenna using CMA for multiband indoor network," *2020 Int. Sym. Antenna Propag. (ISAP)*, pp. 201-202, Jan. 2021. doi: 10.23919/ISAP47053.2021.9391314.

## Submitted

- [5] **Y. Yao**, Y. Shao, J. Zhang and J. Zhang, "High Efficiency and High Gain Indium Tin Oxide Transparent Antenna Based on Fabry-Perot Cavity," submitted to *IEEE Trans. Antennas Propag.*.
- [6] **Y. Yao**, Y. Shao, J. Zhang and J. Zhang, "Dielectric Cosinusoidal Transparent Lens Antenna For Beamforming," submitted to *AEU - International Journal of Electronics and Communications*.



# Table of contents

<b>List of Publications</b>	<b>ix</b>
<b>List of figures</b>	<b>xv</b>
<b>List of tables</b>	<b>xxi</b>
<b>Abbreviations</b>	<b>xxiii</b>
<b>1 Introduction</b>	<b>1</b>
1.1 Background . . . . .	2
1.1.1 Indoor Communication Environment . . . . .	2
1.1.2 Indoor Antenna Technologies . . . . .	4
1.2 Objectives . . . . .	8
1.3 Contributions . . . . .	9
1.4 Organisation . . . . .	10
<b>2 Literature Review</b>	<b>13</b>
2.1 Material-Integrated Antennas . . . . .	13
2.1.1 Embedded Antennas . . . . .	13
2.1.2 Glass-Integrated Antennas . . . . .	15
2.2 Transparent Antennas . . . . .	17
2.2.1 Transparent Conducting Films . . . . .	18
2.2.2 TCF Antennas . . . . .	21
2.2.3 Micro MM Antennas . . . . .	25

2.2.4	Wired MM Antennas . . . . .	29
2.2.5	TCFs and MM Comparison . . . . .	31
2.3	Transparent Metasurfaces . . . . .	32
2.3.1	Conductive Metasurfaces . . . . .	35
2.3.2	Dielectric Metasurfaces . . . . .	37
2.4	Summary . . . . .	38
<b>3</b>	<b>Metal Mesh Antennas</b>	<b>39</b>
3.1	Glass-integrated Antenna Using CMA for Multiband Indoor Network . . . . .	40
3.1.1	Introduction . . . . .	40
3.1.2	Feeding Refinement and Glass Integration . . . . .	47
3.1.3	Conclusion . . . . .	49
3.2	CPW-Fed TAA Using Wired MM . . . . .	49
3.2.1	Introduction . . . . .	49
3.2.2	Antenna Design . . . . .	50
3.2.3	Transparent Treatment of the Antenna Array . . . . .	53
3.2.4	Results and Discussion . . . . .	55
3.2.5	Conclusion . . . . .	57
3.3	A Transparent Antenna Using Metal Mesh for UWB MIMO Applications . . . . .	57
3.3.1	Introduction . . . . .	57
3.3.2	Element Design . . . . .	58
3.3.3	Array Design . . . . .	62
3.3.4	Results and Discussion . . . . .	66
3.3.5	Conclusion . . . . .	75
<b>4</b>	<b>TCF Antennas</b>	<b>77</b>
4.1	UWB MIMO Optical Transparent Antenna Based on ITO film . . . . .	78
4.1.1	Introduction . . . . .	78
4.1.2	Antenna Design . . . . .	78
4.1.3	Simulation and Measurement Results . . . . .	80

---

4.1.4	Conclusions . . . . .	83
4.2	High Efficiency and High Gain ITO TA Based on Fabry-Perot Cavity . . . .	84
4.2.1	Introduction . . . . .	84
4.2.2	Transparent FPC Antenna Design . . . . .	85
4.2.3	Results and Discussion . . . . .	93
4.2.4	Conclusion . . . . .	98
<b>5</b>	<b>All-Dielectric Transparent Lens Antenna</b>	<b>99</b>
5.1	Introduction . . . . .	99
5.2	Cosinusoidal Lens Mechanism . . . . .	101
5.3	ADTLs Antenna Design . . . . .	103
5.3.1	Feeding Antenna . . . . .	103
5.3.2	ADTL 1 . . . . .	104
5.3.3	ADTL 2 . . . . .	105
5.3.4	ADTL 3 . . . . .	106
5.4	Experiment Results . . . . .	107
5.5	Conclusion . . . . .	113
<b>6</b>	<b>Conclusions and Future Work</b>	<b>115</b>
6.1	Conclusions . . . . .	115
6.2	Future Work . . . . .	117
<b>A</b>	<b>Matlab Code for CMA</b>	<b>121</b>
A.1	Main Function of Sweeping Modes for Specific Band . . . . .	121
A.2	Function ATWSTraightWireTriangle For MoM Using Triangle Function . .	122
A.3	Function CM for Characteristic Mode Algorithm . . . . .	127
A.4	Function Normalise For Modes Normalisation . . . . .	128
A.5	Function Tracking For Mode Tracking . . . . .	128
	<b>References</b>	<b>131</b>



# List of figures

1.1	Deployment of indoor BSs including embedded BS, on-glass transparent BS and on-wall BS. . . . .	6
2.1	(a) Microstrip patch embedded in concrete model [10], (b) microstrip antenna sensor for moisture monitoring [13]. . . . .	14
2.2	Wideband MIMO embedded antennas on vehicle roof [16]. . . . .	15
2.3	(a) FM vehicle antenna based on defroster lines [17], (b) 5G vehicle antenna [21]. . . . .	16
2.4	(a) Antenna for wearable glasses [22], (b) reconfigurable slot antenna for wearable glasses [23]. . . . .	17
2.5	Skin depth comparison of TCFs and MM at different frequencies [26]. . . . .	19
2.6	The optical transparency versus film thickness with different carrier concentrations [25]. . . . .	21
2.7	Wideband MIMO TA, (a) geometry of antenna element, (b) simulated and measured reflective coefficient, (c) geometry and prototype of the MIMO antenna, (d) measured $S$ -parameter of the TA [40]. . . . .	22
2.8	UWB MIMO TA for automotive, (a) geometry and prototype, (b) TA mounted on the windshield. [41]. . . . .	24
2.9	(a) TA array using copper doped ITO film [44], (b) TA array using Ag doped ITO film [45]. . . . .	25

2.10	(a) Ideal micro MM for fill factor definition, (b) PVD processed micro MM under the microscope [22], (c) photograph of diamond mesh structure fabricated by Ag-alloy etching ( $W_{\text{ver}}=100 \mu\text{m}$ , $W_{\text{hor}}=50 \mu\text{m}$ and $W_{\text{mesh}}=3 \mu\text{m}$ ) [52]. . . . .	26
2.11	(a) Antenna-on-display for mobile phone, (b) $1 \times 8$ TA array with multilayer feeding structure [52], (c) geometry and (d) prototype of the MIMO TA in [53].	27
2.12	(a) The geometry of the element and the prototype of the TA array in measuring environment [59], (b) isometric view of the wired MM TA attaching to the solar cells with covered glass [60], (c) TA using meshed structure for vehicle applications, (d) a triple-band TA. . . . .	30
2.13	The reported TAs using TCFs or micro MM, where $\phi_{TC}$ denotes the figure-of-merit [26]. . . . .	31
2.14	(a) The working pattern of the reflectarray, (b) the prototype under the experiment [93], (c) the metasurface prototype and measuring environment [94], (d) prototype of the transparent transmitarray [95]. . . . .	35
2.15	(a) The element and metasurface geometry [108], (b) prototype and its H-plane radiation pattern at 5.8 GHz [109]. . . . .	37
3.1	Normalised current distribution on grid antenna, (a), (b) and (c) represent the current distributions of mode 1, mode 2 and mode 3 at their resonance frequencies . . . . .	45
3.2	Overall version of antenna design that is integrated within the glass pieces, where $a = 28 \text{ mm}$ , $b = 23 \text{ mm}$ , $c = 17.4 \text{ mm}$ and $L = 2a$ , the thickness of glass is $t = 5 \text{ mm}$ , the gap is $g = 3 \text{ mm}$ and the radius of the wires is $r = 0.3 \text{ mm}$ . (a) is the front view and (b) is the right view. . . . .	46
3.3	(a) MS of mode 1 in Figure 3.2(a) with different size of the outer frame, (b) triple-band resonance performance in free space. The side lengths of each grid in the antenna are $a = 45 \text{ mm}$ , $b = 34 \text{ mm}$ and $c = 24 \text{ mm}$ . . . . .	47
3.4	The reflective coefficient ( $S_{11}$ ) of the antenna in free space and integrated with glass. . . . .	48

3.5	Radiation patterns of the glass-integrated antenna at the resonance frequencies of 1.8 GHz, 2.4 GHz and 3.5 GHz at (a) $yz$ -plane and (b) $xz$ -plane . . .	49
3.6	(a) The top view of the CPW-fed antenna unit where $l_1=21$ mm, $l_2 =16$ mm, the gap $d_1 = d_2=7.5$ mm, $d_3 =7$ mm, $g_1=0.9$ mm and the feed line width $w_1=1$ mm, (b) the reflective coefficients of antenna unit and opaque antenna array.. . . . .	51
3.7	The top view of the CPW-fed antenna array where $g_2=0.5$ mm, $w_2=7$ mm, $g_3=0.3$ mm, $w_3=12$ mm, $g_4=0.9$ mm, $w_4=5$ mm and the units distance $d_4=44$ mm. Stage 1, 2 and 3 are the impedance matching stages. . . . .	52
3.8	The current distribution of opaque antenna array. . . . .	52
3.9	The processes of the transparency treatment. (a) is the cut antenna array, (b) applying large meshes on the ground plane, (c) applying small meshes on feed line and (d) slotting on patches. . . . .	53
3.10	(a) The resonant performance of the antenna array while doing the transparent processes. The Step 1, 2, 3 and 4 correspond to the models in Fig. 3.9 (a), (b), (c) and (d), (b) the gain and radiation efficiency of the solid antenna and TAA. . . . .	55
3.11	The radiation patterns: (a) the original CPW-fed antenna array, (b) the final version of the TAA. . . . .	56
3.12	The CPW-fed UWB element and its current distribution at 4 GHz: (a) opaque element, (b) current distribution of opaque element. . . . .	59
3.13	The transparent processing steps: (a) step 1, (b) step 2, (c) step 3 is the final version of UWB transparent element. (d) is current distribution of the transparent element. . . . .	59
3.14	The reflective coefficients of the opaque, Step 1, Step 2 and transparent element corresponding to Fig. 3.12(a), Fig. 3.13(a), (b) and (c). . . . .	60
3.15	Geometry of the proposed UWB MIMO TA: (a) front view, (b) rear view. The detail dimension is presented in Table 3.2. Grey and orange colour represent metal and FR-4 substrate, respectively. . . . .	61

3.16	The evolution of the connection and decoupling structure. (a) is the front view, (b), (c) and (d) are the rear view. (a) to (b) is the element connection optimisation and (b), (c) and (d) are the parasitic decoupling structure optimisation with their current distribution at 4 GHz. . . . .	63
3.17	$S$ -parameters of the antenna evolution shown in Fig. 3.16. . . . .	64
3.18	Current distributions on the MIMO antenna when Element 1 is excited at 3.5 GHz: (a) initial structure, (b) final structure. . . . .	65
3.19	The prototype of the proposed antenna: (a) front view, (b) rear view. . . . .	66
3.20	The simulated and measured $S$ -parameter of the proposed UWB MIMO TA. . . . .	67
3.21	The simulated and measured radiation patterns: (a) x-z plane at 4 GHz, (b) y-z plane at 4 GHz, (c) x-z plane at 7 GHz, (d) y-z plane at 7 GHz, (e) x-z plane at 10 GHz, (f) y-z plane at 10 GHz. . . . .	68
3.22	Measured $S$ -parameter and picture of the UWB MIMO TA attached to an indoor window. . . . .	69
3.23	The gain and radiation efficiency of the proposed antenna. . . . .	70
3.24	(a) MEG of Element 1, where $M_1$ and $M_2$ are based on Gaussian for elevation and uniform for azimuth with 0 and 6 dB XPR, $M_3$ and $M_4$ are based on isotropic environment with 0 and 6 dB XPR, (b) Ratio between MEGs at $XPR = 6$ dB, where $R_1$ and $R_2$ are obtained by $ MEG_1/MEG_2 $ and $ MEG_1/MEG_3 $ using Gaussian for elevation and uniform for azimuth, while $R_3$ and $R_4$ are obtained by $ MEG_1/MEG_2 $ and $ MEG_1/MEG_2 $ based on isotropic environment. . . . .	71
3.25	ECC and DG calculated by farfields, where $\rho_{12}$ and $DG_{12}$ represent ECC and DG between element 1 and 2, $\rho_{13}$ and $DG_{13}$ represents ECC and DG between element 1 and 3. . . . .	72
3.26	Channel capacity of the proposed MIMO TA. . . . .	73
3.27	(a) Normalised transmitted and received signal pulses at 0.5 m, (b) group delay. . . . .	74

4.1	(a) The front view of the antenna, orange represents the ITO film and blue represents the glass substrate, (b) the surface current distribution of the proposed TA, when exciting Element 1 at 7 GHz. . . . .	79
4.2	The simulated and measured S-parameter of the proposed 2×2 MIMO TA. .	80
4.3	The simulated and measured radiation patterns . . . . .	81
4.4	(a) Ratios of MEG between element $i$ and $j$ ; (b) ECC and DG. . . . .	82
4.5	Photograph of proposed antenna: (a) antenna prototype and (b) the visual effect of the TA attaching to the indoor window. . . . .	83
4.6	Schematic diagram of the proposed FPC antenna. . . . .	86
4.7	Geometry of the transparent FPC antenna. . . . .	87
4.8	(a) Geometry of the TM feed source, the dimensions are shown in Table 4.2, (b) the efficiencies of the TM with different $H_g$ . . . . .	88
4.9	Simulated and measured $S_{11}$ of TM alone. . . . .	89
4.10	The unit cell of top PRS, (a) geometry, (b) current distribution at 5.6 GHz. .	90
4.11	S-parameter of the unit cell on top PRS with different dimensions, (a) magnitude, (b) phase. . . . .	90
4.12	S-parameter of the unit cell on bottom PRS. . . . .	91
4.13	Current distributions of the bottom cell at (a) 4.9 GHz and (b) 6.3 GHz. . .	92
4.14	Prototypes of the antenna, (a) components, (b) transparency comparison. . .	93
4.15	$S_{11}$ of the FPC TA assembled together. . . . .	94
4.16	Simulated and measured gains of the TM alone and the FPC TA. . . . .	94
4.17	Efficiencies of the TM alone and the FPC TA. . . . .	94
4.18	Normalised radiation pattern: (a) E-plane at 4.9 GHz, (b) H-plane at 4.9 GHz, (c) E-plane at 5.6 GHz, (d) H-plane at 5.6 GHz, (e) E-plane at 6.3 GHz, (f) H-plane at 6.3 GHz. . . . .	96
5.1	The 3-D geometry of the dielectric ADTL. . . . .	102
5.2	The geometry of transparent monopole feeding antenna, the dimension is shown in Table I. . . . .	103

5.3	(a) Ray tracing schematic diagrams of ADTL 1 ( $A = 26$ mm and $k = 0.33$ ) at 6 GHz. Red, pink and blue zones denote the radiation intensity of the beam from strong to weak and the thin black lines represent the rays. (b) Electric field distribution on $xz$ -plane of ADTL 1. . . . .	104
5.4	(a) Ray tracing schematic diagrams of ADTL 2 ( $A = 20$ mm and $k = 0.7$ ) at 6 GHz, (b) electric field distribution on $xz$ -plane of ADTL 2. . . . .	105
5.5	(a) Ray tracing schematic diagrams of ADTL 3 ( $A = 30$ mm and $k = 2$ ) at 6 GHz, (b) electric field distribution on $xz$ -plane of ADTL 3. . . . .	106
5.6	The prototypes of (a) ADTL 1, (b) ADTL 2 and (c) ADTL 3. (d) The measurement setup and TM prototype. (e) The application on spotlight. . .	107
5.7	(a) The reflective coefficients of the proposed antenna, (b) radiation efficiencies of feeding and with ADTLs. . . . .	108
5.8	Radiation pattern of ADTL 1 and feeding antenna at (a) 5.6 GHz, (b) 6 GHz and (c) 6.4 GHz. (d) The gains of feeding antenna and with ADTL 1 . . . .	109
5.9	Radiation patterns of ADTL 2 at (a) 5.6 GHz, (b) 6 GHz and (c) 6.4 GHz. .	110
5.10	(a) Dual-beam radiation patterns of ADTL 3a ( $A = 28$ mm and $k = 1$ ), ADTL 3b ( $A = 15$ mm, $k = 1.5$ ) and ADTL 3 ( $A = 30$ mm and $k = 2$ ) at 6 GHz. Simulated and measured radiation pattern of ADTL 3 at (b) 5.6 GHz, (c) 6 GHz and (d) 6.4 GHz. . . . .	111
6.1	The relationship between the chapters. . . . .	117

# List of tables

2.1	MATERIAL PROPERTIES OF THE INVESTIGATED TCOS [27, 37–39]	20
3.1	COMPARISONS OF TRANSPARENT ANTENNAS . . . . .	56
3.2	DIMENSIONS OF THE PROPOSED ANTENNA . . . . .	61
3.3	COMPARISON OF TRANSPARENT MIMO ANTENNAS . . . . .	75
4.1	COMPARISON OF TCF MIMO ANTENNAS . . . . .	83
4.2	DIMENSIONS OF THE PROPOSED FPC TA . . . . .	88
4.3	COMPARISONS OF HIGH EFFICIENCY AND HIGH GAIN TA . . . . .	97
5.1	DIMENSIONS OF THE TRANSPARENT MONOPOLE . . . . .	103
5.2	COMPARISONS OF SIMILAR DESIGNS . . . . .	112



# Abbreviations

**2G** The second-generation

**3-D** 3-dimension

**3G** The third-generation

**4G** The fourth-generation

**5G** The fifth-generation

**ADTL** All-dielectric transparent lens

**AZO** Al-doped ZnO

**BS** Base station

**CM** Characteristic modes

**CMA** Characteristic modes analysis

**CPW** Co-planar waveguide

**DG** Diversity gain

**ECC** Envelop correlation coefficient

**EFIE** Electric field integral equation

**EM** Electromagnetic

**EMI** Electromagnetic interference

**FP** Fabry-Perot

**FPC** Fabry-Perot cavity

**FSS** Frequency selective surface

**FTO** Fluorine-doped tin oxide

**GSM** Global system for mobile communications

**GZO** Ga-doped ZnO

**ITO** Indium-doped tin oxide

**LoS** Line-of-sight

**LSAA** Large scale antenna array

**MEG** Mean effective gain

**MIMO** Multiple-input multiple-output

**MM** Metal mesh

**mmWave** Millimetre wave

**MoM** Method of moment

**MS** Model significance

**O2I** Outdoor-to-indoor

**PRS** Partially reflective surface

**PVD** Physical vapor deposition

**RCS** Radar cross section

**RF** Radio frequency

**RIS** Reconfigurable intelligent surface

**RWG** Rao-Wilton-Glisson

**SLA** Stereolithography

**TA** Transparent antenna

**TAA** Transparent antenna array

**TCF** Transparent conducting film

**TCO** Transparent conductive oxide

**THz** Terahertz

**TM** Transparent monopole

**UWB** Ultra-wideband

**V2I** Vehicle-to-infrastructure

**V2P** Vehicle-to-pedestrian

**V2V** Vehicle to vehicle

**WLAN** Wireless local area network

**XPR** Cross-polarization power ratio

**ZnO** Zinc oxide



# Chapter 1

## Introduction

Wireless mobile traffic has experienced exponential growth in the last few decades. More than 80% of mobile traffic will take place indoors. Wireless strategies are constantly evolving to satisfy the requirements of signal coverage and capacity of indoor communication. The second and third generations (2G and 3G) cover indoor mobile networks by connecting outdoor cellular radio towers. In the fourth generation (4G), multi-operators with increasing base stations (BSs) strengthen the outdoor to indoor transmission and compensate for the indoor signal coverage. In the fifth generation (5G) and beyond higher frequency networks, massive multiple-input multiple-output (MIMO), beamforming and reconfigurable intelligent surface (RIS) are widely studied to address increased path loss and weakened penetration. Especially in the indoor environment, signals are significantly reduced by extensively distributed indoor barriers, such as glass, concrete wall and metal structures. Indoor BSs densification is essential to promote 5G and beyond development. However, using traditional high-performance antenna arrays to construct desirable BSs will inevitably occupy considerable space. In the future smart buildings, densely deployed indoor BSs will face severe space limitations and aesthetic challenges. Thus, the antennas can be integrated into building structures must be investigated [1].

The current antenna designs mainly focus on their own performance while ignoring the combination of the building environment. To be integrated into buildings, the antenna should have the physical characteristic of concealment. A direct way is by making the antenna

transparent. In this thesis, transparent antennas (TAs) using the technologies of grid wires, metal mesh (MM), transparent conducting films (TCFs) and transparent dielectric materials are illustrated. This chapter presents the background of indoor communications, proposes the objectives and summarises the contributions.

## **1.1 Background**

### **1.1.1 Indoor Communication Environment**

As the revolution speed of wireless communication far exceeds the architectural updating, buildings that ignore the communication "friendly" are restricting wireless communication. Indoor wireless environments present a unique set of challenges that can significantly limit the development and performance of indoor antennas. In indoor environments, wireless signals often bounce off walls, ceilings, and other objects, creating multiple paths for the signal to reach the receiver. This phenomenon is known as multipath propagation. Multipath can lead to signal interference, phase cancellation, and reduced signal strength, making it difficult for antennas to effectively receive and transmit signals. The various structures like walls, floors, and furniture can attenuate wireless signals as they pass through. Different materials have varying levels of signal absorption and reflection, leading to signal loss and reduced coverage. These obstacles can also create areas of shadow where wireless signals struggle to penetrate. These shadowed areas result in dead zones where the signal strength is very weak or non-existent. Indoor environments are dynamic; they can change over time due to rearrangement of furniture, addition of new obstacles, and changes in building materials. This makes it challenging to design antennas that consistently perform well under varying conditions. Wireless communication technologies have evolved significantly to cater to the increasing demand for high-speed and reliable connectivity in indoor environments.

Small base stations have gained prominence as a solution to address the challenges of indoor coverage and capacity. Researchers have explored various deployment strategies, interference management techniques, and optimization algorithms for small cell networks in indoor scenarios. Small cells enhance network capacity by offloading traffic from macro

cells and improving signal quality within confined spaces. Research has focused on topics such as energy efficiency, dynamic spectrum allocation, and self-organizing networks for small base stations in indoor environments. Techniques like cooperative communication and hybrid architectures integrating macro and small cells have been investigated to achieve seamless connectivity and efficient resource utilization indoors.

MIMO technology has revolutionized wireless communication by exploiting spatial diversity to enhance data rates and reliability. In indoor settings, researchers have explored advanced MIMO techniques such as massive MIMO to provide high-capacity links for multiple users simultaneously. The integration of MIMO with beamforming and spatial multiplexing has been a subject of study to mitigate interference and improve indoor coverage. Studies have delved into the design of optimal antenna configurations, channel modeling, and interference management for MIMO systems in indoor environments. Hybrid MIMO architectures that combine traditional antenna arrays with smart antennas and RIS elements have been proposed to further enhance indoor communication performance.

RIS have emerged as a promising technology to manipulate wireless propagation by reflecting and modifying incident waves. In indoor scenarios, RIS can be deployed on walls or ceilings to enhance coverage, extend range, and improve signal quality. Research has investigated RIS-assisted communication techniques, such as beamforming optimization, channel estimation, and resource allocation. The application of machine learning and optimization algorithms to exploit the capabilities of RIS in indoor environments has garnered attention. RIS not only complements MIMO systems but also introduces new dimensions to indoor wireless communication design. In addition, as the windows and building materials will cause large penetration loss for an outdoor-to-indoor (O2I) signal, RIS has been proposed to solve the O2I problem [2]. They need to be installed on the exterior wall or windows, which will greatly affect the aesthetics of the building. When faced with low-strength received signals and complex indoor environments, RIS cannot effectively enhance indoor coverage.

Antenna design plays a critical role in achieving reliable connectivity and efficient spectrum utilization indoors. Researchers have explored compact, low-profile antenna designs suitable for indoor environments with limited space constraints. Multi-band and

wideband antennas have been studied to cater to diverse frequency bands used in indoor communication. Studies have also investigated diversity antennas and their impact on indoor channel characteristics. Novel materials and structures, such as metamaterials and printed antennas, have been considered to enhance antenna performance and mitigate interference in cluttered indoor environments.

The evolution of wireless communication technologies has led to significant advancements in providing robust connectivity in indoor settings. High-performance equipment leads to occupy interior space and damage to aesthetics. In a prosperous city, every inch of land has been exhausted, which is hard to divide space for these devices. To maximize the coverage of high-speed communications using them, the space problem should be overcome.

### 1.1.2 Indoor Antenna Technologies

Indoor antennas hold immense significance in indoor wireless communication by optimizing signal penetration, coverage, and strength within confined spaces. They play a pivotal role in minimizing interference, harnessing spatial diversity, and enhancing capacity through technologies like MIMO. By ensuring reliable connections, they elevate user experience, enable internet of thing applications, support private networks, and facilitate location-based services. The current indoor antennas are mainly based on printed patch antennas with opaque conductive materials and substrates. In [3], the current indoor antennas are categorised into linearly polarized nonplanar indoor antennas, circularly polarized nonplanar indoor antennas, and broadband circularly polarized printed slot antennas.

**1). Linearly polarized nonplanar indoor antennas:** They represents a departure from traditional planar antennas, leveraging nonplanar geometries to enhance performance. By introducing curvature or other nonplanar shapes, these antennas can achieve unique radiation patterns and gain characteristics. Such designs are advantageous in indoor environments where signal reflections and multipath propagation are prevalent. They exhibit improved spatial diversity, making them suitable for mitigating multipath fading and enhancing signal reliability [4]. Moreover, their nonplanar structure allows for versatile installation on curved surfaces, ceilings, and walls. These antennas find application in environments where planar

antennas may not provide optimal coverage, making them a promising solution for demanding indoor scenarios. [4–6] gives three nonplanar prototypes for indoor communications.

**2). Circularly polarized nonplanar indoor antennas:** They build upon the advantages of nonplanar designs while introducing circular polarization, which is beneficial for mitigating the effects of polarization mismatch and improving signal quality. Circular polarization ensures that the antenna's reception is less susceptible to polarization changes caused by reflections and object orientations in indoor spaces. This property is especially important in environments with a high degree of signal scattering. Circularly polarized nonplanar antennas find utility in applications where consistent signal reception and transmission are crucial, such as indoor positioning systems, RFID applications, and wireless sensor networks [7, 8].

**3). Broadband circularly polarized printed slot antennas:** They address the challenge of achieving wide bandwidth and circular polarization simultaneously. These antennas utilize slot structures etched onto a substrate, enabling broadband performance by exciting multiple resonant modes. The incorporation of circular polarization enhances the antenna's robustness against interference and polarization mismatch, ensuring reliable connectivity [9]. These antennas are particularly suitable for indoor environments where a wide range of frequencies is used and where circular polarization can enhance the antenna's immunity to multipath fading. Applications include wireless communication systems, Wi-Fi networks, and indoor wireless backhaul solutions.

The indoor coverage can be addressed, however, using them as a part of indoor small BSs will occupy large spaces and negatively affect visual impact. The spatial isolation between the elements in an antenna array will be deteriorated by simply reducing the space intervals to less than half wavelength. Using covert antenna arrays to replace LSAA for indoor BSs is a promising approach. Thus, antenna arrays should be able to combine with building structures and reduce occupied space and visual impact. Fig. 1.1 shows the deployment of indoor BSs with embedded, integrated or attached antenna arrays. The transparent BSs with TA elements can be attached to the surface of windows and walls. The array for embedded BS relies on the steel fibres in the concrete wall. Using TAs in indoor applications is essential

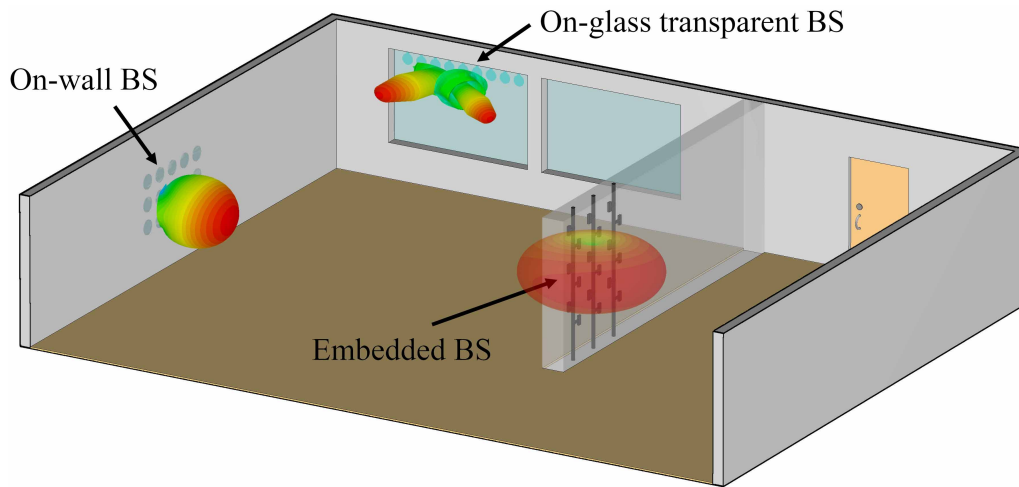


Fig. 1.1 Deployment of indoor BSs including embedded BS, on-glass transparent BS and on-wall BS.

due to their capacity to seamlessly blend with architectural aesthetics and preserve natural lighting, making them ideal for modern offices, retail spaces, and smart homes. These antennas minimise interference with interior layouts, ensure compatibility with other wireless devices, and address privacy concerns, while also future-proofing indoor environments. With their architectural flexibility, user experience enhancement, and ability to integrate into surfaces, TAs offer an unobtrusive yet efficient solution that harmonizes design and wireless connectivity in indoor spaces. Compared with TAs, the traditional indoor antennas have serious constraints on indoor communication development as follows.

Compared to TAs, traditional opaque indoor antennas impose several serious constraints on indoor communication development as follows. The solutions offered by TAs are illustrated.

**1). Aesthetic disruption:** Opaque indoor antennas, often characterized by bulkier and less visually appealing designs, disrupt the aesthetics of indoor spaces by clashing with architectural elements and obstructing sightlines. This compromises the overall design harmony and can be especially undesirable in modern and aesthetically-conscious environments. TAs seamlessly blend with the architectural design of indoor spaces, preserving the visual harmony without disrupting aesthetics. They can be integrated into windows, glass panels, and surfaces, ensuring a cohesive and unobtrusive appearance.

**2). Light obstruction:** Opaque antennas can block natural light and impede the passage of light through windows and transparent surfaces, leading to dimmer indoor spaces and decreased visual comfort. This limitation contradicts the preference for well-lit and inviting indoor environments. TAs allow natural light to pass through, maintaining well-lit indoor environments. By not obstructing light, they enhance the ambiance and comfort of indoor spaces, aligning with the preference for abundant natural lighting.

**3). Limited placement flexibility:** Traditional antennas require dedicated space for installation, which may not always align with the available indoor layout. This lack of flexibility can lead to challenges in optimizing interior space and hinder efficient placement for optimal signal propagation. TAs can be integrated into a variety of surfaces, enabling versatile placement without compromising interior layout. Their adaptability allows for efficient utilization of available space and optimized signal propagation.

**4). Privacy and security concerns:** The presence of conspicuous antennas can raise concerns related to privacy and security in sensitive indoor settings. Traditional antennas can be perceived as intrusive and might not align with the privacy expectations of users in locations like corporate offices, healthcare facilities, and private residences. TAs address privacy and security concerns by remaining inconspicuous, ensuring that users' expectations of privacy are respected without compromising connectivity.

**5). Compromised interior design:** Opaque antennas often necessitate compromises in interior design and layout to accommodate their size and placement requirements. This compromise can result in suboptimal arrangement of furniture, decor, and functional spaces within indoor environments. TAs offer interior design freedom by eliminating the need to compromise on layout due to antenna placement. Furniture, decor, and functional spaces can be arranged optimally without the constraints of traditional antenna structures.

**6). User experience impact:** The presence of conventional antennas in indoor settings can hinder the user experience by creating physical obstacles and visual distractions. In areas where users seek unobstructed views and interactions, such as galleries, museums, and retail spaces, the use of opaque antennas can detract from the intended immersive experience. In settings such as galleries, museums, and retail spaces, TAs contribute to a seamless and

immersive user experience by enabling unobstructed views and interactions while ensuring reliable wireless connectivity.

In conclusion, the limitations of traditional opaque indoor antennas highlight the need for innovative and adaptable solutions. TAs, with their ability to address these constraints, offer a harmonious convergence of design aesthetics, functional performance, and technological advancement in indoor communication systems. As innovative solutions, they pave the way for optimizing indoor environments to meet the demands of modern wireless communication while maintaining the integrity of indoor spaces.

## 1.2 Objectives

The motivation of the thesis is to propose several sets of antenna design methods suitable for indoor BSs. The following objectives should be achieved to promote 5G and beyond applications.

### 1). **Propose a method of designing material-integrated antennas.**

Simply embedding the antenna into the medium takes up additional space and can easily be damaged during decoration. Metal structures used in cement, glass, doors and windows are well protected. A slight transformation in the metal structures to make them capable of communication is the best solution for embedding the antennas. Based on the method, the antenna elements with different shapes can adapt to different building structures.

### 2). **Propose TAs with comparable performance to traditional antennas.**

The state of the art TAs cannot be promoted by sacrificing a lot of performance in exchange for transparency. Most of TAs using low conductivity transparent materials have very low gains and efficiencies. There has never been an antenna that integrates broadband, MIMO, transparency, high gain and high efficiency. The completion of this type of antenna can speed up the entry of indoor small BSs.

### 3). **Optimise the efficiency and gain of TA using TCFs.**

According to the characteristics of current transparent materials, better electrical conductivity will inevitably reduce the transparency of the material. A few traditional metal

antennas need to improve efficiency as their efficiency is close to 1. TA researches focus on using materials with better conductivity but ignores optimising antenna shapes to improve efficiency. To bridge the gap, this objective aims to propose high-efficiency and high-gain antennas using TCFs.

#### **4). Propose all-dielectric transparent lens (ADTL) antenna.**

The dielectric lens can transmit or reflect beams, which effectively improves indoor signal coverage. Compared with the antenna using transparent conductive materials, dielectric lens has much lower efficiency reduction. However, ADTL has not been applied on wireless communications. The current research prefers conductive lens as they are more sensitive to the electric field, while dielectric lens leave a lot of gaps. Thus, we aim to obtain a transparent dielectric lens with beamforming functions to lay the foundation for indoor BSs.

#### **5). Satisfy the common indoor communication frequency bands.**

The proposed TAs for indoor application should scatter the commonly used frequency bands indoors. GSM at 1.8 GHz, WLAN at 2.4 GHz, a low-frequency band for 5G at 3.5 GHz, Wi-Fi at 5 GHz and ultra-wideband (UWB) are important for indoor communication. It is more beneficial to design a single antenna to meet multiple frequency bands at the same time, which can to replace multiple single band traditional antennas.

## **1.3 Contributions**

By keeping exploring with firm determination according to the objectives, the contributions of the thesis are summarised as follows.

- A multiband glass-integrated antenna is proposed using characteristic modes analysis (CMA). It is the first multiband antenna based on a large metal grid structure in buildings. The antenna can be easily deployed on the explosion-proof glass interlayer. Its proposal can provide antenna design solutions for communication-friendly buildings in the future.

- A high gain and high efficiency TA array (TAA) based on wired MM and glass substrate is proposed. In the design, we analysed the effect of mesh size and density on the current and gave references to balance efficiency and transparency.
- An UWB MIMO TA based on a wired MM structure is proposed. The wired MM structure gains advantages against other types of TA in efficiency, gain and transparency. A novel and effective decoupling structure conformal to the MM is developed without degrading transparency. The feasibility of developing UWB MIMO TA based on wired MM is demonstrated.
- A 4-element TA with high transparency using indium-doped tin oxide (ITO) for UWB MIMO applications is proposed. The TA verified the feasibility of developing UWB MIMO using TCF.
- A TA integrated with an ITO based Fabry-Perot cavity (FPC) is proposed. The TA realises breakthrough high gain and high efficiency with low conductive TCF. This TA demonstrates that high transparency, high gain and high efficiency can be achieved simultaneously.
- An ADTL antenna is proposed. This is the first time that antenna theory has been applied to an ADTL. The application dramatically reduces the efficiency cost to obtain transparency. The lenses achieve beamforming functions of gain enhancement, flat-top beam and dual-beam. It can adjust the beam shape, angle and gain to a certain extent according to the needs of the environment.

## 1.4 Organisation

The rest contents of this thesis are organised as follows.

In Chapter II, the literature related to the proposed antennas in this thesis is reviewed. They include material-integrated antennas, TAs using transparent materials, micro MM and wired MM, conductive and dielectric lens.

In Chapter III, a glass-integrated antenna, a four-element TAA and a 4-element UWB MIMO TA are presented. The glass-integrated antenna is optimised by CMA to produce triple bands. The MM TAs are hollowed to wire MM from the solid shapes to obtain transparency. They have comparable gain and efficiency to conventional metal antennas.

In Chapter IV, two optical TAs using ITO films for different purposes are exhibited. An ITO TA aims to provide UWB MIMO service. Another TA demonstrates that using proper gain and efficiency enhancement methods can dramatically improve performance without changing materials.

In Chapter V, a TA with ADTLs for beamforming is proposed. The lens use the optics mechanism and are fabricated by 3-D printing.

In Chapter VI, we conclude the achievements of the thesis and give instructions on the further research direction.



# Chapter 2

## Literature Review

### Overview

This chapter surveys material-integrated antenna, TA and transparent metasurfaces that have the potential to support in-building communications. Following the objectives, firstly, the author reviews the embedded and glass-integrated antennas. Secondly, TAs using TCFs, micro MM and wired MM for various scenarios are reviewed. Finally, conductive and dielectric metasurface antennas are stated.

## 2.1 Material-Integrated Antennas

### 2.1.1 Embedded Antennas

The antenna combined with building structures has not been applied to daily communication. To support the building material integrated antenna design, the related works in concrete and soil are reviewed. Before the author proposed the concept of building material-integrated antenna, the embedded antennas were mainly used as sensors. In [10–12], the traditional antennas are embedded into concrete layers to estimate the infrastructures' health care which can replace expensive manual inspection. Fig. 2.1(a) in [10] shows a model of a microstrip patch embedded in a concrete box, where  $P = 70$  mm and  $D$  is the thickness of the concrete cover layer. A particular air gap between the concrete and the antenna is reserved to prevent

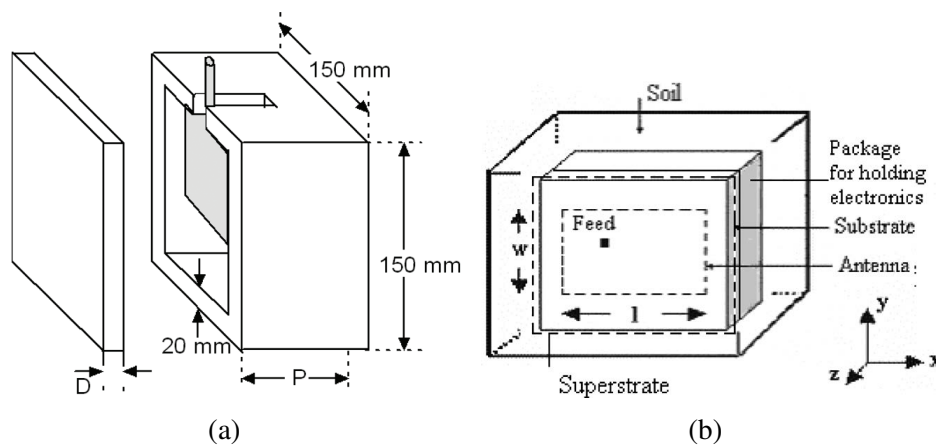


Fig. 2.1 (a) Microstrip patch embedded in concrete model [10], (b) microstrip antenna sensor for moisture monitoring [13].

a major alteration occurs in the electromagnetic characteristics of the device. The paper compares the  $S_{11}$  in free space, dry and wet concrete. Their bandwidths remain the same, but the resonant performance is reduced as the water loses over time. In [13], a microstrip antenna is buried in the soil to measure moisture. Fig. 2.1(b) shows the buried antenna model in [13]. The bandwidth and radiations can be affected by embedded depth.

The embedded sensor antennas concern more about the influence of dielectric rather than the design of the antenna itself [14, 15]. They mainly work on the very low power consumption and the stability of the resonant frequency band. They need to be embedded during construction and have difficulties in repairing if a mechanical failure occurs [10]. The effect of building materials on embedded antennas is gradual and long-term, which is a challenge for indoor wireless applications. When creating a material-integrated antenna for daily networks, the characteristics of the material need to be evaluated.

Literature [16] proposes an embedded antenna on the roof for cooperative driving. As shown in Fig. 2.2, three cavities are hollowed out from the roof's front, middle and end of the outer layer and the antennas are located in them. The antennas on the top can reduce signal blockage from low obstacles. Plenty of areas in the roof benefits spatial isolation for MIMO array, wide bandwidth and cooperative driving design. The radiation pattern of the antenna covers all the directions of the vehicle. However, the large cavities hollowed in the roof may reduce vehicle safety in a crash. In addition, the antennas are semi-embedded,



Fig. 2.2 Wideband MIMO embedded antennas on vehicle roof [16].

which will be affected by a strong wind, heavy rain and snow while driving. For a practical embedded antenna, the structure robustness, electromagnetic environment and interference in application scenarios should be addressed.

### 2.1.2 Glass-Integrated Antennas

Compared to concrete and soil, the electromagnetic characteristic of glass is stable, has a low cost of integrating and high feasibility. However, the minimisation and light transmissivity must be considered by integrating devices. The current glass-integrated antennas have been applied in various scenarios. In vehicles, the most commonly used communication is the radio function. Some existing designs for material-integrated antennas are designed for vehicular radio communications on the windows. In [17–19], the excitation sources and a few wires are added to the defroster lines on the rear window of the saloon. Fig. 2.3(a) exhibits the antenna structure in [17]. The mesh structure consists of horizontal defroster metal lines and five vertical wires. The optimal structure is obtained by using the Pareto genetic algorithm. The current distribution of the antenna is determined by connecting or disconnecting the vertical wires and feeding location. This work uses the inherent metal structure of the car, which expands the antenna's physical size without occupying additional space. Compared with the conventional car FM antenna on the roof with a smaller size, the vertical gain is improved. In [20], the mesh wires of the antenna's main body are printed on the glass surface by a silk-screening printing method. The mesh wire is optimised by the

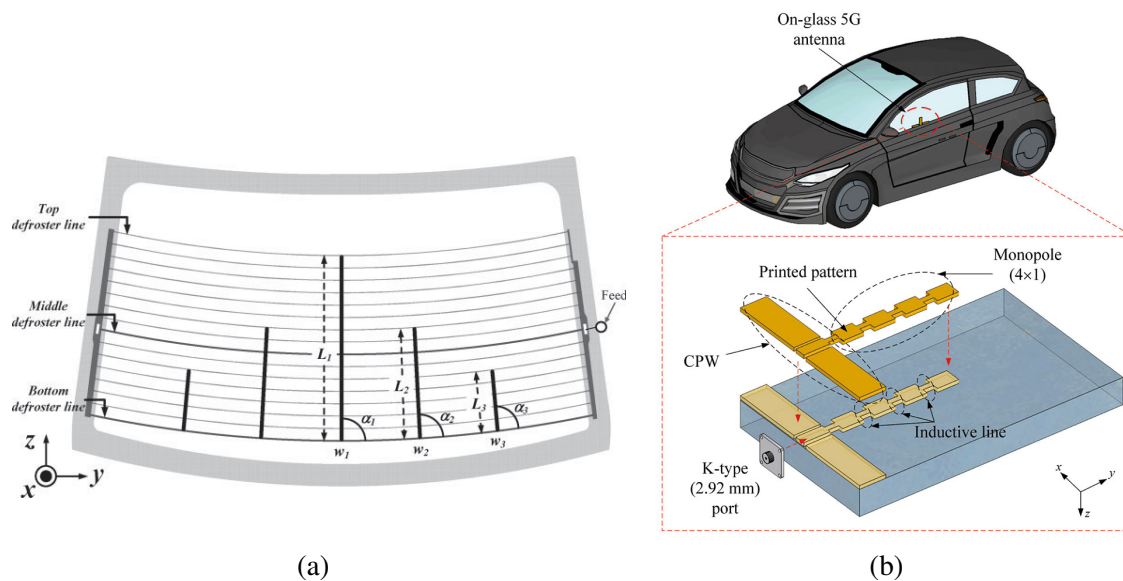


Fig. 2.3 (a) FM vehicle antenna based on defroster lines [17], (b) 5G vehicle antenna [21].

connection-warranted filtering method. Though the antenna with large size only occupies a little space as it relies on the glass, it affects the visual impact of the window.

In recent years, the low latency 5G has promoted vehicle-to-vehicle (V2V), vehicle-to-pedestrian (V2P) and vehicle-to-infrastructure (V2I) communications for driving safety. Vehicular communication cannot be limited by FM antennas, the higher frequency antennas for vehicles are explored. In Fig. 2.3(b), [21] provides a 5G glass integrated antenna with  $4 \times 1$  monopole elements using coplanar waveguide (CPW) feeding. The antenna provides a high gain and the phase can be adjusted. Nevertheless, simply attaching leads to the transparency and space loss on glass. It is urgent to develop an antenna that can be hidden in the structures with small sacrifices.

To facilitate access to information and increase work efficiency, wearable devices are expected to play an important role. The communication system installed on smart glasses will indeed become a fast channel for obtaining information in the future. In [22] and [23], the antennas on wearable glasses are proposed for Bluetooth and WiFi at 2.4 to 2.5 GHz. As shown in Fig. 2.4(a), three types of antennas are carried on the top of the lens, the side of the lens and the side of the glasses frame, respectively [22]. The type A and B antennas are designed along the curve of the lens. Three antennas can guarantee communication capability

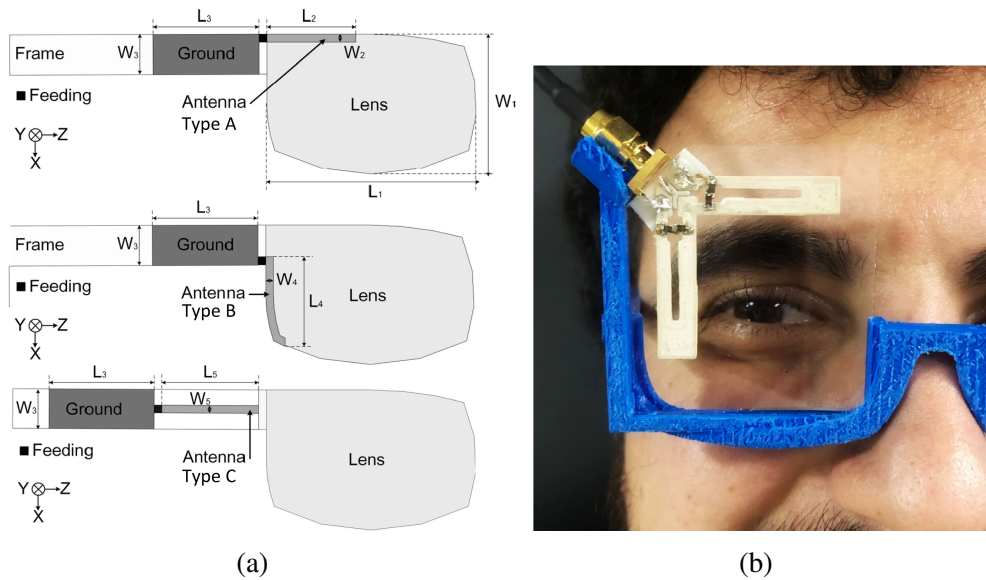


Fig. 2.4 (a) Antenna for wearable glasses [22], (b) reconfigurable slot antenna for wearable glasses [23].

while worn by a human. In Fig. 2.4(b), the antenna aims to be a part of the glasses frame. It comprises of the slotted L-shaped metal legs with CPW feeding. The two metal legs create different working modes which generate perpendicular polarisations.

## 2.2 Transparent Antennas

Since the 21st century, there has been a steady rise in the number of transparent conducting materials required by electronic devices such as touch screens, electromagnetic interference (EMI) shielding, organic LEDs and solar cells. It is predicted that the trend will persist in the foreseeable future [24]. The materials enable simultaneous electric conducting while transmitting visible light. The transparent conductive material is made into TCFs with a thickness of a micron scale. TCFs have been primarily applied to equipment with low demand on electrical conductivity and must be seen through human eyes. With the emergence of some applications that require high conductivity and transparency, highly conductive transparent materials such as metal-doped TCFs and MM have been developed [25, 26]. As the limitation of space, the current electronic devices increase the demand for size

reduction and concealment in order to integrate more functions. The development of TAs can significantly alleviate the contradiction between space and equipment.

This section gives a review of the mechanism of transparent conducting materials and a survey of the state of the art TAs. It involves the illustration of the trade-off between optical transparency and radio frequency (RF) sheet resistance, an in-depth survey of antennas using TCFs, metal-doped TCFs, micro MM and wired MM.

### 2.2.1 Transparent Conducting Films

TAs made by TCFs can transmit light as the materials offer high optical transparency and low resistance. The commonly used transparent materials for TCFs include transparent conductive oxides (TCOs) [27] such as ITO, fluorine-doped tin oxide (FTO), Al-doped ZnO (AZO), and Ga-doped ZnO (GZO) and other polymers such AgHT-4 and AgHT-8 [28–30]. So far, ITO is the most popular transparent conductive material, however, due to the indium shortage that will come soon, the indium prices are rising [31, 32]. FTO, AZO and GZO are promising to be the alternative oxides [33, 34]. To design optical TAs, the properties of TCFs should be evaluated. Electrical conductivity and optical transparency are the critical properties of TCFs.

In order to satisfy the communication requirement, the electrical conductivity of TCFs should be excited within the RF spectrum while transmitting light. The same as the common lossy conductors, the thickness of a TCF is related to its resistance. The sheet resistance  $R$  of the TCFs can be calculated as follows [35].

$$R = \frac{1}{\sigma t} \quad (2.1)$$

where  $\sigma$  is the electrical conductivity and  $t$  is the thickness.

The current in the thin film mainly flows within the skin depth of the sheet. It can be found as follows [26].

$$\delta = \sqrt{\frac{1}{\pi f \mu_0 \sigma}} \quad (2.2)$$

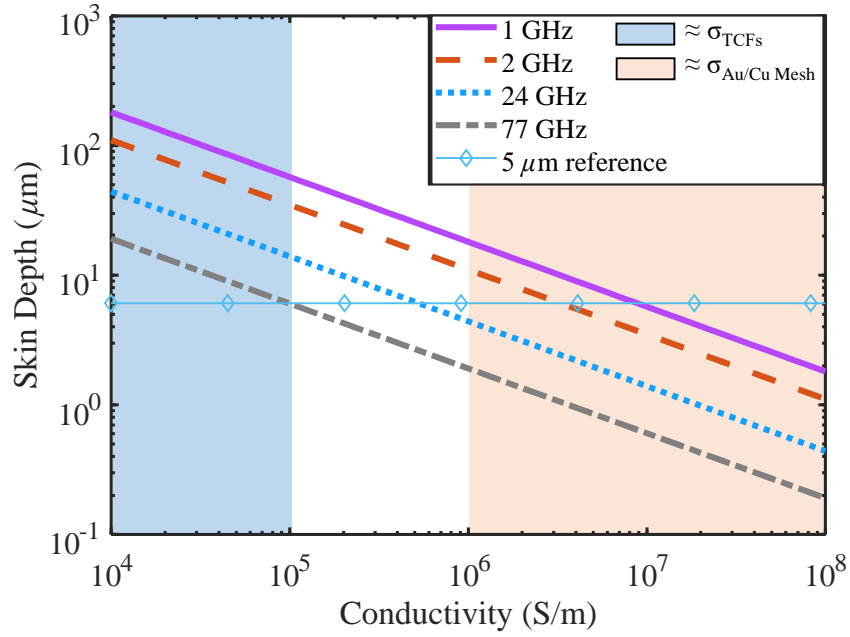


Fig. 2.5 Skin depth comparison of TCFs and MM at different frequencies [26].

where  $f$  is frequency,  $\mu_0$  is the permeability of free space ( $4\pi \times 10^{-7}$  H/m). The skin depth  $\delta$  is affected by the alternating current frequency. While the frequency rises, the current flows toward the surface and the skin depth is reduced. In other words, the current loss increases with frequency [36]. Compared with Cu and Ag, TCFs with larger loss should consider the influence of skin depth. Fig. 2.5 compares the impact of skin depth on the conductivity at different frequencies. The blue area is the conductivity range of the TCFs with common transparent materials and the light orange area represents the conductivity for Au or Cu mesh with the fill factor  $\Psi$  from 0.01 to 1. Within the blue area, the skin depth is above the 5  $\mu\text{m}$  reference line. At the  $10^5$  S/m conductivity, the skin depths are from 6-60  $\mu\text{m}$ . However, the thickness of most of TCFs is less than 5  $\mu\text{m}$ , the ohmic loss is much increased due to the effective cross-section being further reduced. The MMs have lower sheet resistance as they have better conductivity and their thickness is greater than the skin depths.

In the current TCF literature, TCOs are the most popular transparent materials. Table 2.1 shows the material properties of the ITO, AZO and GZO. ITO offers comparable transparency with lowest sheet resistant. This unique blend of properties allows ITO to maintain excellent optical clarity while providing efficient electrical conductivity, making it well-suited for

Table 2.1 MATERIAL PROPERTIES OF THE INVESTIGATED TCOS [27, 37–39]

Property	ITO	AZO	GZO
$N_e$	$13.8 \times 10^{20}$	$15 \times 10^{20}$	$14.6 \times 10^{20}$
Band gap (eV)	53.5	47.6	31
Thin film transparency (%)	75-92	76-95	90-96
$m^*$	$0.35m_e$	$0.24m_e$	$0.31m_e$
Mobility (cm <sup>2</sup> /Vs)	50	10-22	2-8
Sheet resistance ( $\Omega$ /sq)	3-10	4-15	6-17

Note:  $m_e$  is the real electron mass,  $m_e=9.11 \times 10^{-31}$  kg.

applications where both electromagnetic performance and transparency are crucial, such as transparent antennas. From the point of material structure, TCOs are semiconductors produced using a metal-doped oxide compound. The conductivity  $\sigma$  of TCOs can be calculated as follows [27]

$$\sigma = \frac{N_e q_e^2 \tau}{m^*} \frac{1}{1 + jf\tau} \quad (2.3)$$

where  $N_e$  denotes the carrier concentration,  $q_e$  denotes the unit charge,  $\tau$  is the electron relaxation time,  $m^*$  is the effective mass of an electron and  $f$  is the frequency. To guarantee the electron flow effectively in the microwave range, the plasma frequency  $f_p$  is defined as follows [27]

$$f_p = \sqrt{\frac{N_e q_e^2}{\epsilon_\infty \epsilon_0 m^*} - \frac{1}{\tau^2}} \quad (2.4)$$

where  $\epsilon_\infty$  is the optical dielectric constant,  $\epsilon_0$  is the dielectric permittivity in vacuum. The rapid electromagnetic oscillations cannot act on electrons at frequencies higher than plasma frequency, the current cannot flow through the TCO. While the film works at frequencies lower than plasma frequency, it acts as an electrical conductor.

To be optically transparent, TCOs should be thin enough and transmit visible light. However, the thickness  $t$  has an exponential impact on optical transparency. The optical

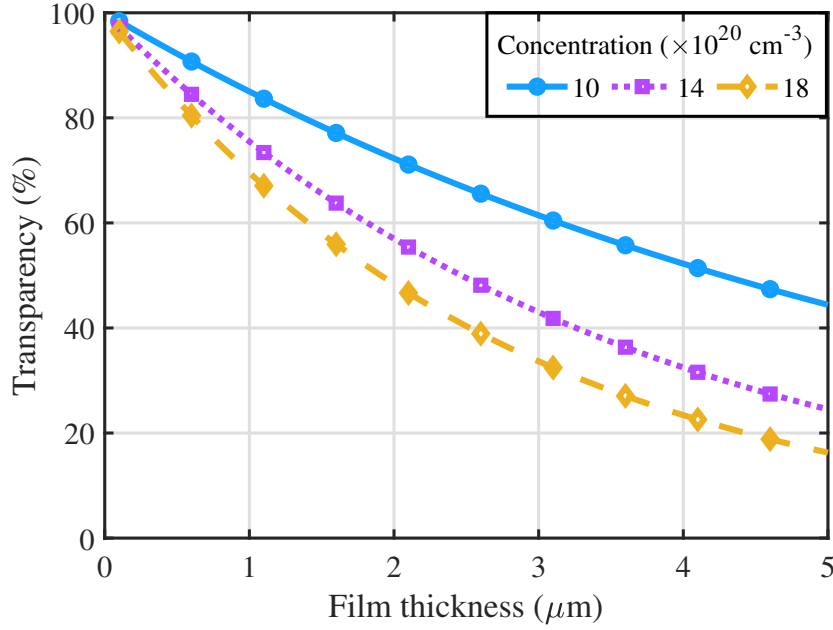


Fig. 2.6 The optical transparency versus film thickness with different carrier concentrations [25].

transparency  $T_{\text{TCO}}$  can be calculated as follows [25]

$$T_{\text{TCO}} \cong e^{-\frac{t}{\delta}} = e^{-\alpha t} \quad (2.5)$$

where  $\alpha$  is the absorption coefficient. Combining (2.2), (2.3) and (2.5), it could be noted that the optical transparency is affected by carrier concentration and film thickness. Fig 2.6 shows the transparency changed as thickness using different carrier concentrations. As the carrier concentration rises, the transparency is decreased. The influence of carrier concentration on transparency is increased as thickness increases. To achieve higher transparency, the thickness of commercial TCOs are always limited under 1  $\mu\text{m}$ .

### 2.2.2 TCF Antennas

The discussed TCFs have been exploited to promote antenna development by researchers. Although the TAs using TCFs are inferior to traditional antennas in performance, the current literature demonstrates their practicality in various environments.

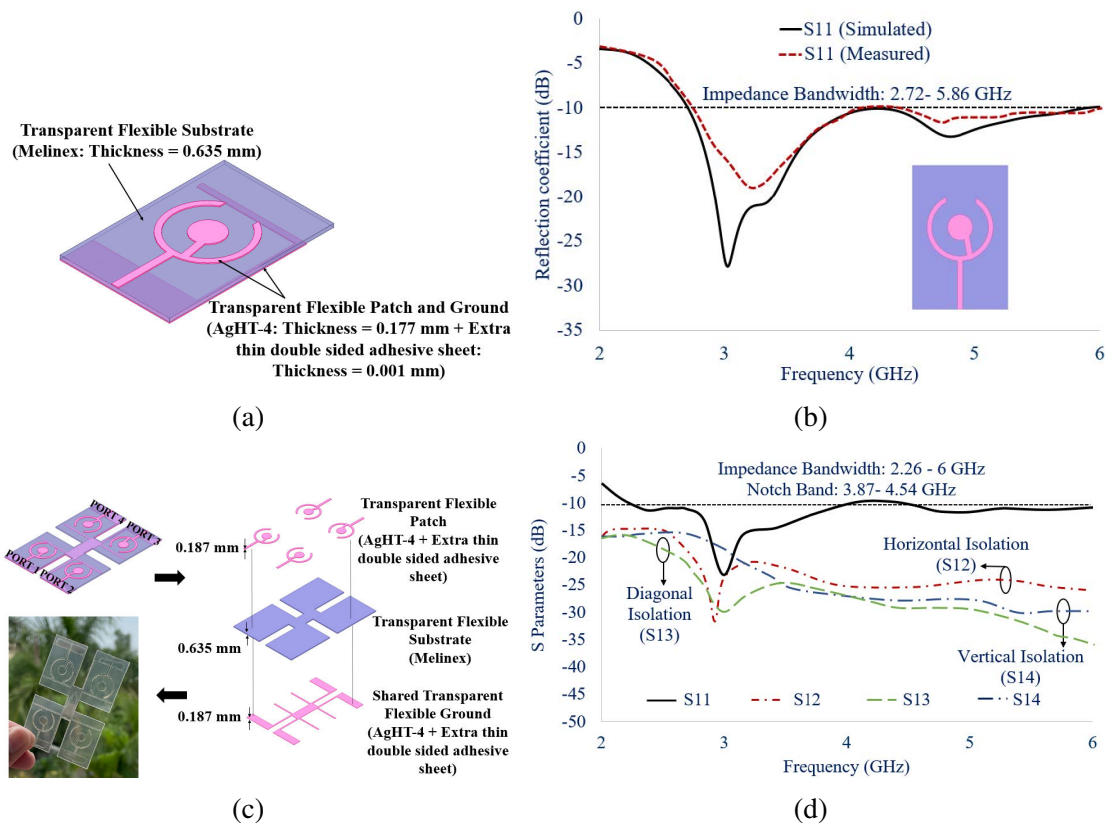


Fig. 2.7 Wideband MIMO TA, (a) geometry of antenna element, (b) simulated and measured reflective coefficient, (c) geometry and prototype of the MIMO antenna, (d) measured  $S$ -parameter of the TA [40].

To maximise the advantage of TCFs' glass-equivalent transparency, TCF antennas are mainly applied on transparent surfaces. As an example shown in Fig. 2.7, the monopole TA is made by AgHT-4 film and Melinex transparent substrate for MIMO applications [40]. For the materials of AgHT-4, the resistance is  $4 \Omega/\text{sq}$ , the conductivity is  $1.4 \times 10^3 \text{ S/m}$ , thickness is  $0.187 \text{ mm}$  and the transparency of a single film without substrate is about 70%. In Fig. 2.7(a), the main radiator of the antenna element comprises of a C-shape arc and a solid circle with an adjustable connection line. The ground plane consists of a rectangle film with a half-enclosed polyline. The function of the connection line is to eliminate the reactive component in the input impedance of the antenna and make the resistive component close to the characteristic impedance of the feed line. The ground plane and feed line function together to match the input impedance. The polyline can improve the diversity while forming an array. Fig. 2.7(b) shows that the optimal antenna element achieves wideband resonance

less than -10 dB at 2.72-5.86 GHz. Fig. 2.7(c) shows the MIMO antenna geometry and prototype. The Melinex substrate allows the antenna to be bent but has a frosted effect. By the superposition of film and substrate, the optical transparency should be less than 60%. Fig. 2.7(d) shows the measured  $S$ -parameter of the MIMO TA.  $S_{11}$  remains the wideband property but with a notched band at 3.87-4.54 GHz.  $S_{21}$ ,  $S_{31}$  and  $S_{41}$  show the isolation performance between the elements, which should be limited to less than -15 dB. Within the bandwidth, a strong mutual coupling is generated at a low frequency around 2.5 GHz and good isolation is achieved at a higher frequency range.

Though this antenna uses a thick film for gain and efficiency enhancement, it only achieves 0.53 dBi maximum gain and 41 % efficiency, which is much lower than conventional metal antennas. In the case of significantly reduced efficiency, the reflective power is reduced before reflecting the excitation source,  $S_{11}$  will be reduced, resulting in a broadband false appearance of some TCF antennas. Therefore, a TCF antenna with broadband performance should keep  $S_{11}$  much lower than -10 dB. In addition, the mutual coupling will be reduced due to large ohmic loss. Although the performance of the antenna can be further improved, this TA is an innovation to the TCF antenna, whose bendable medium further improves the adaptability of the antenna to various environments.

Traditional vehicle antennas have effects on the aerodynamic of the shell and aesthetics. Designing an antenna inside the vehicle will suffer serious scattering and shadowing by the metal shell [42]. The glass occupies a large area on the shell and provides opportunities for many applications. So far, a part of commercial vehicles have strobe devices on the front windshield for rear-end collision and fatigue driving warnings. In the future, the windshield can integrate display for multiple functions [43]. Thus, it is promising to design TAs on glass applications. In [41], a UWB MIMO TA using ITO film for vehicles is introduced. In Fig. 2.8(a), the geometry and prototype of the UWB MIMO TA are shown. The shape is optimised from a simple monopole with a rectangle patch and ground. The patch creates broadband behaviour and the ground eliminates the notch band. The TA uses ITO film with  $10 \Omega/\text{sq}$  sheet resistance and  $1.4 \mu\text{m}$  thickness. It achieves 72% in the ITO covered area and 80% in other areas. The gains are from -2 to 2 dBi and the efficiency is 40-60%. In Fig.

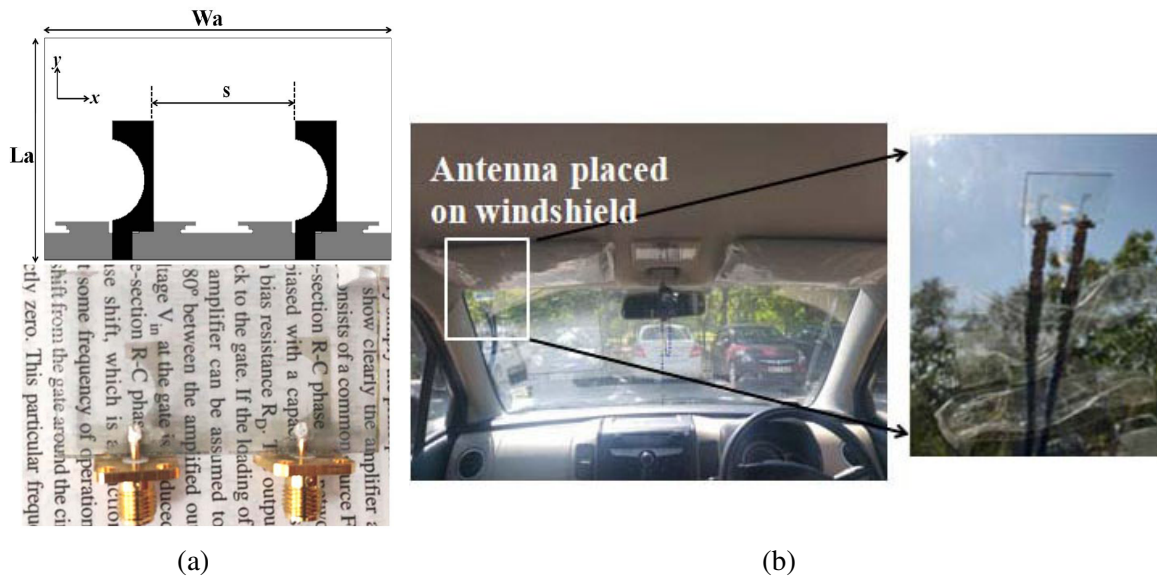


Fig. 2.8 UWB MIMO TA for automotive, (a) geometry and prototype, (b) TA mounted on the windshield. [41].

2.8(b), the TA is mounted on the windshield. The TA with good transparency has little effect on driving.

Though the TA has been well designed, the efficiency and gain are still low. To address the loss issues, the direct way is to improve the conductivity of the transparent films. In [44–47], the antennas use metal-doped TCO materials. In Fig. 2.9(a), the antenna uses copper-doped ITO film [44]. With the space feeding metal structure, the antenna achieves more than 65% efficiency. In Fig. 2.9(b), Ag-doped ITO films are applied on the conductive parts [45]. It achieves 80% efficiency and about 3 dBi for a single element which is very close to the conventional metal antennas. However, it could be noticed that the optical transparency is degraded and the colour of the films has been affected. The metal element in the transparent film will add additional refraction and reflection of light, which results in the film presenting a metallic colour.

For the TAs using TCFs, the main challenge is to improve the antenna performance while retaining transparency. Many TAs have explored the materials and geometries to enhance the performance. In [48], a gold nanolayer has been deposited in the ITO film. As a result, the efficiency of the single-layer monopole TA is improved compared with the ITO TA with the



Fig. 2.9 (a) TA array using copper doped ITO film [44], (b) TA array using Ag doped ITO film [45].

same shape. In [28], the highly conductive metal strips are embedded in the edge of the main radiator which is made of AgHT film. The gain is improved by 5 dB and the efficiency is improved from 35% to 70%. In [29], the TA uses a complementary split ring resonator on AgHT-4 film to enhance the broadband performance. In [49], the TCO film is embedded in a thick transparent polymer for the main radiator. With the metal microstrip feeding line, the antenna size is reduced, and the antenna efficiency is enhanced.

### 2.2.3 Micro MM Antennas

The other category antenna with optical transparency uses MM structure. According to the mesh size and the manufacturing processes, the MM for TAs design can be classified into micro MM and wired MM. The micro MM uses micro-fabrication techniques such as ink-jet printing, physical vapour deposition (PVD) and electroplating, while the wired MM can be fabricated much more simpler such as PCB manufacturing. The micro MM is constructed by many meshes with a micrometre scale that cannot be seen by eyes, and wired MM uses visible wires to form the meshes. Ideally, the meshes are square, while in practice, the meshes' shape and size can be regular and irregular, which are determined by the fabrication techniques [50]. Fig. 2.10 shows the ideal micro meshes, PVD processed and Ag-alloy etched micro meshes. The optical transparency of the micro MM material depends on the fill

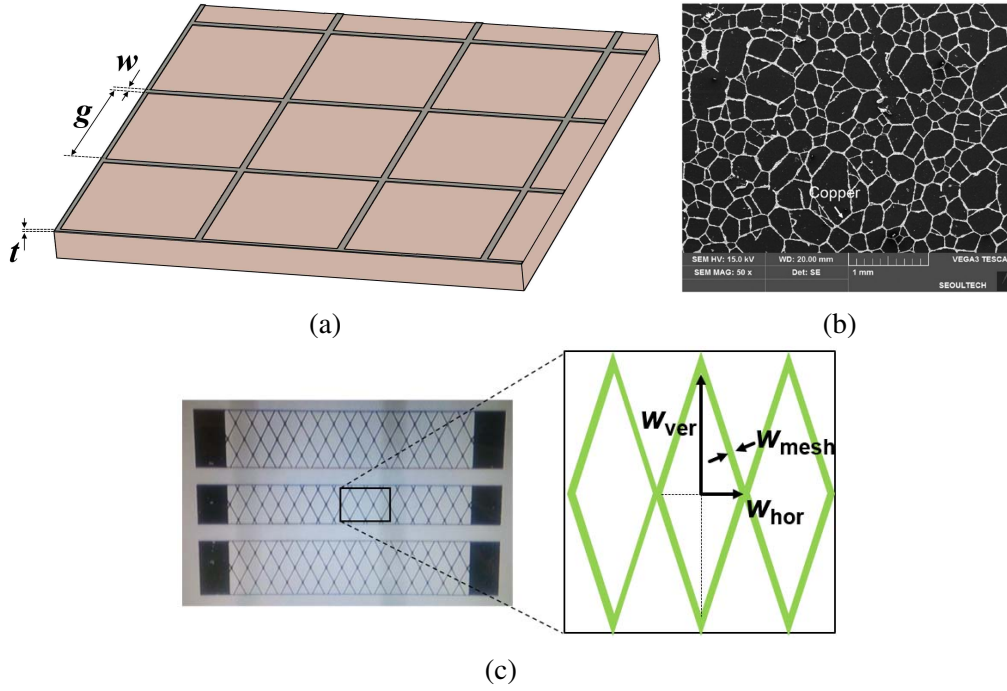


Fig. 2.10 (a) Ideal micro MM for fill factor definition, (b) PVD processed micro MM under the microscope [22], (c) photograph of diamond mesh structure fabricated by Ag-alloy etching ( $W_{ver}=100 \mu\text{m}$ ,  $W_{hor}=50 \mu\text{m}$  and  $W_{mesh}=3 \mu\text{m}$ ) [52].

factor  $\Psi$ , which is defined as follows [51],

$$\Psi = \frac{w}{g + w} \quad (2.6)$$

where  $w$  is the width of the metal line and  $g$  is the gap between the lines. Remaining the thickness constant, increasing the fill factor will decrease the sheet resistance and the transparency. The optical transparency  $T_{mMM}$  of the micro MM is defined by Equation (2.7). The sheet resistance  $R$  is defined in Equation 2.8.

$$T_{mMM} = (1 - \Psi)^2 \quad (2.7)$$

$$R = \frac{1}{\sigma t (1 - T_{mMM})} \quad (2.8)$$

where  $(1 - T_{mMM})$  is the area ratio occupied by micro MM. The sheet resistance of micro MM used in the current publications varies between 0.02 and 0.4  $\Omega/\text{sq}$ . It is shown that the

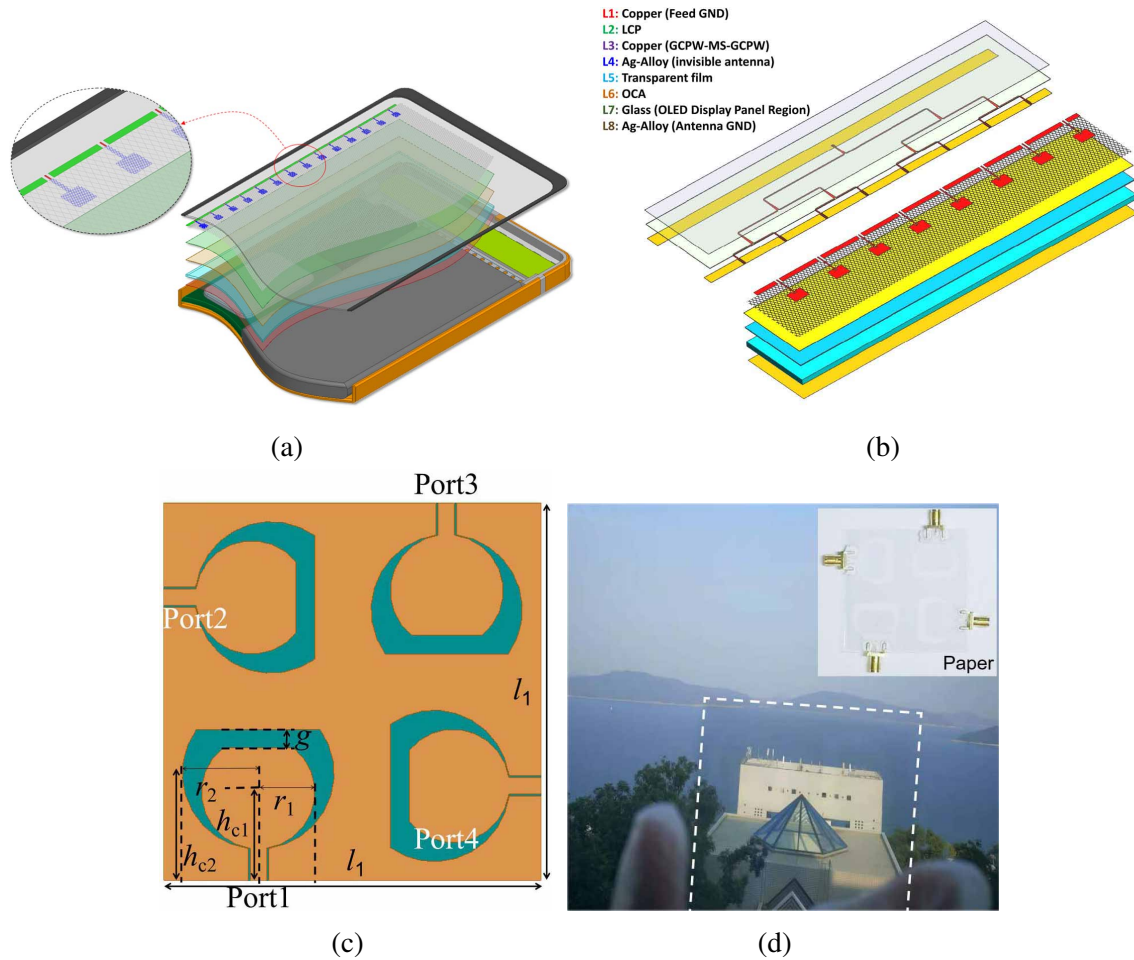


Fig. 2.11 (a) Antenna-on-display for mobile phone, (b)  $1 \times 8$  TA array with multilayer feeding structure [52], (c) geometry and (d) prototype of the MIMO TA in [53].

average sheet resistance of micro MM is about 1/25 of that of TCFs when they have the same transparency [26]. In addition, the light transmitted through the holes of the micro MM material can keep the wavelength of the visible light intact. However, the micro MM has light shadows as the metal is not transparent. When the transparency of micro MM and TCFs are comparable, micro MM has a poorer perspective effect. In addition, the cost of micro MM is much higher than the TCFs as the fabrication processes of micro MM are more complex.

The micro MM is favoured by many applications in terms of better performance on conductive and transparency. In [52], a micro MM TA array on mobile phone screen for mmWave 5G cellular devices is proposed. High transparency enables the antenna to be

seamless for general users. The antenna is fabricated using diamond mesh shown in Fig. 2.10(c). In Fig. 2.11(a), the antenna array is placed at the edge of the screen. Considering the high loss that will be generated in the feeding structure as the narrow feed line has a larger impedance, a novel multilayer structure for feeding is proposed shown in Fig. 2.11(b). The efficiency has been improving by 17% using the multilayer structure. The TA achieves 88% transparency, 41% efficiency and 6.7 dBi gain at 28 GHz. In [53], Ni-based embedded MM nanotechnology has been applied on TA arrays for 5G mmWave MIMO applications. The article evaluates the conductivity of the hexagon mesh with different fill factors. The trade-off relationship of fill factor and conductivity has been established, which helps it choose the most suitable fill factor for TAs. The geometry and prototype of the TA array for the 5G n79 band (4.4-5 GHz) are shown in Fig. 2.11(c) and (d). It uses a symmetric rotation shape and CPW-fed techniques for high isolation MIMO antenna design. The TA achieves the highest transparency (93%) in current published antenna design literature and has 85% radiation efficiency simultaneously. In addition to these, a lot of literature shows the superiority of micro MM in TA design. In [54], the micro MM film with 75 % transparency and  $0.02 \Omega/\text{sq}$  is cut into MIMO antenna arrays. Though the long feeding lines in the design show good radiation performance, they lead to larger loss. The TA achieves 46% efficiency. [55] presents a  $4 \times 1$  MIMO TA using micro MM with Lexan substrate. The high conductive micro MM allows low loss while using the narrow line for impedance matching. Dual polarisation and high gain that are comparable to traditional metal antenna array are generated. The special double-sided micro MM technology has been applied to mmWave TA array in [56]. The high conductivity of double-sided film reduces the loss in the transmission line and achieves a high gain.

Despite optimising the transparent conductive materials is the direct way to enhance the antenna performance, antenna structure optimisation should be considered more. Usually, conventional metal antennas barely consider efficiency issues, so copying traditional antenna shapes is detrimental to efficiency enhancement. Modifying the antenna structure is one of the key factors that can lead to a significant increase or decrease in efficiency. The TAs in

[55] and [54] use micro MM with approximate sheet impedance of 0.02-0.03  $\Omega/\text{sq}$ , but they have a huge gap in efficiency which are 78% and 40%, respectively.

### 2.2.4 Wired MM Antennas

Another transparent mesh is wired MM which is fabricated by using a traditional metal conductor with visible wires, hollowed holes and gaps [25]. The design method can be categorised into the meshed substrate with wired MM and the transparent substrate with wired MM. For the antennas with meshed substrates, the meshed patches, ground planes and substrate have a joint impact on the radiation performance, which may vary from their solid shapes. The optimisation process of this type of antenna is more complicated. As it can be fabricated by simple and cheap PCB processing and laser cutting, compared with TCFs and micro MM, it has a much lower cost. For the wired MM antennas with transparent substrates, the transparent substrates for commercial usage usually have no conductive cladding attached. The conductive materials such as silver epoxy are deposited on the surfaces to create the antennas [57]. This step increases the cost of fabrication.

Thick wires between the holes or gaps guarantee good conductivity of the material. In this case, the efficiency difference between the TAs using wired MM and the traditional metal antenna should be small. However, as the current can only flow on the meshes, the large meshes will change the distribution characteristics of the current on the original solid antenna and affect the performance [58]. The working mode changed as the current distribution weakened the radiated energy of the antenna and increased the reflected energy, resulting in a decrease in efficiency and gain. In essence, wired MM transforms the contradiction between transparency and efficiency into a contradiction between transparency and working mode. The transparency  $T_{\text{wMM}}$  of wired MM is defined as [58]:

$$T_{\text{wMM}} = 1 - \frac{A_{\text{mesh}}}{A_{\text{solid}}} \quad (2.9)$$

where  $A_{\text{solid}}$  is the occupied area of the TA in solid shape and  $A_{\text{mesh}}$  is the meshed area. Though the wires block some of the line-of-sight transmission of light, the wavelength of

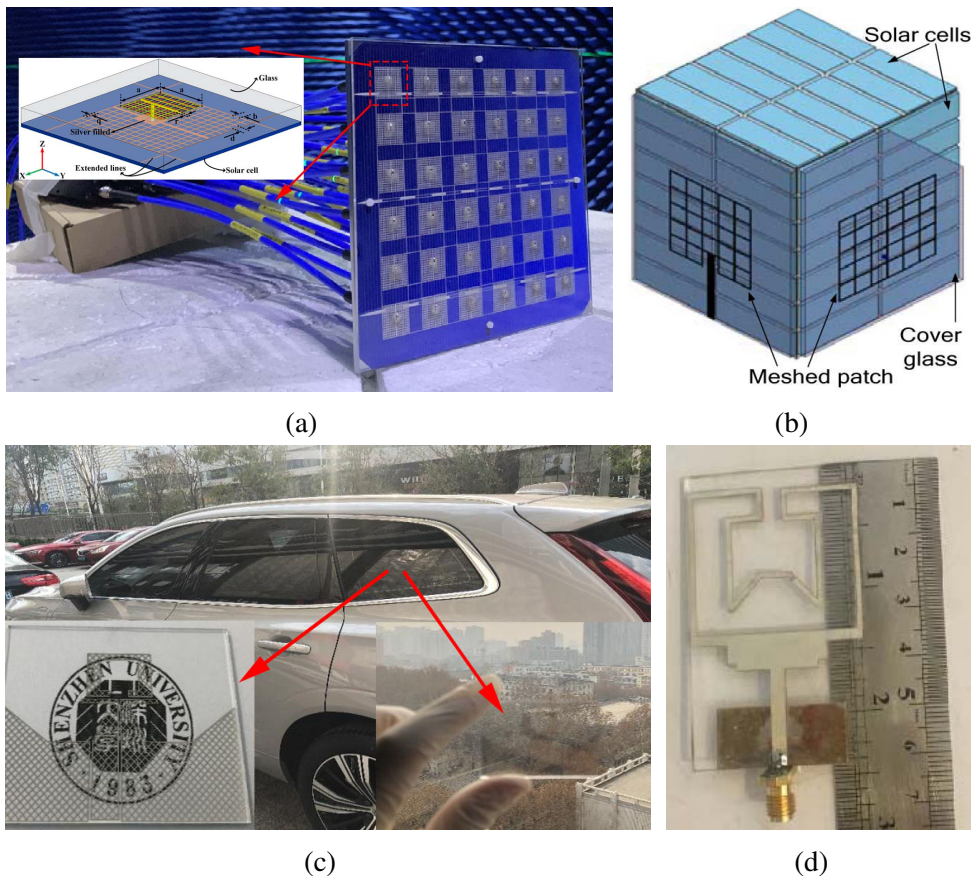


Fig. 2.12 (a) The geometry of the element and the prototype of the TA array in measuring environment [59], (b) isometric view of the wired MM TA attaching to the solar cells with covered glass [60], (c) TA using meshed structure for vehicle applications, (d) a triple-band TA.

light passing through is unlimited and the light passed through the hollowed area is entirely unobstructed. Wired MM is favoured for applications that prefer light transmission over uniform transparency. For example, solar panels, satellites, glass and other applications with the opaque substrate are the main applications for wired MM TAs.

In [59], a  $6 \times 6$  antenna array is coated on a solar panel for high gain and X-band operation is presented. Fig. 2.12(a) shows the TA array geometry and prototype. The TA array is constructed by meshed patch and ground plane on both sides of the glass substrate. The operating bandwidth and efficiency of the element decrease, and the mutual coupling increases with the mesh gap narrowing. After the trade-off, the TA achieves 20 dBi gain and 88% efficiency. It states that the solar cell remains its photovoltaic generate efficiency while covered by the TA array. In addition, the solar panel has been combined with satellites

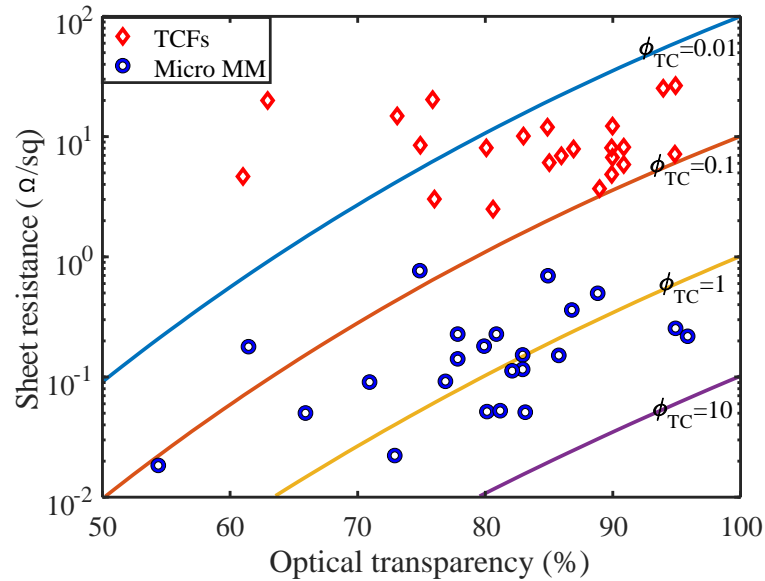


Fig. 2.13 The reported TAs using TCFs or micro MM, where  $\phi_{TC}$  denotes the figure-of-merit [26].

[60, 61]. As shown in Fig. 2.12(b), the TAs in [60] achieves 93% transparency and are integrated into the solar cells with glass cover. In [61], a broadside radiation pattern with 5.2 dBi gain is achieved on the solar panel. The applications on glass substrates are illustrated in [62, 63]. As shown in Fig. 2.12(c), the wired MM can be perfectly hidden in the glass window with UV films [62]. Based on the wired MM, the article [64] proposes an innovative new transparent shape as shown in Fig. 2.12(d). The antenna only keeps the edges of the original solid antenna as the current is focused on the edges. By further analysing the current distribution, the antenna not only remains the original working mode but also creates triple-band resonance. In addition, it hollows out the patch and the solid substrate and integrates with the glass piece. The TA with FR-4 substrate is simple for fabrication and low cost.

### 2.2.5 TCFs and MM Comparison

This section compares the materials' properties and antenna performance of state of the art. In Fig. 2.13, we collect the sheet resistance and the transparency of the TAs using TCF or micro MM. Wired MM is not included as the conducting mechanism and transparency calculation of wired MM differ from theirs. It can be seen that the micro MM exhibits

significant superiority over TCFs in terms of conductivity. The sheet resistance of micro MM is limited below  $1 \Omega/\text{sq}$ , while the TCFs are within  $1\text{--}30 \Omega/\text{sq}$ . Additionally, the overall transparency of TCFs is relatively higher and more TCF TAs exceed 85%. The figure-of-merit reference line classifies each material into different levels. The material closer to the lower right corner has better transparency and sheet resistance performance. No reported TA is below  $\phi_{TC}=10$ , which shows that the trade-off between transparency and conductivity has an upper limit.

Table 2.2 comprehensively compares the reported TAs with TCFs [22, 28, 33, 40, 41, 45, 65–75], micro MM [50, 52–56, 67, 76–79] and wired MM [59, 61, 63, 64, 80, 81]. Regarding material properties, the lowest sheet resistance achieved by TCFs is  $1 \Omega/\text{sq}$  [45] while that of micro MM is  $0.015 \Omega/\text{sq}$  [50]. The micro MM has better average conductivity than the TCFs counterpart. Lower sheet resistance generally results in low transparency, high gain and efficiency. Nevertheless, [22, 40, 50, 54, 67] use the material with lower than average sheet resistance have the efficiency or gain that is lower than the average. [55, 56, 75] achieve higher efficiency and gain than the average with higher sheet resistance. It can be noted that the average transparency of TCFs is the lowest, and TCFs have better visual effects as they look more like crystals in practice. Micro MM has light metal colour, and wired MM blocks some line-of-sight transmission.

## 2.3 Transparent Metasurfaces

Metasurface antennas consist of a series of conductive or dielectric scatter elements on the surface and feeding source. The properties of the source antennas can be controllably affected by metasurfaces. Metasurfaces are closely related to the transmitarray and reflectarray of the antennas as many theories of the antenna array are directly applied to metasurfaces [82]. The fundamental properties of metasurfaces are described as follows.

- The distribution and dimension of the elements of a metasurface can be homogeneous and heterogeneous, while the traditional antennas with array surfaces consist of periodic elements [83].

Table 2.2 Comparison of the Reported TAs

Ref.	Technique	Sheet Resistance ( $\Omega/\text{sq}$ )	Transparency	Element	Dimension (mm)	Band (GHz)	Efficiency	Gain (dBi)
[16]	(IZTO)/Ag/IZTO	3	0.811	2	-	2.4-2.5	0.4	2.6-3.6
[22]	AgHT-4+metal strip	4.5	0.7	1	60×120	2.2	0.68	0
[27]	GZO	-	76%	1	10×60	2.2-2.6	0.45	2.1
[34]	AgHT-4	4	0.7	4	66×45	2.2-6	0.41	0.53
[35]	FTO & ITO	4 & 10	0.72	2	29×50	2.4-11	0.6	-2-2
[39]	AgITO	1	45% & 66%	1 & 2	29×29 & 47.6×27.6	5.8	71% & 80%	2.3 & 5
[59]	AgHT-8	8	0.8	1	30×45×0.175	3.15-32	-	-6--3.2
[60]	AgHT-4	4	75%	1	17×33.5×2	2.2-12.1	48%	-8-0
[61]	IZTO/Ag/IZTO	2.5	0.8	1	50×50×1	2.4-2.5	7.8%	-4.2
[62]	AgHT-4	4.5	0.75	1	55×85×5.3	3.4-3.8	0.5	4
[63]	AgHT-8	8	0.85	1	50×60×0.35	1-13	2%-20%	-11--2
[64]	AgHT-8	8	0.83	1	23.4×20	2.5-12.5	-	-10--4
[65]	ITO	6	0.84	4	-	4.9 & 26	-	1 & 3
[66]	AgHT-4	4	0.75	1	30×30	2.4 & 5.8	-	2.4 & 2.9
[67]	ITO+metal FSS	7	-	5×5	52×52	5.73-5.85	-	-6
[68]	ITO	3	0.8	1	9.4×6.8	9.5-10.5	0.6	4.5
[69]	AgHT-8	8	0.85	2×2	24×20×1.85	24.1-27.2 & 33-44.1	0.75	3
<b>Average performance</b>		<b>5.3</b>	<b>75%</b>	-	-	-	-	-
[44]	Honeycomb mesh	0.015	0.73	1	-	77	-	0
[46]	Ag-alloy	-	0.88	8	-	28	24% & 41%	6.7 & 9.2
[47]	Ni embedded	-	93% & 86%	4 & 8	60×60 & 45×13.5	4.7 & 26-28	85% & 61%	3.8 & 9.7
[48]	-	0.05	0.75	2	40×40	2.4 & 5.8	43% & 46%	0.7 & 2.3
[49]	-	0.28	84.5%	4	20×30	5-6	78%	6-7.2
[50]	Double side	0.5	68% & 80%	4×2	25×25×0.2	58 & 59.7	80%	13.6 & 15.6
[61]	-	0.18	0.6	1	50×50×1	2.4-2.5	0.43	2.6
[70]	-	0.3	0.8	1	50×50	2.25-3	49%-57%	5.3
[71]	-	-	0.97	1	31.5×43	2.4	0.22	-1.4
[72]	Ag-alloy	-	0.88	1	10×7	2.7-5.2	0.7	2.6
[73]	Au/Ti bilayer	0.44	0.83	1	2.3×2.3	60	0.85	3
<b>Average performance</b>		<b>0.25</b>	<b>81%</b>	-	-	-	-	-
[53]	Silver-meshed	-	0.88	6×6	157×157	8.51 to 9.10	0.35	20.5-22
[55]	-	-	0.92	1	10×10	23.6-24.3	-	5.9
[57]	-	-	0.9	1	44.1×66.1 & 28.4×43.7	1.6 & 2.4	79% & 86%	4.2 & 5.3
[58]	-	-	0.8	1	60×40	0.95 & 2.1 & 4.6	66% & 87% & 88%	-0.2 & 3.7 & 4.4
[74]	Double side	-	0.6	1	97×97	1.575	72%	6.7
[75]	-	-	-	1	70×70	2.74	-	5.2
<b>Average performance</b>		-	<b>82%</b>	-	-	-	-	-

- The elements of the metasurface should be electronically small and correspond to sub-wavelength [82].
- Based on the source antennas, better performance or more functions should be achieved by the metasurface, such as gain enhancement [84], bandwidth extension [85, 86], multiple band resonance [87], frequency selection [88], radar cross section (RCS) reduction [89], polarisation conversion [90], beam steering [91], beam formation [92] and so on.

Metasurfaces can play an important role in future high-frequency communications. For example, it can improve beam directivity to improve communication accuracy and reduce BS power. At present, metasurfaces have been maturely used in antennas. However, some features of current metasurfaces are contrary to the requirements of future indoor communication. The real indoor application environment will degrade the metasurface performance. The disadvantages of current metasurfaces for indoor applications are summarised as follows.

- Metasurfaces will seriously affect the appearance and reduce space utilization if installed on the ceiling, wall or glass surface. Generally, better performing metasurfaces require more elements resulting in larger sizes.
- Although metasurfaces can be attached to the surface of objects, it is still a challenge to realize their functions, as many metasurfaces require source antenna excitation in a specific position. It is impractical to dedicate an area specifically for the placement of the source antenna.
- Transmissive metasurfaces may lose effect because the metasurfaces can hardly be placed in the air. The feed-to-surface distance must be narrow in order to reduce overall volume.
- The properties of medium-dependent metasurfaces can be affected. Medium impact assessment could be more conducive to the large-scale promotion of metasurfaces.

To address the disadvantages, the indoor environment should be evaluated and the metasurfaces should be designed based on real scenarios. Designing transparent metasurface antennas with reference to conventional metasurfaces and TA can be a way for indoor applications. According to the material's conductivity, conductive and dielectric metasurface are disclosed in the following sections.

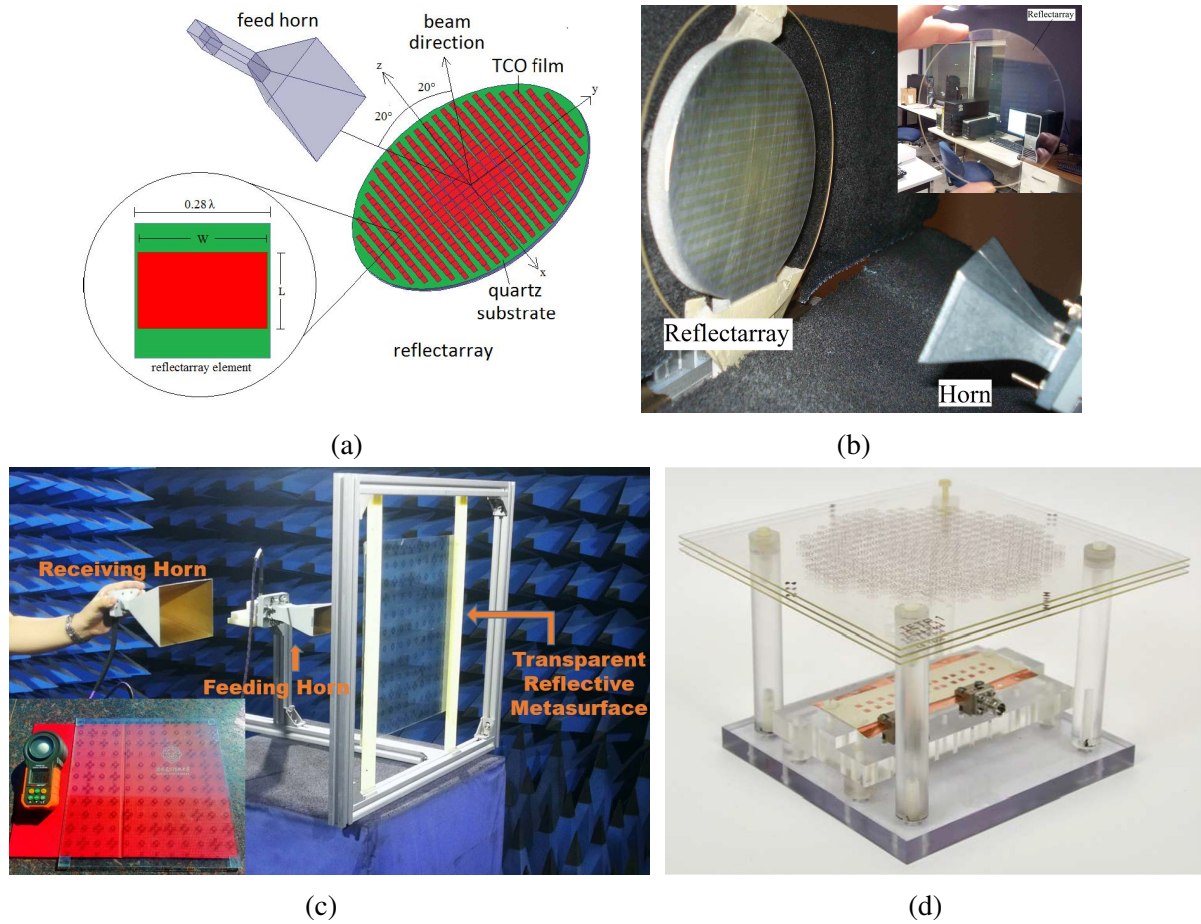


Fig. 2.14 (a) The working pattern of the reflectarray, (b) the prototype under the experiment [93], (c) the metasurface prototype and measuring environment [94], (d) prototype of the transparent transmitarray [95].

### 2.3.1 Conductive Metasurfaces

A conductive metasurface is defined as a metasurface containing conductive materials such as metals and TCFs. In [93], ITO film with  $8 \Omega/\text{sq}$  surface resistance has been applied on the transparent reflectarray for solar applications. Fig. 2.14(a) illustrates the working pattern of the reflectarray, and Fig. 2.14(b) shows the prototype of the antenna. The reflectarray consists of 392 elements with different densities and is fed by a 16 dBi horn at around 26 GHz. The reflectarray achieves 6.2 dBi gain enhancement and 22.2 dBi peak gain. Similarly, in [96], a transparent reflectarray with three-layer ITO elements is developed to improve the gain and efficiency. It achieves 25.8 dBi gain and 37.3% efficiency at 28 GHz. In [94], a

transparent metasurface is proposed for near-field focusing. It can provide service to wireless harvesting and power changing systems. Fig. 2.14(c) shows the measurement setup of the reflective metasurface prototype. The metasurface comprises two types of elements with the cross-dipole structure and the Jerusalem Cross structure and mesh ground. All conductive parts are made by ITO film. These transparent metasurfaces achieve high transparency, however, they are fed by horn antennas. As a reference, a horn antenna for 10 to 15 GHz with 15 dBi gain is around  $150 \times 60 \times 30 \text{ mm}^3$ . Its non-negligible volume makes it difficult for existing transparent metasurfaces to apply to indoor environments directly. To avoid occupying large space, the source antenna and metasurfaces are integrated into a double-layer model. In [44, 95], the transparent transmitarrays are excited by the feed arrays, which are close to the surfaces. Fig. 2.14(d) shows the prototype of the three-layer transmitarray with the array feeding. It achieves  $\pm 30^\circ$  beam steering with 25 dBi peak gain.

At present, though the researches on transparent metasurfaces are scarce, many opaque metasurface antennas have been developed. Among them, one of the most suitable structure for indoor installation is the Fabry-Perot cavity (FPC) structure [97]. FPC consists of double-layer surfaces and an attached feeding structure [98]. In buildings, the double-layer structure is widely applied on windows, doors, baffles and so on [99]. In addition to the convenience of layout, the opaque FPC antennas can achieve many functions. Wide bandwidth is achieved by S-shape elements on superstrate [100], two-layer partially reflective surface (PRS) [101] and two complementary frequency selective surfaces (FSSs) [98]. High gain [102] and high directivity [103] are one of the core features of the FPC antennas. The broadband and 5G MIMO are combined using a single layer PRS in [104]. Beam scanning is achieved by tunable high impedance surface of FPC [105]. Beam steering technology is achieved by FPC leaky-wave antenna [106] and phase-modulated metasurfaces [107].

It is promising to combine the transparent metasurface with the FPC in the future. The mechanism of the FPC with transparent materials and related technologies will be analysed in Chapter IV with the proposed transparent FPC antenna.

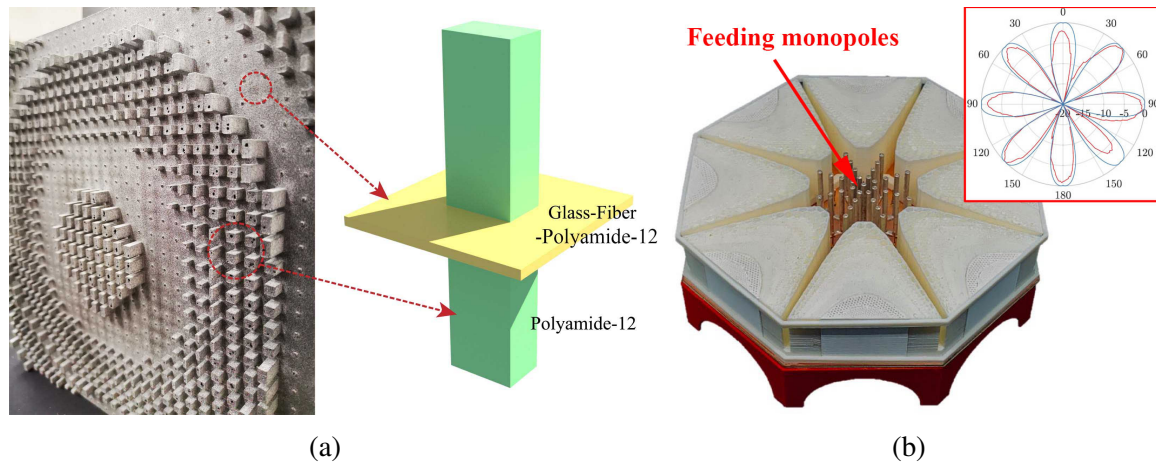


Fig. 2.15 (a) The element and metasurface geometry [108], (b) prototype and its H-plane radiation pattern at 5.8 GHz [109].

### 2.3.2 Dielectric Metasurfaces

Dielectric metasurfaces are all made of dielectric materials. With the increasing precision and popularity of three-dimension (3-D) printing, dielectric metasurfaces have become more attractive. Transparent resin, acrylic and other materials are cheap and can be applied to any 3-D printer. The loss of space waves through dielectric materials is much lower than that through lossy conductive materials. Compared to TCFs and MM, the antennas using transparent dielectric metasurfaces have the advantages of low profile, low cost and higher radiation efficiency. Though dielectric resonators and metasurfaces exist, the transparent dielectric metasurface has yet to be explored. In order to invent it, the previous dielectric metasurfaces are referred to.

In Fig. 2.15(a), an ultra-broadband all-dielectric transmissive metasurface is designed [108]. The character of the surface is determined by the dimension and shape of the raised pillars. They are optimised using the genetic algorithm based on Snell's Law. The metasurface is fabricated using polyamide-12 and glass fibre by 3-D printing. The metasurface is fed by a ridged horn and achieves 7-12 dB gain enhancement at 9-20 GHz. Additionally, literature [110, 111] also uses metasurfaces with pillars to enhance the gain. In [109], an all-dielectric metasurface fed by embedded monopoles achieves multiple beam creation. The antenna prototype and its radiation pattern are shown in Fig. 2.15(b). It can produce uniform beams

with approximately 8.5 dBi gain. In [112], an inhomogeneous all-dielectric metasurface for diffusive reflection is provided using 1-bit and 2-bit coding unit cells. In [113], a dielectric metasurface is used as a PRS of the FPC antenna. Combined with the metal ground and feeding antenna, it generates a wideband near-field correlation. In [114], a lens-like metasurface is proposed, which achieves the effect of converging beams to increase gains. Though the above metasurface antennas exhibit good performance, they are not suitable for being placed indoors. Thus, a transparent all-dielectric metasurface is proposed in Chapter V.

## 2.4 Summary

In this chapter, the author reviews the antennas that have the potential to be transformed for indoor communications. Meanwhile, their advantages and challenges in indoor applications are analysed. The material-integrated antennas can be easily hidden. But they need to be more convenient to install and repair. Their performance is affected by the materials' properties variation. TAs have good application prospects, but they must better balance the transparency and efficiency in indoor environments. Transparent metasurfaces have great potential due to their excellent performance in conventional opaque antennas. However, the development of transparent metasurfaces faces great difficulties as little literature has paid attention to this field. Especially for the ADTL, it has not been proposed in any literature.

# Chapter 3

## Metal Mesh Antennas

### Overview

In this chapter, three TAs with mesh or grid structures are presented. In Section 3.1, a mesh-grid structure was proposed that relied on the existing metal grid structure in buildings. Section 3.2 develop the mesh-grid to wired MM based on glass substrate. Section 3.3 further studies the wired MM and proves its practicality. The following paragraphs briefly introduce the designs in each section.

**Section 3.1** presents a triple-band glass-integrated grid antenna used in indoor communications. Integrating the antenna with the inherent glass structure of the buildings is a method of optimising the deployment of indoor base station. The antenna consists of three concentric square grid structures. By characteristic modes analysis (CMA), characteristic current distribution can be obtained and three optimum operating modes can be excited with a single feeding. Each operating mode generates broadside radiation, and each resonant frequency can be tuned independently. In order not to affect the usage and aesthetic of the building, the proposed antenna is integrated into glass as metallic grids which can also strengthen the robustness of the glass. To demonstrate the effectiveness of the concept, a design for GSM at 1.8 GHz, WLAN at 2.4 GHz and a low-frequency band for 5G at 3.5 GHz is provided.

**Section 3.2** presents a CPW-fed transparent antenna array (TAA) in order to reduce the space occupation and virtual influence of the indoor base station. The TAA is comprised

of 4 CPW-fed antenna units and a standard glass substrate. The gain is improved by array structure to 7.6 dBi. The transparency of the antenna achieves 80%. It achieves more than 90% efficiency. The TAA operates at the bands of 2.12-2.5 GHz.

**Section 3.3** presents a transparent UWB MIMO antenna based on a wired MM structure. TAs can be integrated on various building materials with little visual impact to facilitate flexible massive indoor wireless device deployment. The proposed antenna achieves 77% transparency by hollowing out both metal and substrate into a mesh shape, while maintaining more than 83% radiation efficiency. The MIMO antenna consists of 4 elements, each being a CPW-fed UWB monopole and adjacent elements being placed orthogonally to produce dual polarisation. The operating band of the MIMO antenna spans over 3.2-11.2 GHz. A parasitic decoupling structure aligned with the mesh grid is designed to enhance the isolation between MIMO elements without degrading the transparency. Within the entire operating band, the isolation between any two elements is more than 20 dB. The peak gain varies from 3.3 dBi to 7.2 dBi within the bandwidth. The envelop correlation coefficient (ECC) is less than 0.004. The channel capacity and time domain response are analysed. The antenna can be easily fabricated by conventional PCB and laser cutting techniques with a low cost.

## **3.1 Glass-integrated Antenna Using CMA for Multiband Indoor Network**

### **3.1.1 Introduction**

Small BSs are expected to be deployed densely indoor to enable wireless traffic increase [115]. To avoid affecting the usage and aesthetics of room, antennas should be well integrated with building material [116]. Since glass with metal grids is widely used as shutters, explosion-proof and burglar-proof windows in modern buildings, antennas can be integrated with glass to provide good signal coverage. Researches show the glass-integrated antenna has advantages of styling, light weight, security and reliable [117], and so far the glass-integrated antennas are mainly applied in vehicles at FM/AM radio frequency band [19]. By modifying

the metal grid integrated with glass, antenna for the indoor network at higher frequency bands can be designed.

To obtain good radiation pattern without degrading the transparency of glass severely, the structure and feeding of the glass-integrated antenna should be optimised. CMA is an efficient method to determine the inherent modes of an arbitrary shape antenna, which can be applied to design multiband and high efficiency antenna [118].

In this section, a glass-integrated grid antenna achieved multiband resonance in UHF and SHF band is proposed. With the aid of CMA, three operating modes with vertical polarization can be obtained by continuously optimising the structure based on simple square grid. Each resonance frequency is determined by the length of corresponding square grid, which leads to strong adjustability of the design. Characteristic current indicates that the three modes can be simultaneously excited by a single feeding. Furthermore, the grid antenna is integrated with glass and the impacts of glass are discussed.

### Electric Field Integral Equation

Traditionally, the surface integral equation of can be applied to closed and open structures. The electric field integral equation (EFIE) can be used to support characteristic mode (CM) theory. This section formulates the EFIE of PEC bodies based on Maxwell's equations. Following the derivation of Maxwell's equation in [118], the electromagnetic boundary condition for PEC structures in homogeneous medium is obtained. For an arbitrary surface  $S$  of PEC, we have

$$(\mathbf{E}^i(\mathbf{r}) + \mathbf{E}^s(\mathbf{r}))_{tan} = 0, \mathbf{r} \in S \quad (3.1)$$

where  $\mathbf{E}^i$  is incident plane wave,  $\mathbf{E}^s$  is scattering field,  $\mathbf{r}$  is observation point and the subscript "tan" means the tangential component of the electric field.

By introducing the electric field expressed by magnetic vector potential  $\mathbf{A}$  and electric scalar potential  $\Phi$  in the source-free region, the scattering field can be expressed as:

$$\nabla \cdot \mathbf{A}(\mathbf{r}) = -j\omega\epsilon\mu\Phi(\mathbf{r}) \quad (3.2)$$

$$\mathbf{E}^s = -j\omega\mathbf{A}(\mathbf{r}) - \nabla\Phi(\mathbf{r}) = -j\omega\mathbf{A}(\mathbf{r}) - \frac{j}{\omega\epsilon\mu}\nabla(\nabla\cdot\mathbf{A}(\mathbf{r})) \quad (3.3)$$

where  $\epsilon$  and  $\mu$  are constituent parameters permittivity and permeability respectively.  $\mathbf{A}(\mathbf{r})$  can be obtained by the integrating the closed surface after eliminating the singularity at the observation point  $\mathbf{r}$ .  $\mathbf{A}(\mathbf{r})$  is given by:

$$\mathbf{A}(\mathbf{r}) = \frac{j\mu}{4\pi} \int_S \mathbf{J}(\mathbf{r}') G(\mathbf{r}, \mathbf{r}') dS' \quad (3.4)$$

where  $\mathbf{J}(\mathbf{r}')$  represents the current in source point  $\mathbf{r}'$ ,  $G(\mathbf{r}, \mathbf{r}')$  is the free space Green's function [119] multiplied by  $4\pi$  and is given by:

$$G(\mathbf{r}, \mathbf{r}') = \frac{e^{-jkR}}{R} \quad (3.5)$$

where  $R = |\mathbf{r} - \mathbf{r}'|$ . Combining (3.1), (3.3) and (3.4), the tangential incident plane wave can be expressed as EFIE:

$$\mathbf{E}_{tan}^i(\mathbf{r}) = \frac{jk\eta}{4\pi} \left( \int_S \mathbf{J}(\mathbf{r}') G(\mathbf{r}, \mathbf{r}') dS' + \frac{1}{k^2} \nabla \int_S \nabla' \cdot \mathbf{J}(\mathbf{r}') G(\mathbf{r}, \mathbf{r}') dS' \right)_{tan} \quad (3.6)$$

where  $k = \sqrt{\epsilon\mu}$  and  $\eta = \sqrt{\epsilon/\mu}$  are wavenumber and wave impedance in homogeneous medium, the report defaults the medium is free space.

## Method of Moment

The EFIE can be transformed into a matrix equation by the method of moment (MoM). When dealing with electromagnetic problems, MoM mainly expresses unknown parameters, such as current, in the form of expansion function which is also called the basis function. This section takes a thin wire as an example to describe the processes of discretising EFIE which include: dividing the dipole into many small segments; using appropriate basic function to expand the unknown current; using testing function to transfer the EFIE into a impedance matrix [118, 120].

A thin wire with very small radius  $r \ll L$  is divided into  $N$  segments and each of them has the length of  $\Delta x$ . Assume the current over the length of a segment is the same, the total current  $\mathbf{J}(\mathbf{r})$  can be represented as:

$$\mathbf{J}(\mathbf{r}) = \sum_{n=1}^N J_n \mathbf{f}_n(\mathbf{r}) \quad (3.7)$$

where  $J_n$  is unknown coefficient of the  $n$ th segment,  $N$  denotes the number of the segment and  $\mathbf{f}_n(\mathbf{r})$  is a basic function.

Triangle basic function is currently a popular basic function which has good accuracy. In PEC surface, it is known as Rao-Wilton-Glisson (RWG) basis function [121, 122]. The currents of the thin wire in the report is using triangle basic functions represented by  $\mathbf{f}_n(\mathbf{r})$  in Equation 2.7. A thin wire with  $N$  segments is divided by  $N + 1$  points and  $N - 1$  triangle basic functions. Each triangle function is shared by two segments and the value of it varies from 0 at starting point to unit at the dividing point between the segments. It should be noticed that the segments are not required to have equal length. The adjacent basic functions have the overlapped part which gives a piecewise solution. The basic function is given as:

$$f_n(r) = \frac{r - r_{n-1}}{r_n - r_{n-1}} \quad r_{n-1} \leq r \leq r_n \quad (3.8)$$

$$f_n(r) = \frac{r_{n+1} - r}{r_{n+1} - r_n} \quad r_n \leq r \leq r_{n+1} \quad (3.9)$$

Since the EFIE derivation process of a thin wire is similar to that of an arbitrary close surface, the EFIE of thin wire can be derived from Equation 2.6 by converting the surface to linear and combining to Equation 2.7, it is given by:

$$\mathbf{E}_{tan}^i(\mathbf{r}) = (j\omega\mu \sum_{n=1}^N J_n \int_{f_n} \mathbf{f}_n(\mathbf{r}') G(\mathbf{r}, \mathbf{r}') d\mathbf{r}' - \frac{j}{\omega\epsilon} \sum_{n=1}^N J_n \nabla \int_{f_n} \nabla' \cdot \mathbf{f}_n(\mathbf{r}') G(\mathbf{r}, \mathbf{r}') d\mathbf{r}')_{tan} \quad (3.10)$$

The final step of the MoM is to use the basic function as the testing function to discretizing the EFIE. To obtain the impedance matrix from the discretized EFIE, the vector identity

$\Delta \cdot (\phi \mathbf{A}) = \mathbf{A} \cdot (\Delta \phi) + \phi (\Delta \cdot \mathbf{A})$  is applied, the matrix equation is shown:

$$[Z_{mn}] [J_n] = [V_m] \quad (3.11)$$

where,

$$Z_{mn} = j\omega\mu \int_{f_m} \mathbf{f}_m(\mathbf{r}) \cdot \int_{f_n} \mathbf{f}_n(\mathbf{r}') G(\mathbf{r}, \mathbf{r}') d\mathbf{r}' d\mathbf{r} - \frac{j}{\omega\epsilon} \int_{f_m} \nabla \cdot \mathbf{f}_m(\mathbf{r}) \int_{f_n} \nabla' \cdot \mathbf{f}_n(\mathbf{r}') G(\mathbf{r}, \mathbf{r}') d\mathbf{r}' d\mathbf{r} \quad (3.12)$$

$$V_m = \int_{f_m} \mathbf{f}_m(\mathbf{r}) \mathbf{E}^i(\mathbf{r}) \quad (3.13)$$

### Conventional Derivation of CM

In electromagnetic, CM theory converts the natural property of a structure to the eigenvalues and eigenvector [118]. They describe the radiation and scattering of the structure. The impedance matrix of a thin wire represents the natural impedance property. Given in Equation 2.12, the impedance matrix  $Z$  can be represented by real and imaginary Hermitian parts:

$$\mathbf{Z} = \mathbf{R} + j\mathbf{X} \quad (3.14)$$

$$\mathbf{R} = \frac{\mathbf{Z} + \mathbf{Z}^*}{2} \quad (3.15)$$

$$\mathbf{X} = \frac{\mathbf{Z} - \mathbf{Z}^*}{2j} \quad (3.16)$$

According to the theory of Harrington and Mautz [123],  $R$  and  $X$  are real and symmetric matrices. The generalised eigenvalues  $\lambda_n$  and characteristic currents  $\mathbf{J}_n$  can be derived as:

$$\mathbf{X}\mathbf{J}_n = \lambda_n \mathbf{R}\mathbf{J}_n \quad (3.17)$$

Since  $R$  and  $X$  are symmetric,  $\lambda_n$  and  $\mathbf{J}_n$  are real. Proved in [118], the  $\mathbf{J}_n$  is orthogonal with  $R$  and  $X$ . Thus, the characteristic of  $\mathbf{J}_n$  is reflected in the current polarization and the current phase are orthogonal to each other.

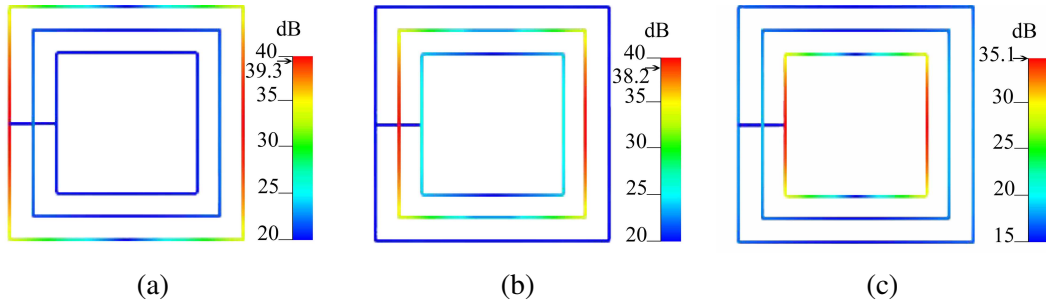


Fig. 3.1 Normalised current distribution on grid antenna, (a), (b) and (c) represent the current distributions of mode 1, mode 2 and mode 3 at their resonance frequencies

The value of  $\lambda_n$  describes the resonant performance of the antenna, positive, negative and zero values corresponding to the inductive, capacitive and resonant modes respectively. To observe the mode resonance more intuitively, model significance (MS) is defined as:

$$MS = \frac{1}{|1 + j\lambda_n|} \quad (3.18)$$

MS provides a better visualisation on resonance frequency and bandwidth. The value of the MS approach to 1 indicates that the mode of the antenna has a resonance at the frequency.

By applying CMA to a metal structure, the data of the MS, surface current and radiation pattern can be obtained, which can be a guide for antenna structure modification. A multiband antenna with good performance should have multiple resonance frequency points, which means the values of the MS close to 1 repeatedly within the simulation frequency range. Simultaneously, the characteristic modes with inhomogeneous radiation field at the resonance point should be eliminated, because the homogeneous radiation field will improve the indoor signal coverage performance. Furthermore, the optimisation of the structure targets that the resonance frequencies of modes can be determined independently by the sizes of the grids, meanwhile, interferences between the grids should be limited in an acceptable range.

### Antenna Design using CMA

The proposed antenna utilises a grid structure obtained through the application of CMA for guided optimisation. This grid-based design is engineered to exhibit resonant behaviour at

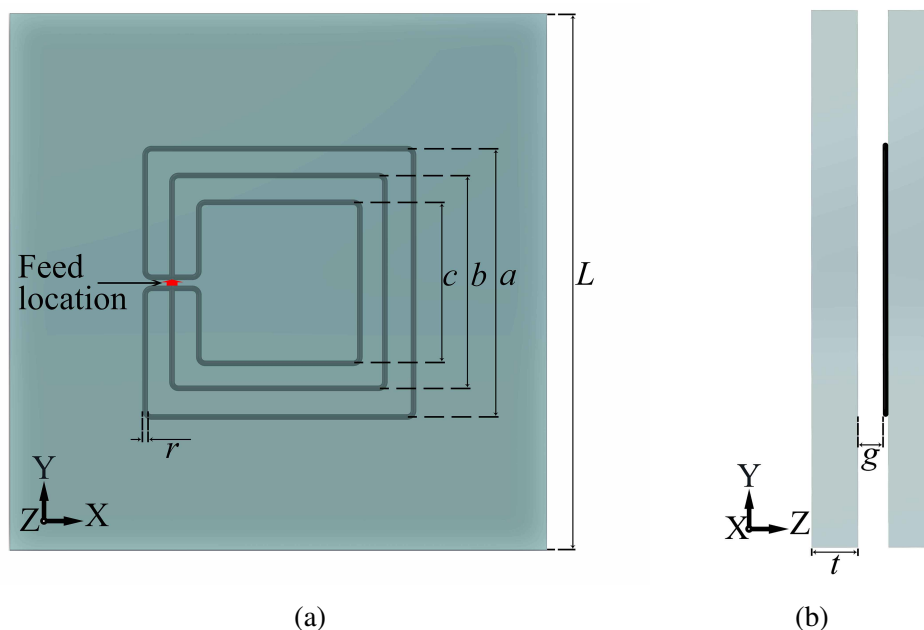


Fig. 3.2 Overall version of antenna design that is integrated within the glass pieces, where  $a = 28$  mm,  $b = 23$  mm,  $c = 17.4$  mm and  $L = 2a$ , the thickness of glass is  $t = 5$  mm, the gap is  $g = 3$  mm and the radius of the wires is  $r = 0.3$  mm. (a) is the front view and (b) is the right view.

multiple frequencies. To achieve a triple-band resonance capability, the antenna employs three grids of varying sizes, each corresponding to a distinct resonance frequency. Notably, a key challenge revolves around efficiently exciting these three mesh grids, given their disparate resonant frequencies. Leveraging the power of CMA, all resonant modes for the three grids at the designated frequency range are identified. Through an intricate analysis of the current distribution associated with these modes, three approximated resonant modes are selected, as depicted in Fig. 3.1. These grids uniformly manifest approximate resonant currents along the vertical orientation, facilitating the intriguing possibility of effectively exciting all three grids using a single feed. To exploit this characteristic, we strategically positioned at the centre of left sides of the grids. Placing the feed source at this precise connection wire location engenders the remarkable outcome of achieving triple-band resonance.

By continuously optimising, a structure with good performance is accomplished as shown in Fig. 3.2, as the grid-in-grid structure exhibits its superiority on multiband resonance and homogeneous radiation. The Matlab code for CMA applying on the thin wire antenna shape

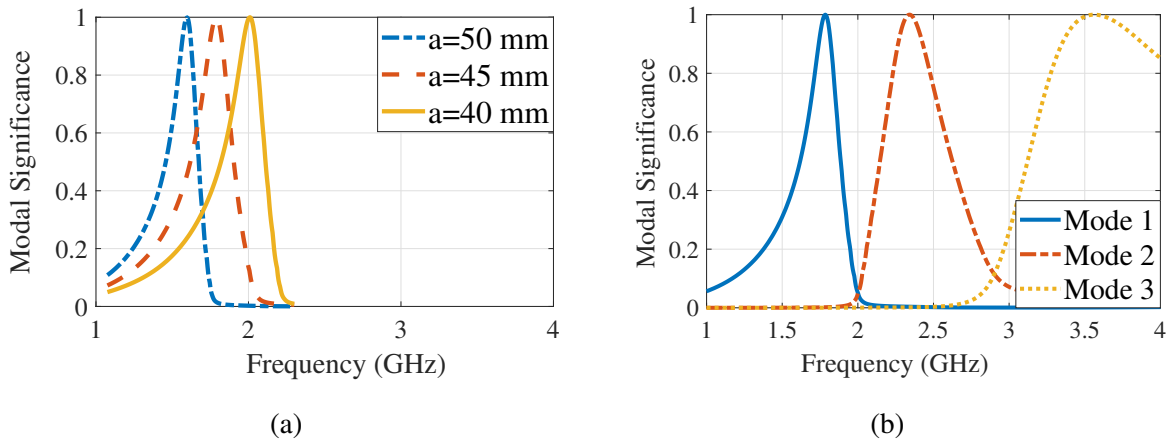


Fig. 3.3 (a) MS of mode 1 in Figure 3.2(a) with different size of the outer frame, (b) triple-band resonance performance in free space. The side lengths of each grid in the antenna are  $a = 45$  mm,  $b = 34$  mm and  $c = 24$  mm.

is shown in Appendix. Fig. 3.1 depicts the current distribution of the selected modes. Fig. 3.1(a)-(c) correspond to 2.7, 3.5 and 5 GHz at free space, they present approximate current distributions after integrated to the glass. The radiation patterns of them are similar to that of a pair of parallel dipoles. Fig. 3.3(a) shows the frequency adjustability of the antenna by tuning the side length of the outer grid. Accordingly, the antenna with triple-band resonances is tuned to satisfy the most common use frequency bands, as shown in Fig. 3.3(b), the MS shows the resonances are at 1.8 GHz, 2.4 GHz and 3.5 GHz.

### 3.1.2 Feeding Refinement and Glass Integration

CMA revealed the availability of the grid-in-grid structure in free space, however, the feed and dielectric materials limit the mode excitations and radiation efficiency. Excite multiple modes with a single feed depends largely on the similarity between the modes. As shown in Fig. 3.2, the selected modes of the proposed design have similar current distribution except for dimension and the high-current location is in the connecting wire. Similar to the feed for dipole, one side of the grids are disconnected and two connecting wires are placed to connect the grids then feed as shown in Fig. 3.1(a). Double-layer glass with wires is one of the popular structures of commercial explosion-proof and burglar-proof windows. As shown

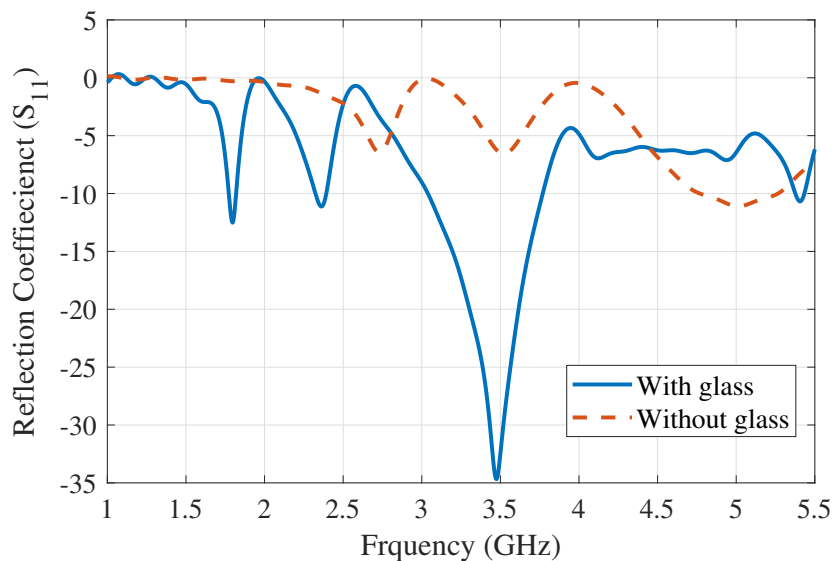


Fig. 3.4 The reflective coefficient ( $S_{11}$ ) of the antenna in free space and integrated with glass.

in Fig. 3.1(b), the antenna is sandwiched by the glass pieces, attaches to a face of a piece of glass and have few millimetres gap with another.

The simulation results in CST Microwave Studio obtained by Time Domain Solver indicates that the combination of glass varies the resonance frequencies and reflection coefficients. By optimising the lengths of the grids, the dimension of the glass-integrated antenna is shown in Fig. 3.1. Fig. 3.4 compares the reflective coefficients ( $S_{11}$ ) of the antenna with and without the glass. The integration of glass reduces the resonance frequency and of each mode, as the resonance frequencies in free space at 2.7 GHz, 3.5 GHz and 5 GHz are reduced to the desired frequencies. In this case, the resonant frequency bands of the antenna are 1.8 GHz (5.6%), 2.4 GHz (8.3%) and 3.5 GHz (20.2%). The special designed bands can provide service for GSM, LTE and WLAN and low-frequency band for 5G and private LTE communication.

As the radiation pattern of the antenna in free space in Time Domain Solver are generally the same as that in Integral Equation Solver (CMA method), the single feed proves its availability. Fig. 3.5 shows the radiation patterns of the glass-integrated antenna. At 1.8 and 2.4 GHz, the antenna exhibits broadside and uniform radiation patterns in the  $xz$ -plane and  $yz$ -plane, while the pattern at 3.5 GHz shows strong front radiation in the  $xz$ -plane and

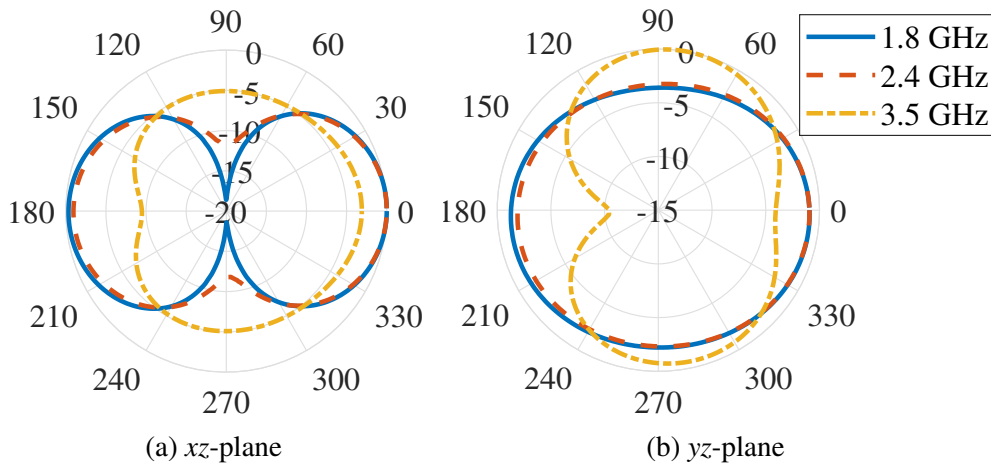


Fig. 3.5 Radiation patterns of the glass-integrated antenna at the resonance frequencies of 1.8 GHz, 2.4 GHz and 3.5 GHz at (a)  $yz$ -plane and (b)  $xz$ -plane

relatively weaker front radiation in the  $yz$ -plane. As the resonant frequency increases, the antenna radiates more power in the direction from the antenna to the glass with a gap, as a result, the antenna attached on the inner face of the outer glass of the double-layer windows performs better for indoor communications.

### 3.1.3 Conclusion

In conclusion, a tri-band glass-integrated antenna is designed and optimised for indoor communication based on CMA. The antenna has a simple grid structure with a single feeding, and each operating mode can be tuned flexibly. Moreover, the antenna can be integrated with glass as metal grid. This work demonstrates the feasibility of window integrated antenna to realize indoor multi-band communications.

## 3.2 CPW-Fed TAA Using Wired MM

### 3.2.1 Introduction

The deployment of indoor BSs constructed by large-scale antenna arrays is constrained by many factors, including space, beauty and concealment. The antenna adapted to the indoor base station should have the characteristics of small size, easy installation and concealment

[124]. Therefore, using the TA that is attached to the surface of dielectric materials could be a choice. Over the past years, the TAs are mainly using two forms: TCF and conductive meshes [26]. In contrast, the TA using wired MM obtains optical transparency and has comparable gain and efficiency performance to traditional metal antennas [60, 125]. In buildings, the main material that needs to transmit light is glass. MM structure with high performance can be a good choice.

Based on the CPW-fed antenna array, a TAA is proposed in this section by using the MM structure. The objective of the present antenna array is to obtain the maximum light transmittance with acceptable antenna array performance. In order to adapt to the medium where the antenna is attached, the original CPW-fed antenna array is redesigned. By using the MM structure to replace the ground plane, feed line and antenna body of the designed antenna array, the light transmittance is improved. The commonly used glass is the substrate of the proposed TAA as it allows the TAA to be deployed on many building structures.

### 3.2.2 Antenna Design

The principle and methods of research will be disclosed through the designed CPW-fed TAA with MM structure at 2.4 GHz indoor wireless communications.

#### a. CPW-fed Antenna Unit Design

The CPW-fed antennas serving the TAA are different from the conventional CPW-fed antenna. The substrate of the TAA units is glass with a 6.15 dielectric constant. In the CPW-fed antenna array, the ground planes of each unit should be connected. Thus, the patch of the unit is surrounded by the ground plane. The antenna unit is shown in Fig. 3.6(a). To satisfy the frequency band of indoor wireless devices, the design working frequency of the transparent antenna array is set at 2.4 GHz. As the array construction will affect the overall operating band, the centre resonant frequency of the unit is set to 2.8 GHz. The reflective coefficients of the unit are shown in Fig. 3.6(b). The band of  $S_{11}$  less than -10 dB is from 2 GHz to 3.1 GHz. The resonant frequency is mainly affected by the dimension of the patch and the distance between the sides. The desirable resonant band is around 2.8 GHz for the element

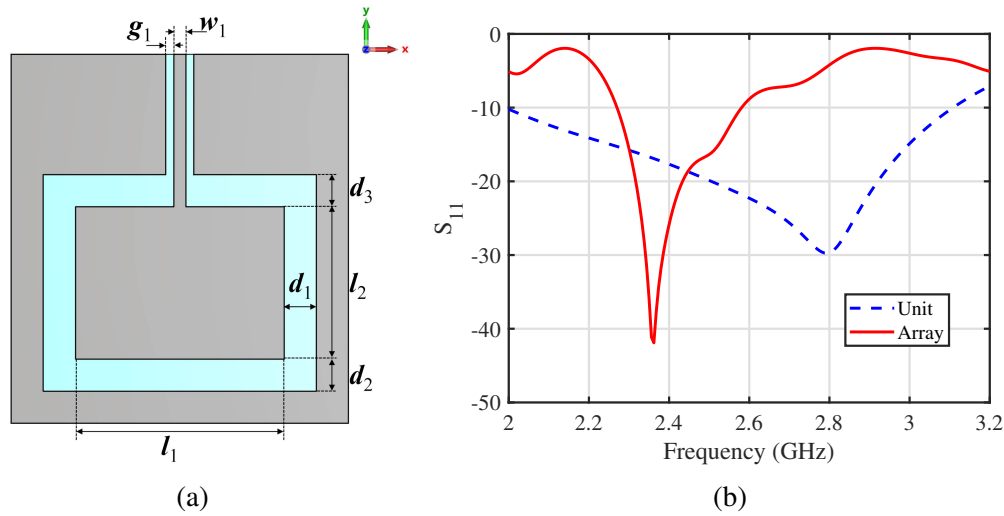


Fig. 3.6 (a) The top view of the CPW-fed antenna unit where  $l_1=21$  mm,  $l_2 =16$  mm , the gap  $d_1 = d_2=7.5$  mm ,  $d_3 =7$  mm,  $g_1=0.9$  mm and the feed line width  $w_1=1$  mm, (b) the reflective coefficients of antenna unit and opaque antenna array..

antenna. The initial shape of the patch is square so the length should close to a quarter wavelength (around 27 mm). After forming the elements to an antenna array, the length of each edge, gaps between patch and ground and distance between the elements are further optimised by sweeping the parameters. In Fig. 3.6(a), the optimised dimension and distance are shown. Increasing the distance  $d_1$  and  $d_2$  will decrease the resonant frequency and the coupling. Increasing the distance  $d_3$  between the top side of the patch and the ground plane will increase the resonant frequency dramatically. The side lengths  $l_1$  and  $l_2$  of the patch are inversely proportional to the resonant frequency. While the distance between elements  $d_4$  close to half wavelength (63 mm) and quarter wavelength (31 mm), the coupling are more relative strong. Considering that small  $d_4$  will cause greater coupling, and the overall size of the array should not be too large,  $d_4$  is set to around  $1/3$  wavelength.

### b. Antenna Array and Feed Line Design

The TAA consists of 4 CPW-fed antenna units as demonstrated in the previous subsection. The antenna units are placed at the same height on the same plane. The range of the distances  $d_4$  between the units is determined by the operating frequency which is set to  $d_4 = 44$  mm. In Fig. 3.7, the structure of the CPW-fed antenna array is shown. The characteristic impedance

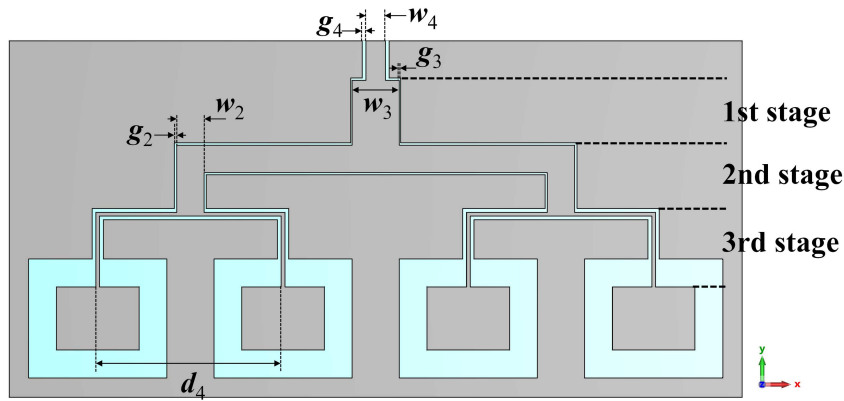


Fig. 3.7 The top view of the CPW-fed antenna array where  $g_2=0.5$  mm,  $w_2=7$  mm,  $g_3=0.3$  mm,  $w_3=12$  mm,  $g_4=0.9$  mm,  $w_4=5$  mm and the units distance  $d_4=44$  mm. Stage 1, 2 and 3 are the impedance matching stages.

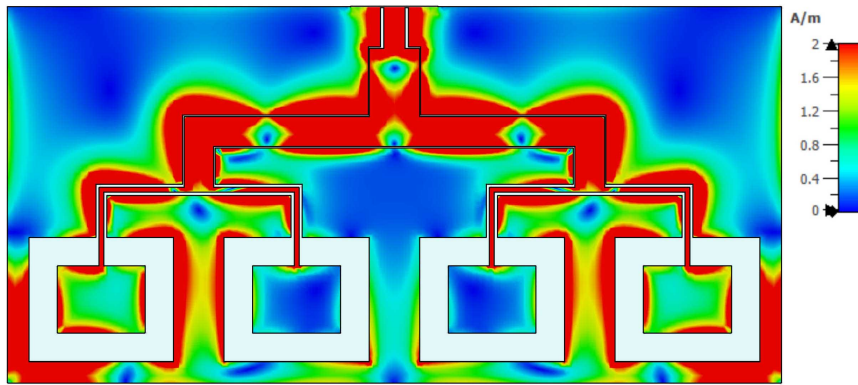


Fig. 3.8 The current distribution of opaque antenna array.

in the third transmission stage are  $75 \Omega$ , the impedance of the feed line in the second transmission stage should be  $37.5 \Omega$ . At the boundary of the first and second transmission stages, the characteristic should be equal to half of that at the second stage which is  $18.75 \Omega$ . In order to convert the characteristic impedance at the boundary to match the input impedance, a quarter-wave impedance transformer is applied. By calculating using (3.19), the impedance of the quarter-wave impedance transformer can be obtained,

$$R_t = \sqrt{R_1 \times R_2} \quad (3.19)$$

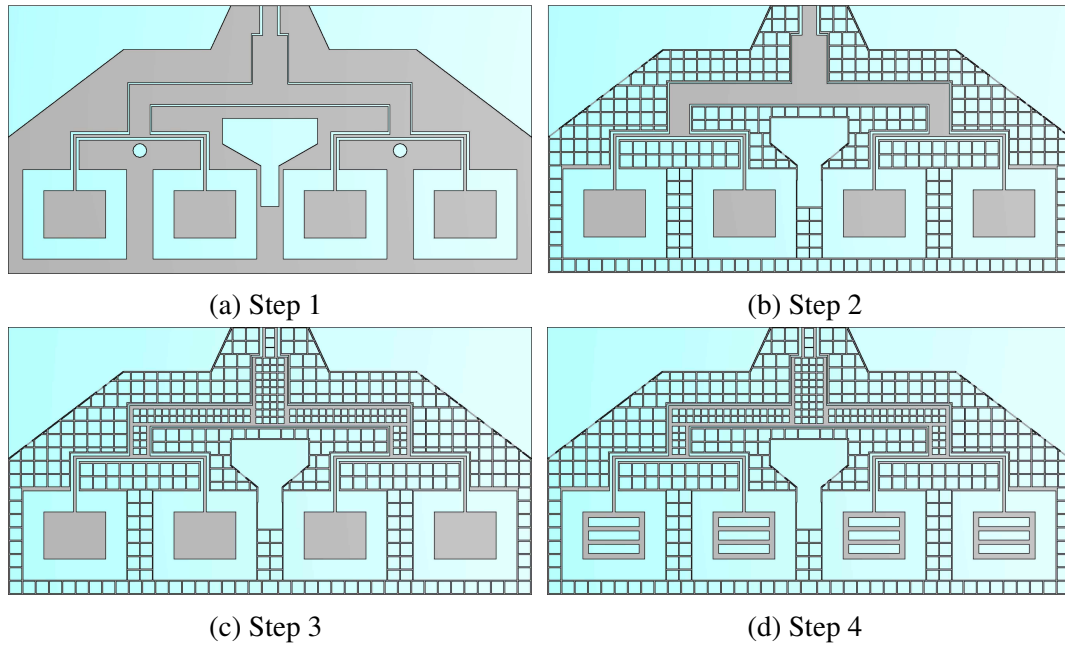


Fig. 3.9 The processes of the transparency treatment. (a) is the cut antenna array, (b) applying large meshes on the ground plane, (c) applying small meshes on feed line and (d) slotting on patches.

where  $R_t$  is the impedance of the quarter-wave impedance transformer,  $R_1$  is the input impedance and  $R_2$  is the characteristic impedance of the transmission line. In this antenna array, the impedance of the transformer is  $30.6 \Omega$ . The length of it is 16.4 mm. In addition, a  $50 \Omega$  transmission line is connected at the end of the quarter-wave impedance transformer. The antenna array is designed for 2.4 GHz. As shown in Fig. 3.6(b), due to the close placement of the elements will generate coupling, the centre resonant band of the antenna array is reduced compared with the band of the unit. The bandwidth is reduced but the  $S_{11}$  is decreased at around 2.4 GHz.

### 3.2.3 Transparent Treatment of the Antenna Array

The transparent treatment aims to reduce the shading area of the antenna array. In the traditional CPW-fed antenna array, the surface current is concentrated on the feed line, patches and their surrounding parts. The area with weak current has very weak effect on the performance of the antenna array. Therefore, the part where the current is low will be cut

off. Fig. 3.8 shows the current distribution of the opaque antenna array. (3.20) defines the transparency [76],

$$\text{Transparency} = \frac{A_{\text{cut-out}}}{A_{\text{total}}} \times 100\% \quad (3.20)$$

where  $A_{\text{cut-out}}$  is the cut out area and  $A_{\text{total}}$  is the total area. By comprehensively evaluating the influence of the transparency on transmittance, radiation pattern, reflective coefficient and bandwidth, the shape in Fig. 3.9(a) is obtained. The  $S_{11}$  of it is similar to that of the antenna array without cutting.

### a. Transparent Treatment of the Ground Plane and Feed Line

Using mesh structure to replace the whole metal board can greatly increase light transmittance. Under the condition that the working mode can be excited, the main purpose is to increase the transparency as much as possible. In areas with low currents, large meshes are applied to replace the original metal plates, while areas with high currents require small and dense meshes. Compared with the feed line, the current on the ground plane is sparser. Therefore, larger meshes should be applied to the ground plane while the feed line uses smaller meshes. On the edges of the patches, feed line and some parts of the ground plane, the current values are always higher than the other parts. Thus, the edges are using thicker wires. The transparent treatment processes are shown in Fig. 3.9. Fig. 3.9(b) shows a meshed ground plane using large meshes, Fig. 3.9(c) shows the transparent treatment to feed line with small and dense meshes. Since the broken edge will affect the radiation field, the edges of the ground plane remain connected.

### b. Slotting of the Patches

Patches distribution with dense current is the key to resonance. Mesh processing will affect the radiation pattern, resonance frequency and even change the original working mode. Slotting the patches is better than simply using meshes as the slots can control the working mode. Fig. 3.9(d) shows the slotted antenna which is the final step of the transparent treatment. Each patch has 3 rectangular slots. The slots with the dimension of  $17 \times 3 \text{ mm}^2$

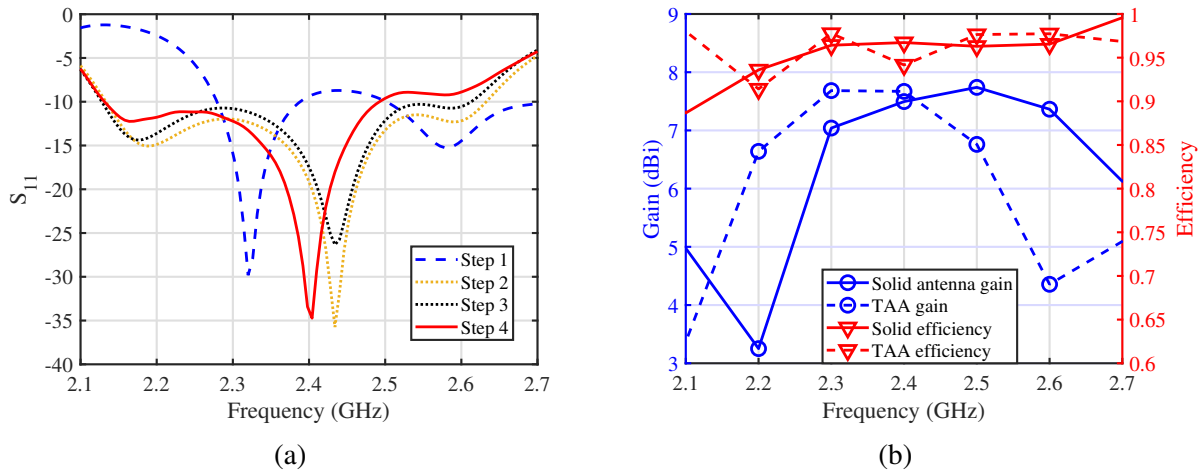


Fig. 3.10 (a) The resonant performance of the antenna array while doing the transparent processes. The Step 1, 2, 3 and 4 correspond to the models in Fig. 3.9 (a), (b), (c) and (d), (b) the gain and radiation efficiency of the solid antenna and TAA.

are designed based on the current distribution. It could be noticed that the horizontal current dominates the patch, and the vertical current in Fig. 3.8 comes from the coupling effect between the patches. The slots have the effect of gathering the horizontal current and weakening the coupling current.

### 3.2.4 Results and Discussion

By simulation using a variety of meshes from small to large, the optimised meshes are obtained. The  $4 \times 4$  mm<sup>2</sup> meshes for the ground plane and  $2 \times 2$  mm<sup>2</sup> meshes for the feed line are considered to be an optimal combination. Fig. 3.10(a) compared the reflective coefficients of each step in Fig. 3.9. The transparent treatment can slightly increase the resonant frequency. The resonant band of the final version of TAA in step 4 is from 2.12 GHz to 2.5 GHz. Fig. 3.10(b) shows the gain and radiation efficiency of the TAA and solid antenna array. The maximum gain of TAA is 7.6 dBi at 2.3 GHz and 2.4 GHz. Relative to its solid counterpart, the peak gains exhibit an approximate nature. Following the transparent process, a downward shift of 0.2 GHz is observed in the frequency of the peak gain. The efficiency of the TAA is remaining higher than 90% within the working band, which is comparable with the efficiency of the solid antenna. Fig. 3.11 shows the radiation patterns

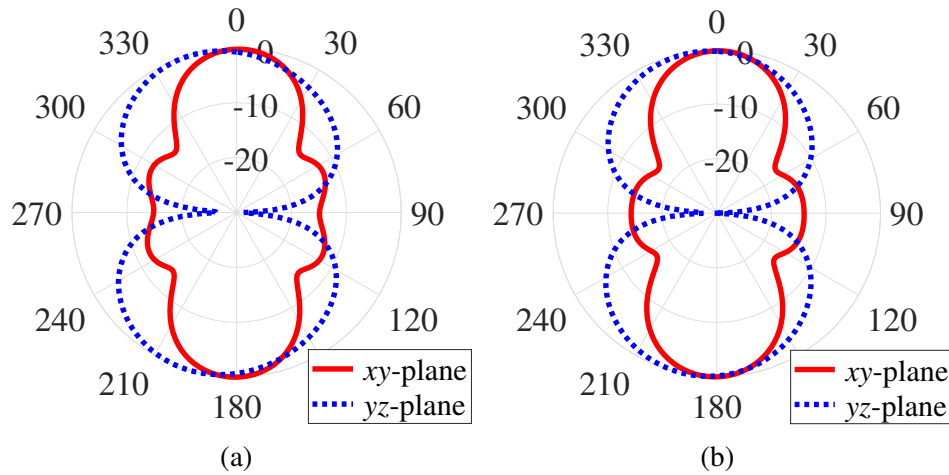


Fig. 3.11 The radiation patterns: (a) the original CPW-fed antenna array, (b) the final version of the TAA.

Table 3.1 COMPARISONS OF TRANSPARENT ANTENNAS

Ref.	Units	Technology	Transparency	Maximum Gain	Efficiency
[41]	2	ITO MIMO	72%	2 dBi	60%
[55]	4	Micro mesh	84%	7.2 dBi	78%
[60]	1	Large mesh	93%	5.3 dBi	-
This work	4	Large mesh	80%	7.6 dBi	90%

of the opaque antenna array and the TAA at 2.4 GHz. Both of them show a broadside pattern. The radiation pattern remains its features after the transparent treatment.

In Table 3.1, the other TAs are compared with the proposed antenna. The transparency of the proposed TAA is less than [55, 60] but the TAA also achieves good transparency. The maximum gain and efficiency of the TAA are better than other works. The TAA is made by the meshes that can be seen by eyes, the minimum width of the wire between the meshes is 0.5 mm which has a very limited effect on the impedance. Thus the loss of the antenna is much less than the TA made by micro metal mesh with nanometre scale meshes such as [55] and TCFs [41] with poor conductivity.

### 3.2.5 Conclusion

A CPW-fed TAA with four units is proposed. The TAA operates at a frequency band from 2.12 GHz to 2.5 GHz which can serve for indoor wireless applications. 80% transparency achieved allows the TAA to be deployed on the glass surface with little impact on the light transmittance. The transparency is obtained by hollowing out different sizes of meshes on the opaque conducting part. The large size meshes remain good conductivity of the antenna. The maximum gain of the TAA is 7.6 dBi and efficiency is more than 90%. High gain and high efficiency TA met the space and communication requirements of large scale BS applying indoors can promote the next generation communication development.

## 3.3 A Transparent Antenna Using Metal Mesh for UWB MIMO Applications

### 3.3.1 Introduction

To satisfy the increasing traffic demand, dense deployments of indoor small BSs based on the MIMO antenna array are expected [126, 127]. However, densely deployed small BSs have adverse effects on the usage and the aesthetic of the room. TAs are therefore explored to alleviate this contradiction [66, 128]. It is anticipated that TAs will be widely used in future buildings, especially in the smart building era [1].

Compared with TCF and micro MM, wired MM is inferior in terms of transparency since relatively thick metal wires obscure part of the light. Even so, transparency larger than 70% can be obtained by designing the pattern of the wired mesh carefully [80]. More importantly, wired MM has thicker strands than micro MM to realize a much lower resistance. The efficiency of wired MM antennas is comparable to that of non-transparent metal antennas. In addition, wired MM TA can be built on various substrates, regardless the substrate is transparent or opaque. Therefore simple fabrication methods such as PCB technique can be used to fabricate wired MM, which reduces the cost of wired MM antennas [64]. When the

requirement of transparency is not very stringent, wired MM TA is a good choice since it exhibits excellent radiation performance [57, 129, 130].

To meet the requirement of large capacity and spectral efficiency in indoor communication, ultra-wideband (UWB) MIMO antennas are essential to enhance the data rate. The main issue of the metal UWB MIMO antenna is the mutual coupling. High isolations in UWB MIMO system were obtained by a tree-like structure in [131], meandered lines in [132], metal strip in [133], a branch and a T-shaped slot in [134] and orthogonal characteristic modes in [135]. To facilitate the deployment, it is highly desirable to develop transparent UWB MIMO antenna. Recently, several designs of transparent MIMO antennas were presented based on TCF [40, 41, 69, 71] and micro MM [53, 54]. However, UWB MIMO TA based on wired MM has not been reported, as it is challenging to design a suitable decoupling structure based on wired MM while maintaining high isolation and transparency at the same time.

This section proposes a wired MM transparent antenna with a parasitic decoupling structure for UWB MIMO applications. Compared to the current transparent MIMO antennas, it has relative wider bandwidth, higher efficiency, higher gains, lower coupling and comparable transparency. 77% transparency is achieved by hollowing out both metal and substrate into a mesh shape while maintaining more than 83% radiation efficiency. The antenna consists of four elements which produce dual-polarized radiation and a wide operating band from 3.2 GHz to 11.2 GHz. A parasitic decoupling structure aligned with the mesh grid is designed to enhance the isolation between MIMO elements without degrading the transparency. The isolation between MIMO elements is more than 20 dB within the whole operating band. The proposed UWB MIMO antenna exhibits excellent diversity performance and time domain response. The antenna is fabricated based on conventional PCB and laser cutting techniques which make this antenna easy to be manufactured with a low cost.

### 3.3.2 Element Design

The proposed UWB MIMO TA is comprised of 4 elements. Each element is an independent UWB TA. The antenna is mounted on an FR-4 substrate with a thickness of 0.6 mm, the

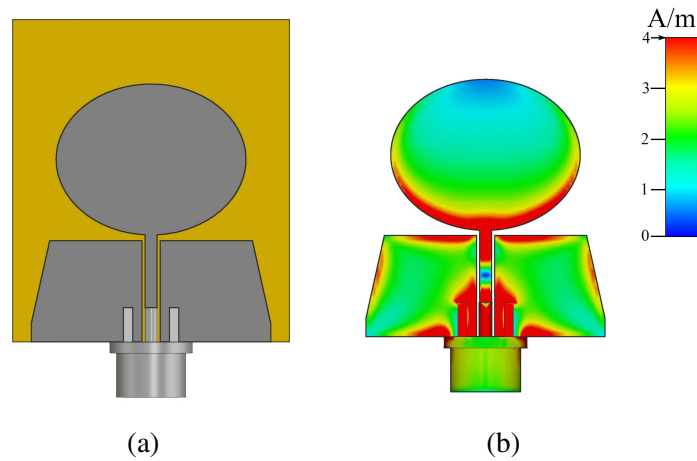


Fig. 3.12 The CPW-fed UWB element and its current distribution at 4 GHz: (a) opaque element, (b) current distribution of opaque element.

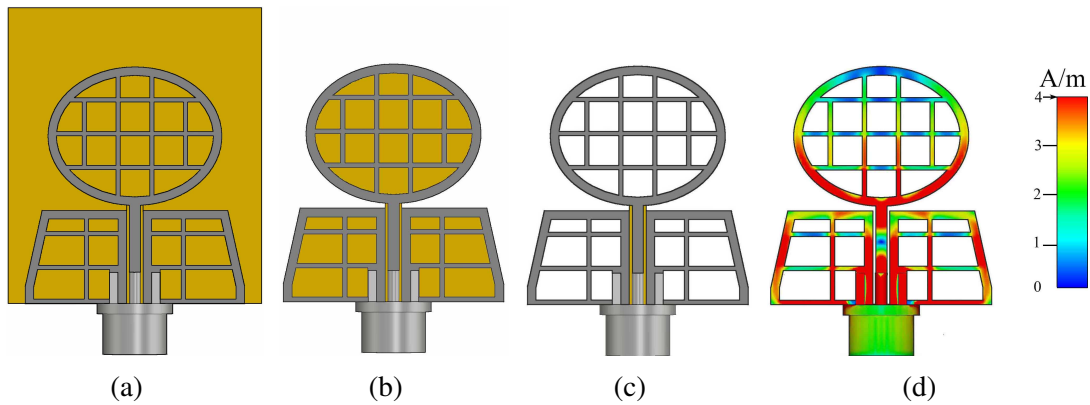


Fig. 3.13 The transparent processing steps: (a) step 1, (b) step 2, (c) step 3 is the final version of UWB transparent element. (d) is current distribution of the transparent element.

dielectric constant of 4.4 and loss tangent of 0.025. All simulations in this paper were performed by CST Studio Suite 2021.

#### a. UWB Element

The proposed UWB element is presented in Fig. 3.12(a), in which the metal is depicted in grey and the substrate is depicted in orange. The antenna element fed by a CPW transmission line is designed on a single metallic layer. The ground with chamfered cut can improve broadband impedance matching. The proposed UWB MIMO element is a variant of monopole antenna. The radiation part of the element is an ellipse monopole which has expanded shape and

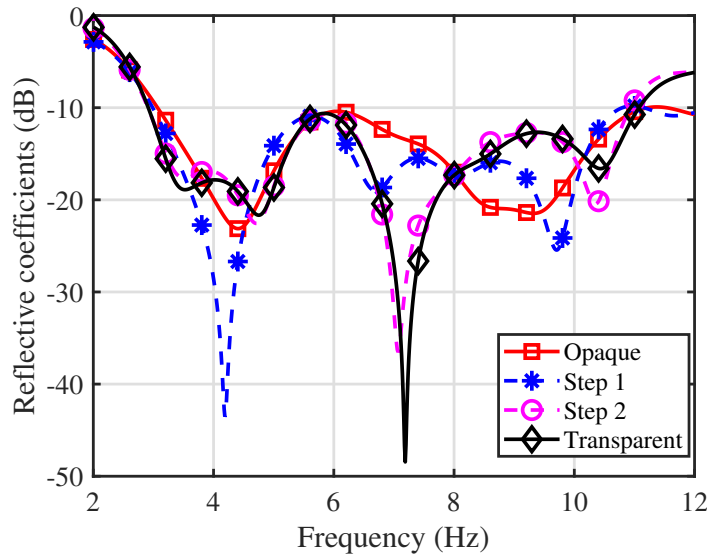


Fig. 3.14 The reflective coefficients of the opaque, Step 1, Step 2 and transparent element corresponding to Fig. 3.12(a), Fig. 3.13(a), (b) and (c).

relatively smooth transition from the feeding line, therefore it exhibits wideband characteristic. The simulated  $S_{11}$  of the UWB element is shown with the red line in Fig. 3.14, the bandwidth for  $S_{11}$  below -10 dB is from 3.1 GHz to 11.3 GHz. The current distribution of the opaque UWB element at 4 GHz is shown in Fig. 3.12(b). It can be seen that the current is mainly distributed on the central conductor of CPW, the edge of the ground and the lower edge of the ellipse monopole, while the current in the middle part of the ground and patch is weak. Based on this observation, it is possible to hollow out the element into a mesh shape to make it transparent without changing its radiation characteristics.

### b. Transparent Processing

The transparent element is optimised from Fig. 3.12(a) in 3 steps. In the first step, the metallic layer of the antenna is meshed by open squares with a size of  $3.5 \times 3.5 \text{ mm}^2$  as shown in Fig. 3.13(a). In order to facilitate the fabrication, the small meshes near the edge and corner are merged into the adjacent meshes. The widths of the metal lines in the middle of the ground and ellipse monopole are set to be 0.5 mm since the current is weak in these areas. In contrast, the widths of the metal lines at the edge of the ground and ellipse monopole

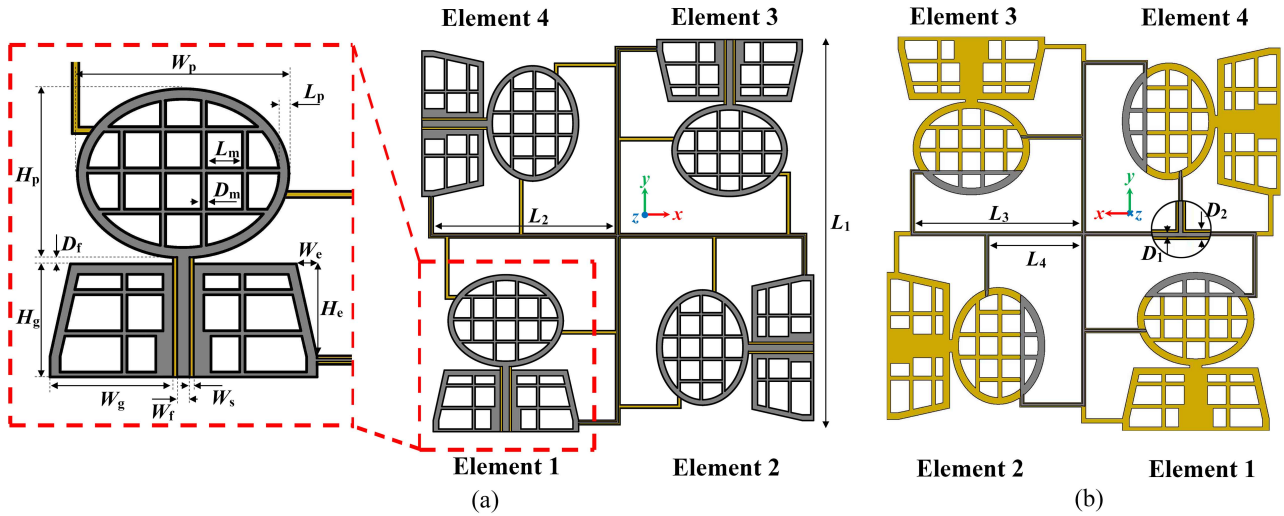


Fig. 3.15 Geometry of the proposed UWB MIMO TA: (a) front view, (b) rear view. The detail dimension is presented in Table 3.2. Grey and orange colour represent metal and FR-4 substrate, respectively.

Table 3.2 DIMENSIONS OF THE PROPOSED ANTENNA

Parameter	$W_g$	$W_f$	$W_s$	$W_p$	$W_e$	$H_p$	$H_g$	$H_e$	$L_m$	$L_1$	$L_2$	$L_3$	$L_4$	$D_m$	$D_1$	$D_2$
Value (mm)	12	1.3	0.34	20.6	2	16.4	11	9	3.5	70	32.8	29.9	16.7	0.5	0.3	0.6

are set to be 1 mm to ensure a low resistance for large current. To allow the current pass through it smoothly, the central conductor of CPW is not meshed since it has the strongest current. Then the substrate outside the antenna frame is cut out as shown in Fig. 3.13(b). In step 3, the substrate inside the antenna frame is hollowed with the same mesh pattern as the metallic layers. The final version of the transparent element is shown in Fig. 3.13(c). It is worth noting that the substrate near the central conductor of CPW is kept intact as it has a large impact on impedance matching.

The current distribution of the transparent element at 4 GHz is shown in Fig. 3.13(d), which is very similar to that of the opaque UWB element shown in Fig. 3.12(b). It indicates the operating mode of the element is kept the same before and after the transparent processing. In Fig. 3.14, the simulated  $S_{11}$  of each step from opaque to transparent are shown. We can see that despite  $S_{11}$  varies during hollowing, especially at high frequency 6-10 GHz, the operation band is unchanged and  $S_{11}$  are well below -10 dB from 3.0 GHz to 11.3 GHz.

The transparency  $T$  of metal mesh can be calculated by (3.20) and the transparency of the proposed UWB element is 73%.

### 3.3.3 Array Design

Four transparent elements described above are employed to construct a UWB MIMO TA, whose geometry is shown in Fig. 3.15. The whole MIMO antenna occupies an area of  $70 \times 70 \text{ mm}^2$ . The dimensions of the antenna are presented in Table 3.2. The antenna elements and feeding lines are printed on the top layer of the substrate while the parasitic decoupling structure is on the bottom layer. The adjacent elements are placed orthogonally to produce dual-polarised radiation. The two elements on the diagonal have the same polarisation. The entire MIMO TA is rotationally symmetric. According to the transparency defined in (3.20), the transparency of the four-element MIMO antenna array is 77%.

#### a. Connection Structure

Initially the four elements are connected by a thin outer frame shown in Fig. 3.16(a), whose  $S$ -parameters are shown in Fig. 3.17(a). Since the antenna array is rotationally symmetric,  $S_{41}$  is the same as  $S_{21}$ , so only  $S_{11}$ ,  $S_{21}$  and  $S_{31}$  are shown.  $S_{11}$  indicates that the bandwidth of the antenna is from 2.5 GHz to 10.2 GHz. However,  $S_{21}$  and  $S_{31}$  are larger than -20 dB in some frequency bands, especially the mutual couplings exceed -15 dB at around 3.4 GHz.

To improve the mutual coupling, a criss-crossing network is invented to replace the initial connection frame. As shown in Fig. 3.15(a), the ground planes of the four elements are connected by the network across the centre of the array. Based on the ground plane connection, two additional connections are made on the edge of the patch of each element by extending the FR-4 substrate. The extended criss-crossing network not only improves the mechanical robustness, but also creates more design space for the decoupling structure on the back of the array as shown in Fig. 3.16(b).  $S$ -parameters of the antenna with criss-crossing network are shown in Fig. 3.17(b). The bandwidth is from 2.8 GHz to 10.8 GHz. The orthogonal placement of adjacent elements not only generates dual polarisation but also limits the coupling. Despite the distance is small between the adjacent elements, the mutual

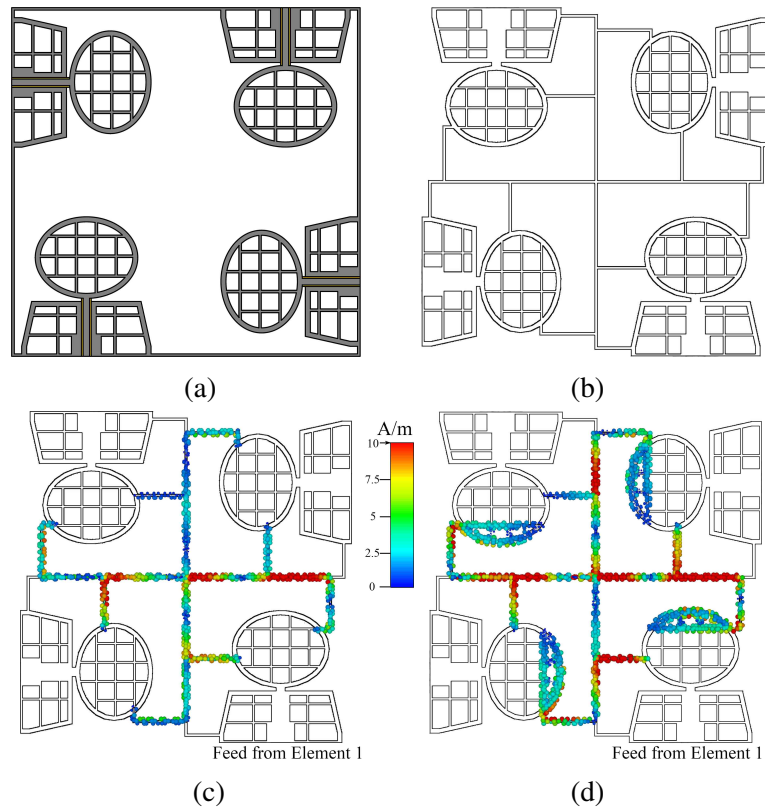


Fig. 3.16 The evolution of the connection and decoupling structure. (a) is the front view, (b), (c) and (d) are the rear view. (a) to (b) is the element connection optimisation and (b), (c) and (d) are the parasitic decoupling structure optimisation with their current distribution at 4 GHz.

coupling between them presented by  $S_{21}$  is lower than -20 dB over the whole band. However, the coupling between diagonal elements presented by  $S_{31}$  is larger, especially in the lower frequency band. For example, it exceeds -20 dB at around 3.3 GHz. Since the mutual coupling will reduce the efficiency of the MIMO system, a proper decoupling network needs to be implemented.

### b. Decoupling Structure

Compact placement leads to strong coupling between elements. In our design, the coupling between the diagonal elements is large since they are in the same polarisation. There are a number of decoupling structures that can enhance the isolation between MIMO antenna elements. However, the proposed meshed UWB MIMO antenna put forwards higher requirements on the decoupling structure. Firstly, the decoupling structure should be conformal to

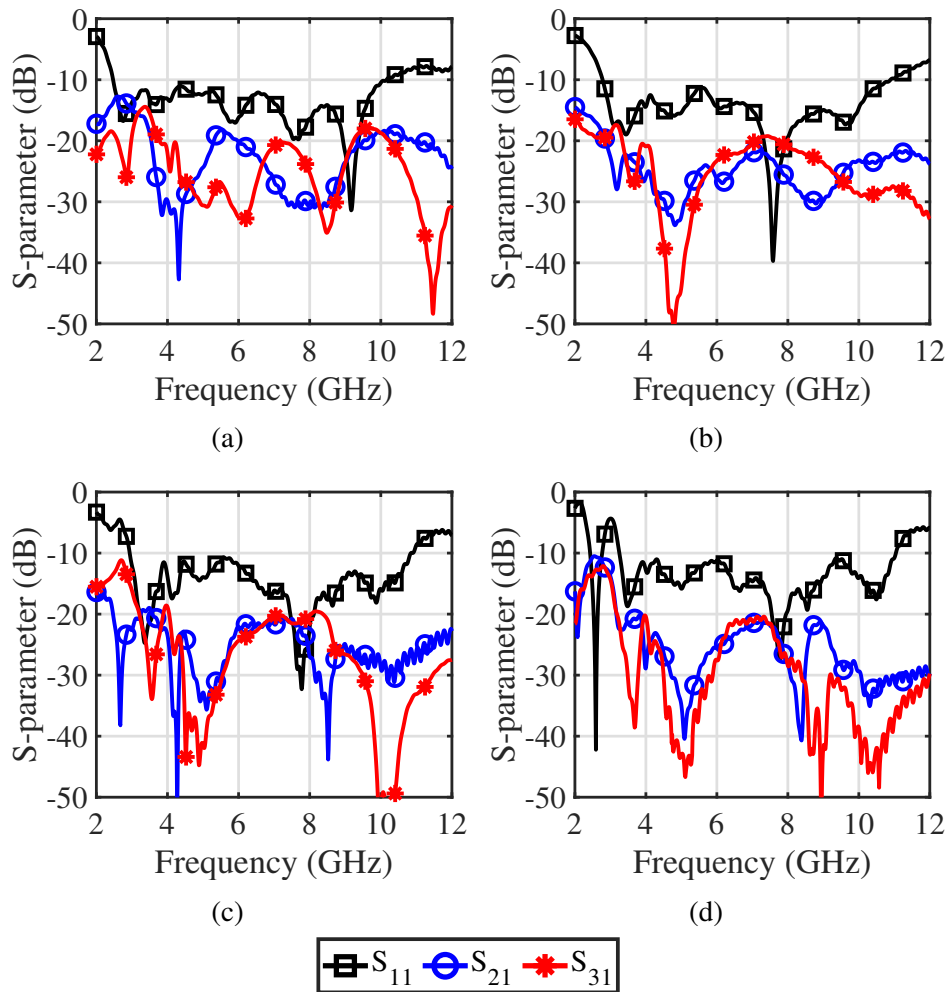


Fig. 3.17  $S$ -parameters of the antenna evolution shown in Fig. 3.16.

the mesh wire so that no extra space will be occupied and the transparency is unaffected. Secondly, the decoupling structure should be wideband so that the overall isolation can be improved within the whole operating band. Furthermore, the decoupling structure should be low profile so that it can be integrated on glass facades without affecting the aesthetic. Considering these requirements, a parasitic decoupling structure is designed and optimised on the bottom layer of the substrate along the meshed wire and the connection network. The decoupling structure is simple and effective.

Fig. 3.16(b) to (d) show the evolution of the parasitic decoupling structure based on the antenna with criss-crossing network, and the corresponding  $S$ -parameters are shown in Fig.

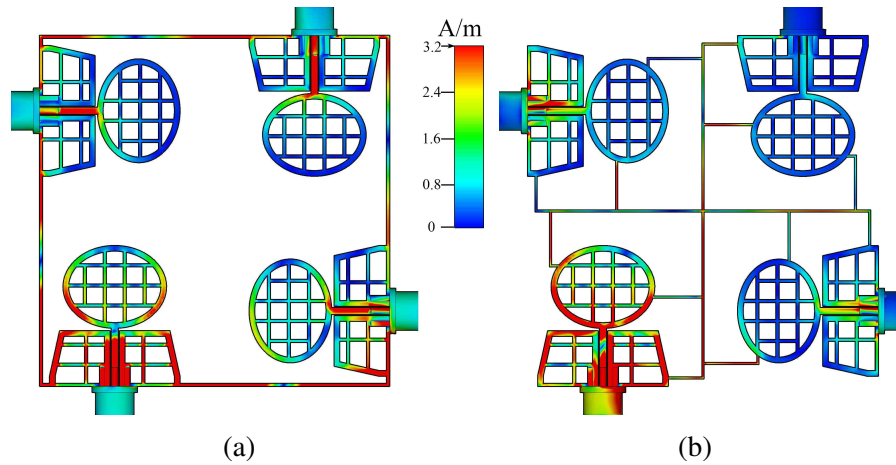


Fig. 3.18 Current distributions on the MIMO antenna when Element 1 is excited at 3.5 GHz: (a) initial structure, (b) final structure.

3.17(b) to (d). Fig. 3.16(c) and (d) also show the current distribution on the decoupling structure at 4 GHz when Element 1 is fed. By observing  $S$ -parameters of the antenna without decoupling structure in Fig. 3.17(b), the coupling between diagonal elements needs to be reduced at around 3.3 GHz and 7.4 GHz. In Fig. 3.16(c), a parasitic decoupling structure which forms a semi-encirclement for each element is attached to the back of the connection network. In Fig. 3.17(c), although  $S_{31}$  is reduced,  $S_{21}$  increased around 3.5 GHz. The final optimisation is to add a half-moon structure along the meshes as shown in Fig. 3.15(b) and its current distribution is shown in Fig. 3.16(d). Compared with Fig. 3.16(c), Fig. 3.16(d) indicates that a stronger resonance is incurred on the decoupling structure. A large amount of energy that should have coupled to other ports are concentrated and canceled on the decoupling structure. As shown in Fig. 3.17(d), both  $S_{21}$  and  $S_{31}$  are limited to below -20 dB over the whole working band.

In summary, good isolation performance of the proposed UWB MIMO TA can be attributed to three aspects. (1) Orthogonal placement. The coupling between adjacent elements is small mainly due to the fact that they are orthogonally polarized. (2) Connection structure. The ground of the four antenna elements is connected by a specially designed criss-crossing network. The hollowed-out ground and substrate between elements act as a defected ground structure [136], which can block surface waves between elements. (3)

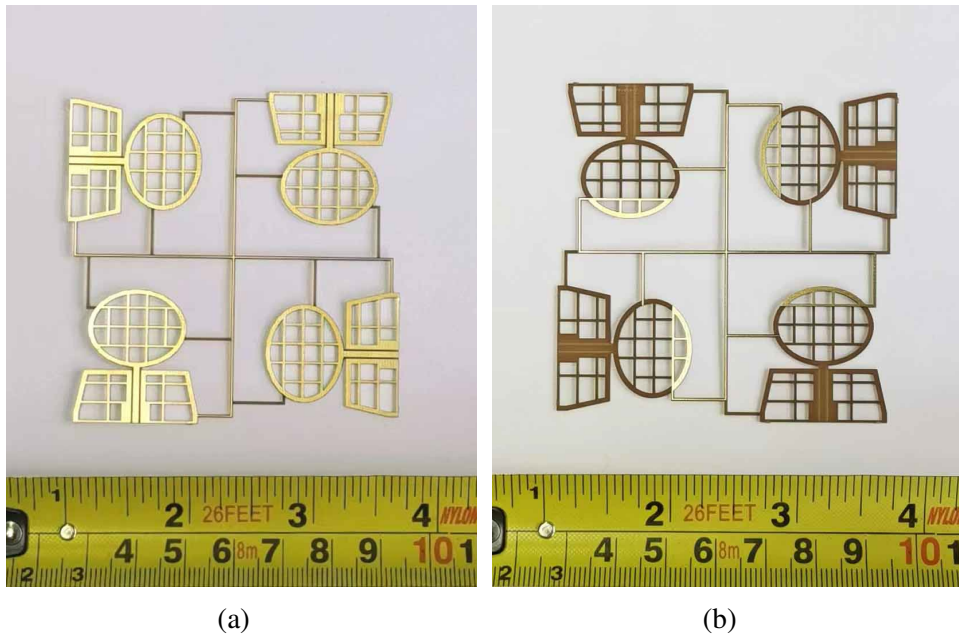


Fig. 3.19 The prototype of the proposed antenna: (a) front view, (b) rear view.

Decoupling structure. A parasitic decoupling structure is designed on the back of the connection network, which can block and cancel the inductive current and thus improve the isolation between elements. Fig. 3.18 shows the surface current on the MIMO antenna when Element 1 is excited. By comparing Fig. 3.18(a) and (b), the difference of the current distribution between the antenna without and with criss-crossing connection network and parasitic decoupling structure at 3.5 GHz can be observed. In Fig. 3.18(a), a strong induced current is generated around the feeding area of other elements. In Fig. 3.18(b), the current on other elements is significantly reduced as a strong current is blocked by the decoupling structure, which demonstrates the effectiveness of the proposed parasitic decoupling structure. This phenomenon generally applies to the entire frequency band. It should be emphasised that the proposed decoupling structure is aligned with the mesh grid completely and the transparency of the antenna is not degraded.

### 3.3.4 Results and Discussion

A prototype is fabricated shown in Fig. 3.19. The wired MM is carved on an opaque FR-4 substrate by the standard PCB technology first, and then the substrate is hollowed by

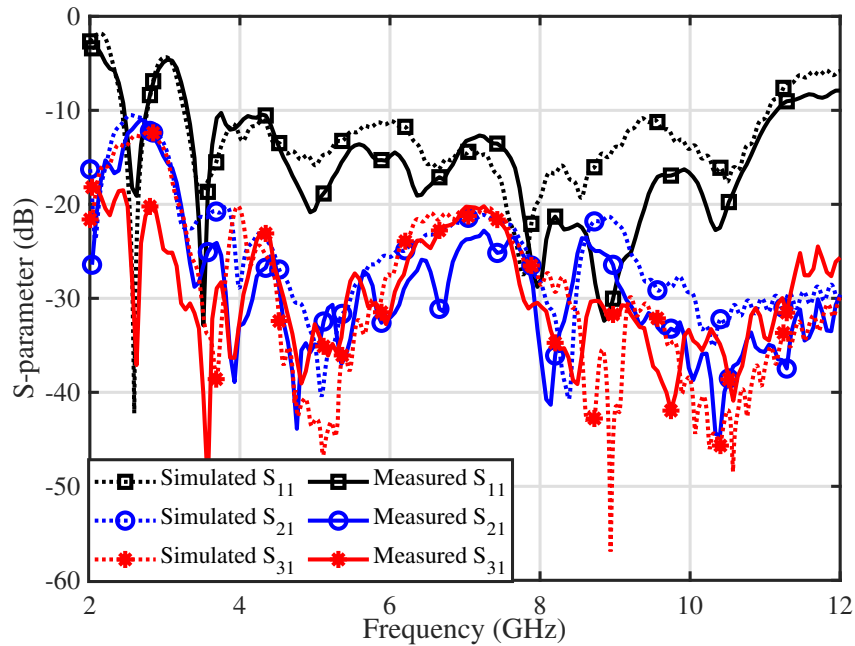


Fig. 3.20 The simulated and measured  $S$ -parameter of the proposed UWB MIMO TA.

laser cutting technology. The whole fabrication process is a conventional method for mass production of PCB circuit boards, so it is simple and low-cost. All the parameters of the fabricated antenna are set as the values in Table 3.2, and 77% transparency is obtained.

The simulated and measured  $S$ -parameters of the proposed UWB MIMO TA are shown in Fig. 3.20. The simulated band for  $S_{11}$  below -10 dB is 3.1-11 GHz while the measured bandwidth is 3.2-11.2 GHz. Both the simulated and measured  $S_{21}$  and  $S_{31}$  are lower than -20 dB over the entire operating band. The results indicate good isolations are achieved among MIMO elements. Overall, the measured results show good agreement with the simulations. The discrepancies are caused by the fabrication error and the inaccuracy of the dielectric properties of the substrate.

Fig. 3.21 shows the simulated and measured radiation patterns in  $x$ - $z$ -plane and  $y$ - $z$ -plane at 4 GHz, 7 GHz and 10 GHz. In the measurement, Element 1 is excited while other elements are terminated with  $50 \Omega$  matched loading. Due to the rotational symmetry of the MIMO antenna, only the radiation pattern of Element 1 is presented. The radiation pattern of Element 2 in  $x$ - $z$  plane is similar with that of Element 1 in  $y$ - $z$  plane, and radiation pattern of Element 2 in  $y$ - $z$  plane is similar with that of Element 1 in  $x$ - $z$  plane. From Fig. 3.21,

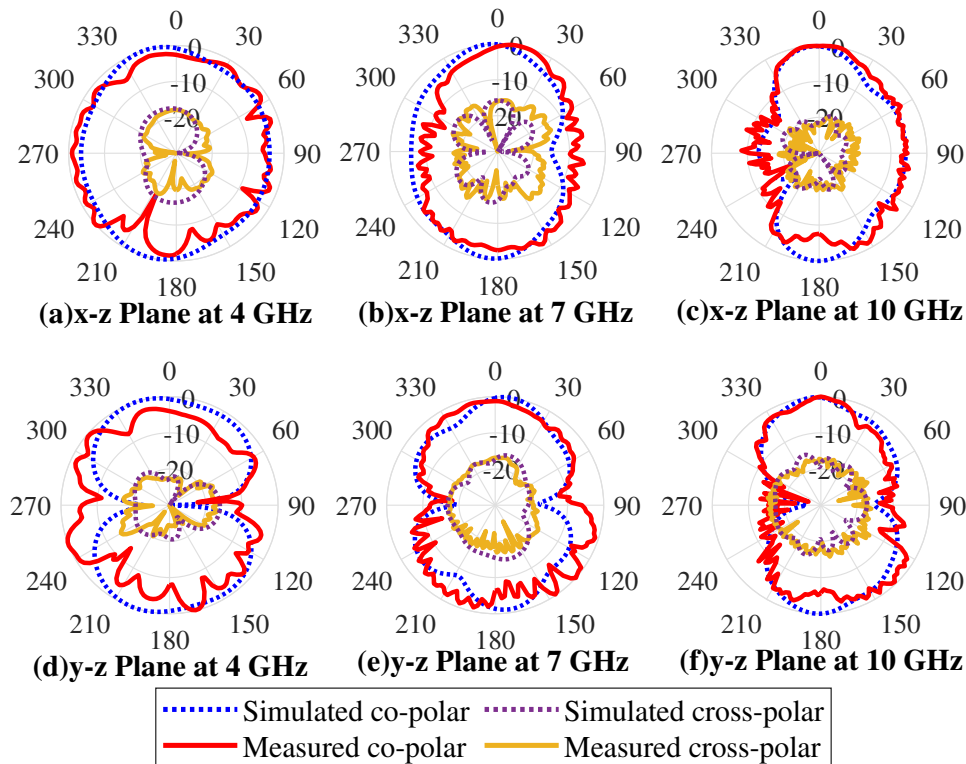


Fig. 3.21 The simulated and measured radiation patterns: (a) x-z plane at 4 GHz, (b) y-z plane at 4 GHz, (c) x-z plane at 7 GHz, (d) y-z plane at 7 GHz, (e) x-z plane at 10 GHz, (f) y-z plane at 10 GHz.

the measured results approximately agree with the simulated results. The radiation of the proposed antenna is bidirectional, and the maximum radiation is along  $z$ -axis. As mentioned before, the current distribution on the antenna is not altered much by the wired metal mesh. Therefore, the antenna elements operate in the same mode before and after hollowing, and it can be observed from Fig. 3.21 that the co-polarization component is maintained and the cross-polarization component is about 18 dB less than co-polarization in the broadside direction.

TAs can be a great way for indoor application due to their transparency. To show the feasibility of the antenna for indoor application, the proposed antenna with 77% transparency was measured while attaching to a glass window. As shown in Fig. 3.22, the antenna does not block normal sight. The bandwidth is from 3.2 GHz to 11.8 GHz. Though  $S_{31}$  exceeds -20 dB around 5 GHz, the isolation performance is excellent within the most of operating band.

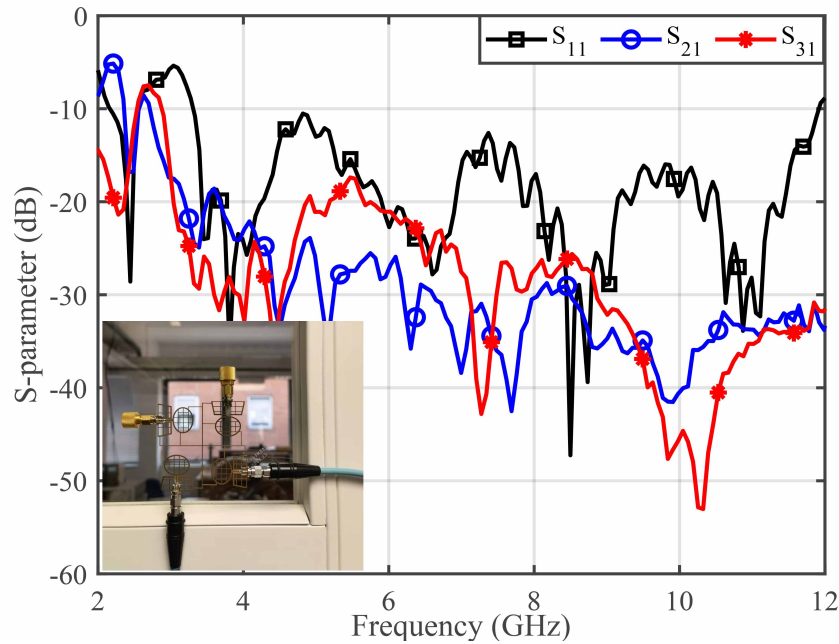


Fig. 3.22 Measured  $S$ -parameter and picture of the UWB MIMO TA attached to an indoor window.

Fig. 3.23 depicts the radiation efficiency and gain of the proposed antenna when Element 1 is excited. A comparison efficiency and gain of its solid shape is also included. The simulated radiation efficiency of TA is greater than 0.83 within the whole bandwidth. The measured gain of TA varies from 3.0 dBi to 7.3 dBi over the operating band. Though the antenna is hollowed out, the thinnest metal wire of the antenna remains 0.5 mm width which has very low resistance. Thus, the efficiency and gains are comparable to solid metal antennas and much better than other types of TA.

The mean effective gain (MEG) is used to quantify the average received signal strength of each antenna element taking into account the multipath propagation environment. It is defined as the ratio of received power ( $P_{Rec}$ ) to the sum of average vertical and horizontal incident power ( $P_V + P_H$ ) shown in (3.21). MEG can be affected by radiation power pattern, total efficiency and propagation environment [137]. The mean incident power ratio  $P_V/P_H$  represents the cross-polarization power ratio (XPR). Using XPR, MEG can be calculated by

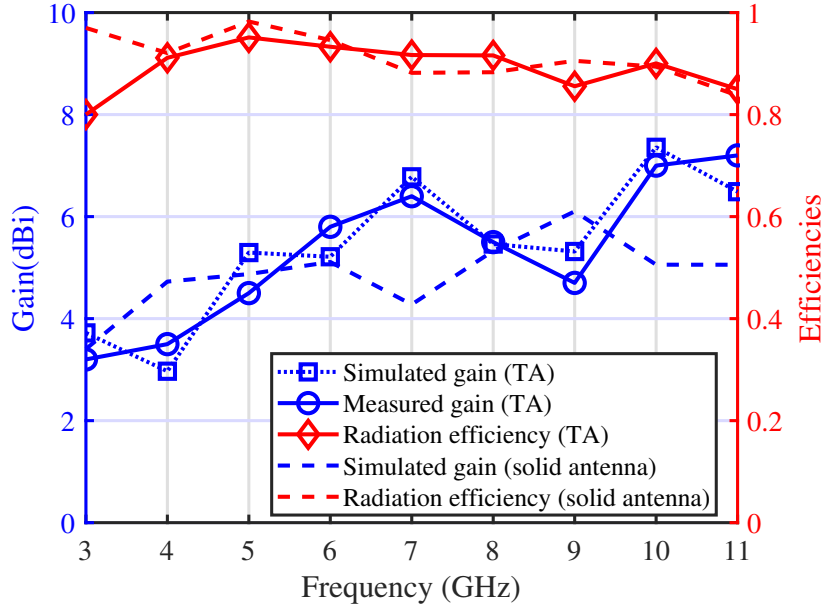


Fig. 3.23 The gain and radiation efficiency of the proposed antenna.

(3.22):

$$MEG_i = \frac{P_{Rec}}{P_V + P_H} \quad (3.21)$$

$$MEG_i = \int_0^{2\pi} \int_0^{\pi} \left[ \frac{XPR}{1 + XPR} G_{\theta}(\theta, \phi) P_{\theta}(\theta, \phi) + \frac{1}{1 + XPR} G_{\phi}(\theta, \phi) P_{\phi}(\theta, \phi) \right] \sin\theta d\theta d\phi \quad (3.22)$$

where  $G_{\theta}(\theta, \phi)$  and  $G_{\phi}(\theta, \phi)$  are the  $\theta$  and  $\phi$  components of the antenna power gain pattern, respectively, and  $P_{\theta}(\theta, \phi)$  and  $P_{\phi}(\theta, \phi)$  are the  $\theta$  and  $\phi$  components of the angular density functions of incoming waves, respectively. In Fig. 3.24(a), MEG for Element 1 is derived in the case of uniform multipath environment ( $P_{\theta}(\theta, \phi) = P_{\phi}(\theta, \phi) = \frac{1}{4}\pi$ ) and Gaussian in elevation while uniform in azimuth ( $\sigma_V = \sigma_H = 20^\circ$ ), when XPR equals 0 dB and 6 dB, respectively. The ratios of MEG for  $i$ th element to MEG for  $j$ th element are used to quantify the power imbalance between elements, which are shown in Fig. 3.24(b). The following criterion is satisfied which indicates good channel performance over the whole operating

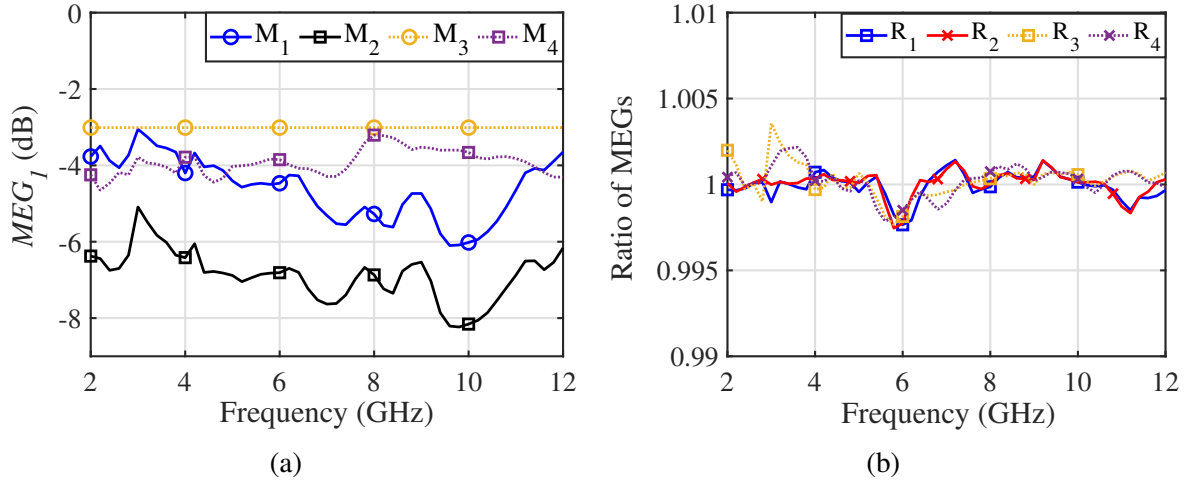


Fig. 3.24 (a) MEG of Element 1, where  $M_1$  and  $M_2$  are based on Gaussian for elevation and uniform for azimuth with 0 and 6 dB XPR,  $M_3$  and  $M_4$  are based on isotropic environment with 0 and 6 dB XPR, (b) Ratio between MEGs at  $XPR = 6$  dB, where  $R_1$  and  $R_2$  are obtained by  $|MEG_1/MEG_2|$  and  $|MEG_1/MEG_3|$  using Gaussian for elevation and uniform for azimuth, while  $R_3$  and  $R_4$  are obtained by  $|MEG_1/MEG_2|$  and  $|MEG_1/MEG_3|$  based on isotropic environment.

band is obtained.

$$|MEG_i/MEG_j| \approx 1 \quad (3.23)$$

The channel isolation and diversity performance can be evaluated by the ECC and diversity gain (DG). ECC for this antenna is obtained from the radiation field using the following equation [138]:

$$\rho_{ij} = \frac{\iint_{4\pi} \mathbf{E}_i(\theta, \phi) \cdot \mathbf{E}_j^*(\theta, \phi) d\Omega}{\sqrt{\iint_{4\pi} \mathbf{E}_i(\theta, \phi) \mathbf{E}_i^*(\theta, \phi) d\Omega \iint_{4\pi} \mathbf{E}_j(\theta, \phi) \mathbf{E}_j^*(\theta, \phi) d\Omega}} \quad (3.24)$$

where  $\mathbf{E}_i(\theta, \phi)$  and  $\mathbf{E}_j(\theta, \phi)$  are the three dimension radiation field for port  $i$  and  $j$ . To guarantee good isolation, the accepted limit is that ECC should be lower than 0.5. On the other hand, DG is defined as the following equation:

$$DG_{ij} = 10\sqrt{1 - \rho_{ij}^2} \quad (3.25)$$

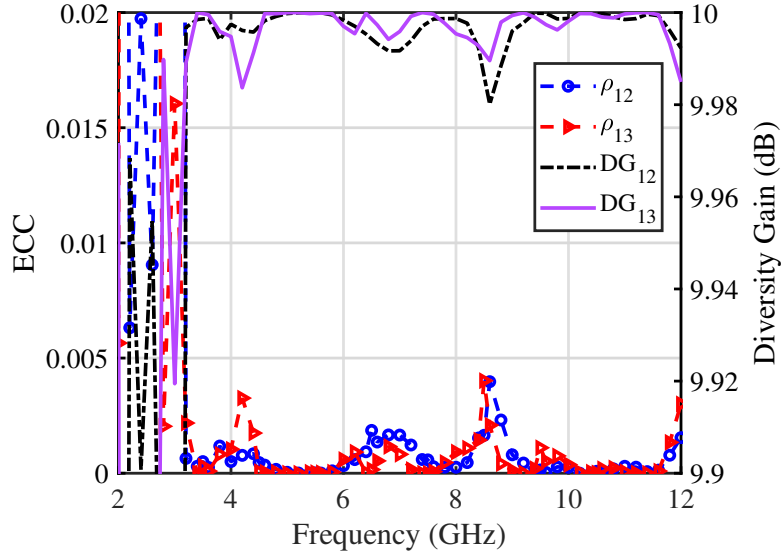


Fig. 3.25 ECC and DG calculated by farfields, where  $\rho_{12}$  and  $DG_{12}$  represent ECC and DG between element 1 and 2,  $\rho_{13}$  and  $DG_{13}$  represents ECC and DG between element 1 and 3.

Fig. 3.25 shows the simulated ECC and DG. The ECC values are less than 0.004 and DG is more than 9.98 dB within the entire operating band, which indicates the proposed MIMO antenna has great diversity performance.

The channel capacity in a  $N \times N$  MIMO system can be calculated by (3.26),

$$C = \log_2 \det \left( \mathbf{I} + \frac{\rho}{N} \mathbf{H} \mathbf{H}^H \right) \quad (3.26)$$

where  $\mathbf{I}$  denotes an identity matrix,  $\rho$  is the average SNR at each receiving antenna and  $N$  denotes the number of transmitting antennas. Assume the the reference propagation environment is independent Rayleigh fading channel  $\mathbf{H}_w$ , the channel state information is unknown, the transmit power strategy is equal power allocation and the receiver SNR is 20 dB, the elements of  $\mathbf{H}_w$  are zero-mean circularly symmetric complex Gaussian random variables. Set the proposed antenna as receiving antenna, and transmitting antenna is ideal, the MIMO channel  $\mathbf{H}$  including antenna effect can be expressed as (3.27) [139],

$$\mathbf{H} = \mathbf{R}^{1/2} \mathbf{H}_w \quad (3.27)$$

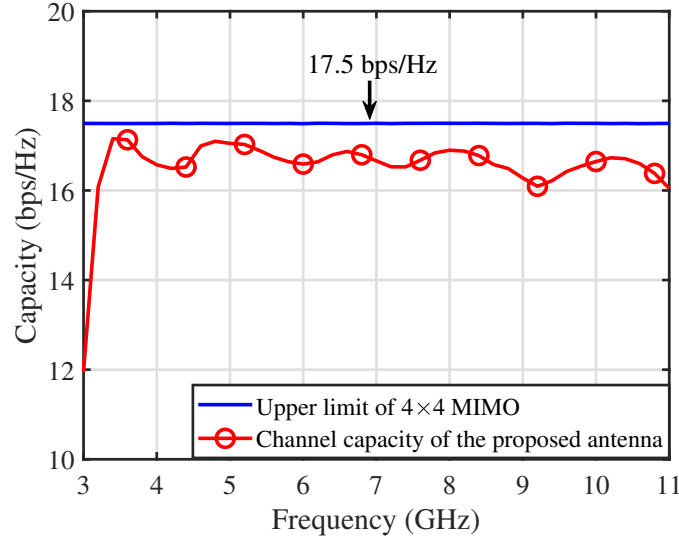


Fig. 3.26 Channel capacity of the proposed MIMO TA.

where  $\mathbf{R}$  is the matrix of receive correlation coefficient of the proposed MIMO antenna, and can be calculated by  $\mathbf{R} = \mathbf{\Lambda}^{1/2} \bar{\mathbf{R}} \mathbf{\Lambda}^{1/2}$ . Here the elements of  $\bar{\mathbf{R}}$  are correlation coefficients of the three-dimensional radiation fields, and  $\mathbf{\Lambda}$  is a diagonal matrix whose elements are total efficiencies of each element. For large SNR, the instantaneous capacity of (3.28) is given by (3.26) and (3.29):

$$C \approx C_0 + \log_2 \det(\mathbf{R}) \quad (3.28)$$

$$C_0 = \log_2 \det \left( \mathbf{I} + \frac{\rho}{N} \mathbf{H}_w \mathbf{H}_w^H \right) \quad (3.29)$$

where  $C_0$  is the upper limit capacity of the  $N \times N$  MIMO system of the ideal Rayleigh channel with ideal antennas. Fig. 3.26 shows the channel capacity of the  $4 \times 4$  MIMO system. Thanks to the low ECC and high efficiency of the proposed MIMO TA, the channel capacity achieves more than 16 bps/Hz within the whole operating band, and the peak capacity is 17.2 bps/Hz which is very close to the upper limit of 17.5 bps/Hz.

To evaluate the time domain response, two of the proposed antennas are employed as Tx and Rx antennas which are separated by 0.5 m. The transfer function between Tx and Rx is measured, and the group delay shown in Fig. 3.27(a) is derived from the phase of the transfer function. The variation of group delay is small within the whole operating band which

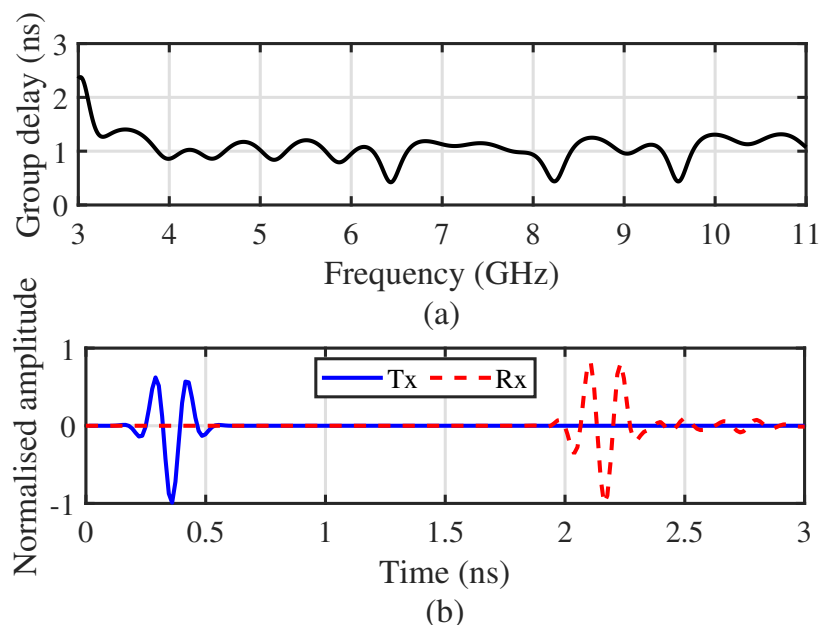


Fig. 3.27 (a) Normalised transmitted and received signal pulses at 0.5 m, (b) group delay.

indicates the proposed antenna has a good phase-frequency characteristic. The transmitted Gaussian pulse and received pulse are compared in Fig. 3.27(b). Compared to the transmitted pulse, the received pulse has a little ringing, the fidelity factor between the transmitted and received pulse is 0.83, which indicates the signal distortion is very limited and the proposed antenna has excellent time domain response.

Table 3.3 compares the performances of the proposed transparent UWB MIMO antenna with other previously reported similar designs. So far, three materials have been employed to design transparent MIMO antenna: TCFs, micro MM and wired MM. The most common material is TCF such as ITO and AgHT in [40, 41, 69, 71]. From Table 3.3, these designs obtain wide bandwidths and high isolations, however, the radiation efficiencies and gains are low. Micro MM [53, 54] has higher conductivity than TCF, especially in [53] when Ni is embedded, the radiation efficiency of the antenna is greatly improved while high transparency is also obtained. However, the fabrication process of micro MM is complex and costly. This paper presented UWB MIMO TA based on wired MM for the first time. Although the transparency of the wired MM is inhomogeneous, the overall transparency of the wired MM is comparable to that of TCFs. From Table 3.3, the proposed antenna achieves much higher

Table 3.3 COMPARISON OF TRANSPARENT MIMO ANTENNAS

Ref.	[40]	[41]	[69]	[71]	[53]	[54]	This work
Elements	4	2	2	4	4	2	4
Size (mm <sup>2</sup> )	45×66	29×50	50×120	150×70	60×60	40×40	70×70
Material	AgHT-4	ITO	AgHT-8	ITO	Micro MM	Micro MM	Wired MM
Transparency	70%	72%	-	84%	93%	75%	77%
Band (GHz)	2.2-6	2.4-11	3.1-10.6	4.9 & 26	4.4-5	2.45 & 5.5	3.2-11.2
Isolation (dB)	15	20	20	30	20	15	20
Gains (dBi)	0.5	-2 to 2	-6 to -2	2	3.8	0.74 & 2.3	3 to 7.3
Efficiency	41%	60%	20%	-	85%	40%	83%-95%

radiation efficiency than TCF antennas in [40, 41, 69, 71] and greater bandwidth than micro MM antennas in [53] and [54]. Furthermore, the fabrication process of the proposed antenna is simple with a low cost.

### 3.3.5 Conclusion

A 4-element TA with 77% transparency and 83% radiation efficiency for UWB MIMO application has been proposed in this section. A wideband parasitic decoupling structure reduces the mutual coupling below -20 dB. MIMO diversity performance is guaranteed in terms of the ratios of MEG ( $1 \pm 0.003$ ), ECC (less than 0.004) and DG (more than 9.98 dB). The MIMO capacity in Rayleigh channel achieves 17.2 bps/Hz. The fidelity factor in UWB transmission reaches 0.83. Since the antenna integrated on the window can provide UWB MIMO service with little visual influence, it is a very promising device to be applied in the indoor wireless infrastructure, as wireless communication will become one of the most fundamental utilities of a building.



# Chapter 4

## TCF Antennas

### Overview

In this chapter, two TAs using ITO are proposed. Section 4.1 achieves UWB MIMO, which lays the foundation, but the efficiency and gain are very low. Section 4.2 uses the FPC to address them and achieves enhanced performance using the same TCF. The following paragraphs briefly introduce the designs.

In **Section 4.1**, an optical TA using ITO for UWB MIMO applications is proposed. The ultrathin ITO film is coated on a  $67 \times 67 \text{ mm}^2$  glass substrate and over 85% transparency is achieved. The antenna consists of four CPW-fed antenna elements with rotationally symmetric placement. The adjacent elements are placed orthogonally to produce dual polarisation and reduce coupling. The MIMO antenna operates from 1.5 to 11 GHz which covers the UWB applications. The coupling between the elements is less than -23 dB. MEG, ECC and DG achieve excellent values which guarantee good MIMO performance. The prototype is verified and the measured results are analysed.

**Section 4.2** proposes the first fully transparent Fabry-Perot cavity (FPC) antenna using indium tin oxide (ITO) film and glass substrates to improve the efficiency and gain of ITO antenna. The proposed TA is composed of a high efficiency transparent monopole (TM) feed source and two transparent partially reflecting surfaces (PRSs). The structure of the TM and the PRSs are optimised to get a good compromise between transparency and radiation efficiency. Multi-resonance cells on the PRSs are designed to improve the bandwidth. The

proposed transparent FPC antenna obtains an overall optical transparency of 84% and a peak efficiency of 70.4%. A peak gain of 11.7 dBi is achieved with an aperture size of  $2.2\lambda_0 \times 2.2\lambda_0$ , and the 3 dB gain bandwidth spans from 4.9 GHz to 6.3 GHz. Furthermore, the transparent cavity structure makes the proposed antenna can be integrated with indoor double glazing seamlessly.

## 4.1 UWB MIMO Optical Transparent Antenna Based on ITO film

### 4.1.1 Introduction

In this section, an ITO based TA for UWB and MIMO applications is proposed. The proposed antenna comprises 4 transparent CPW-fed elements on a glass substrate. The smooth elliptical patches realise a resonant band of 1.5 to 11 GHz. The antenna is in a rotationally symmetric shape and has dual polarised radiation. Meanwhile, the coupling effect between the elements is constrained to a very low level dual to its orthogonal placement and common ground design.

### 4.1.2 Antenna Design

The geometry of the antenna is shown in Fig. 4.1(a). ITO film with  $4 \Omega/\text{sq}$  and  $0.38 \mu\text{m}$  thickness is used as the conductive parts and the glass piece with a thickness of 1.1 mm and dielectric constant of 6.15 is used as the substrate. The proposed antenna is designed and simulated by CST Microwave Studio 2021. By adjusting the parameters of the antenna in the simulation, we obtained the optimal antenna size of  $L = 67 \text{ mm}^2$  and an element occupies the area of  $30 \times 33 \text{ mm}^2$ .

The antenna consists of 4 UWB CPW-fed elements. Each element is fed by a  $50 \Omega$  CPW line with  $H_g = 13 \text{ mm}$  length and  $W_f = 2 \text{ mm}$  width. The width of the slot between the feeding line and ground is  $G_2 = 0.3 \text{ mm}$ . The patches with ellipse shapes are beneficial to bandwidth enhancement since the progressively increasing width of the patch allows its

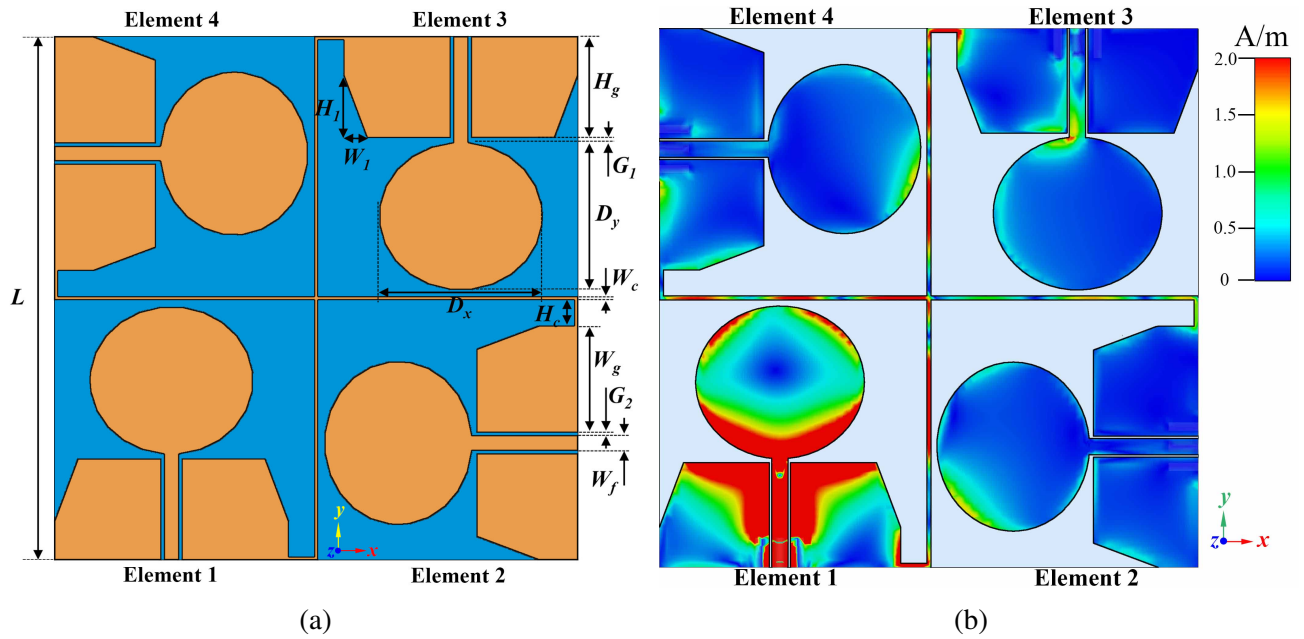


Fig. 4.1 (a) The front view of the antenna, orange represents the ITO film and blue represents the glass substrate, (b) the surface current distribution of the proposed TA, when exciting Element 1 at 7 GHz.

impedance and radiated pattern to remain relatively stable over a wide bandwidth. The optimal major axis  $Dx = 21$  mm, minor axis  $Dy = 19$  mm, the gap between patch and ground is  $G_1 = 0.2$  mm and the ground width  $W_g = 13.7$  mm. The triangle chamfer edges with sides  $H_1 = 8$  mm and  $W_1 = 3$  mm of the ground planes have auxiliary effects on UWB resonance. The chamfer edges also increase the shortest distance between the ground plane and the patch of adjacent antenna which reduces the mutual coupling.

The proposed antenna is rotationally symmetrical in shape, which can generate dual polarisation. The ground planes are connected by an ITO wire intercrossing at the centre of the antenna array instead of directly connecting the ground planes of adjacent elements. The width of the ITO wire is  $W_c = 0.5$  mm and the length of ground connection  $H_c = 3.3$  mm. The intercrossing can not only share common ground but also benefit the isolation between the elements by blocking the coupling energy.

Fig. 4.1(b) shows the current distribution when Element 1 is fed at 7 GHz. Though the current distribution are different in different frequency, current distributed at 7 GHz is

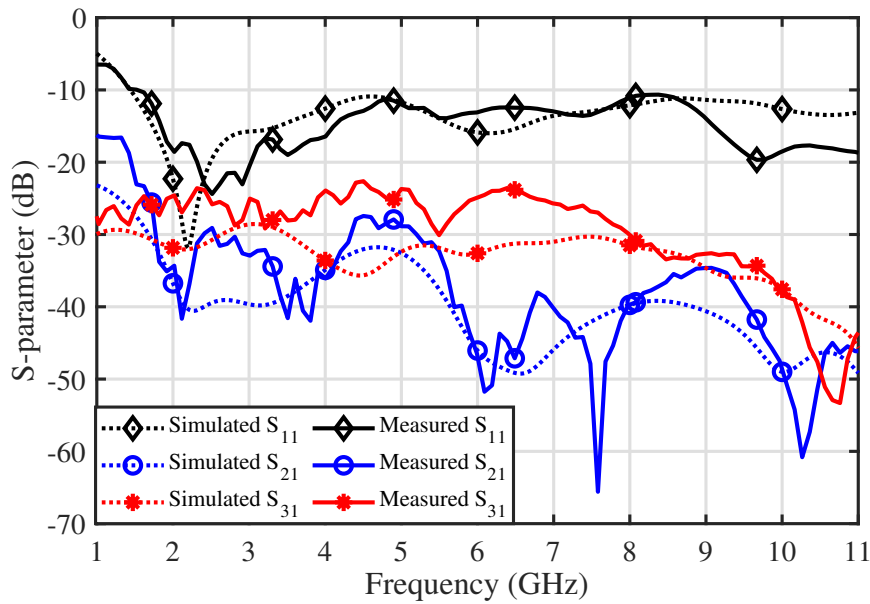


Fig. 4.2 The simulated and measured S-parameter of the proposed  $2 \times 2$  MIMO TA.

representative over the band. The strong current always concentrated on the edge of the patch and feeding line and the coupling current is always stronger at diagonal element than that at adjacent element. Element 1 is vertically polarised while Element 2 is horizontally polarised. The main current on Element 1 is distributed along the y-axis, thus, it leads to a strong y-axis induced current on the patches of Element 2. Since Element 2 is polarised along x-axis and the crossing common ground structure increases the separation between elements, the coupling between Element 1 and 2 is reduced. Compared with Element 2, the induced current direction of Element 3 is the same as its polarisation direction, and the coupling of Element 1 and 3 can be strong.

### 4.1.3 Simulation and Measurement Results

Fig. 4.2 shows the simulated and measured S-parameters of the antenna. Since the antenna array is rotationally symmetric,  $S_{41}$  is the same as  $S_{21}$ , so only  $S_{11}$ ,  $S_{21}$  and  $S_{31}$  are shown. Both simulated and measured  $S_{11}$  are less than -10 dB from 1.5 GHz to more than 11 GHz. The simulated and the measured coupling effect between adjacent elements ( $S_{21}$ ) are always

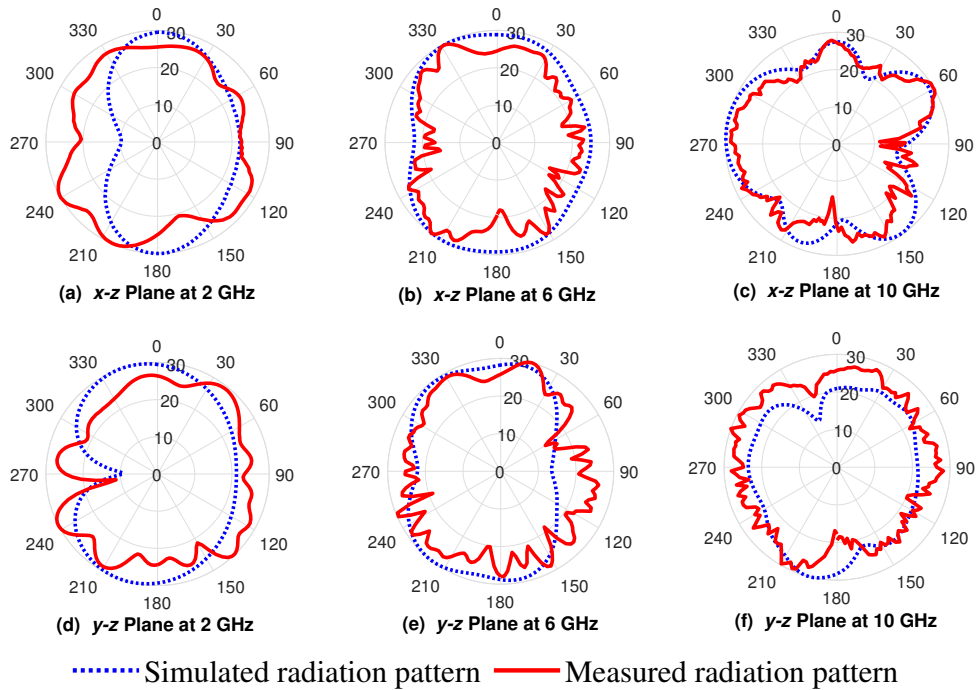


Fig. 4.3 The simulated and measured radiation patterns

kept at less than -25 dB. The simulated  $S_{31}$  of diagonal elements are less than -27 dB and measured  $S_{31}$  are less than -23 dB. Orthogonal polarisation and special common ground design largely reduce the mutual coupling. Since the radiation patterns above 11 GHz have multiple side lobes and largely deviate from the  $z$ -axis direction, this antenna is most suitable for working below 11 GHz. The main purpose of the antenna is to provide service over UWB which spans from 3.1 to 10.6 GHz.

Fig. 4.3 shows the radiation patterns of the proposed antenna when Element 1 is excited. Due to the rotational symmetry of the MIMO antenna, only the radiation pattern of Element 1 is presented. In Fig. 4.3(a), (b), (d) and (e), the main lobes of the antenna point toward  $z$ -axis. As shown in Fig. 4.3(c) and (f), the strong  $z$ -direction radiation is presented, but a strong sidelobe appears. In practical applications in indoor environments, a slight deviation of the main lobe and the appearance of side lobes can be tolerated. Because the abundant scatterers in the room facilitate multipath signal propagation to cover the entire space.

The MIMO performance can be evaluated by MEG [137], ECC and DG. MEG can be derived by Equation (3.22). The cross-polarization power ratio (XPR) is defined by the propagation environment. MEGs of the elements are calculated based on Gaussian in

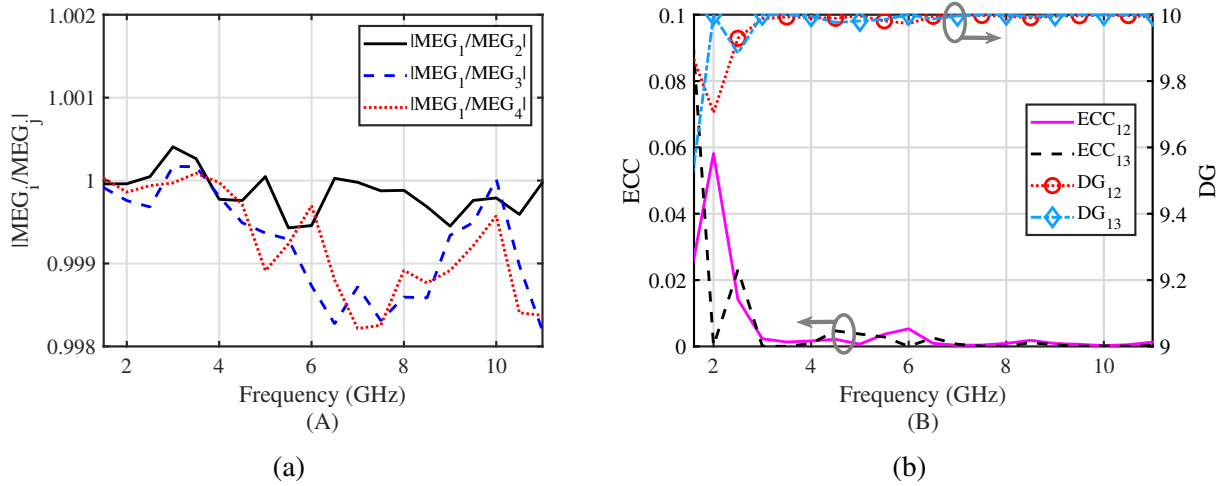


Fig. 4.4 (a) Ratios of MEG between element  $i$  and  $j$ ; (b) ECC and DG.

elevation while uniform in azimuth with 0 dB XPR. The ratios of MEG of the elements can evaluate the power imbalance in a multipath propagation environment. A ratio approximates to 1 can guarantee good channel performance. Fig. 4.4(a) shows the MEG ratios are limited within  $1 \pm 0.002$ . To evaluate channel performance, ECC is calculated using radiation patterns as shown in Equation (3.24). The limitation of acceptable ECC is less than 0.5. In Fig. 4.4(b), ECC is under 0.1. DG is to evaluate diversity performance which can be derived from Equation (3.25). As shown in Fig. 4.4(b), DG is larger than 9.5 dB over the operating band.

The prototype in Fig. 4.5(a) is fabricated by using magnetron sputtering and laser engraving. The visible light transparency of the ITO antenna is 85%. As a reference, the transparency of a pure glass substrate with the same thickness is 93%. Fig. 4.5(b) shows the effect when the antenna is attached to an indoor window. It does not cause any obstruction to the visual effects. The ITO films are almost invisible.

Table 4.1 compares the other transparent MIMO antenna using TCF materials. Compared to [40, 41, 69], the proposed antenna has advantages in transparency, bandwidth and isolation performance. Limited by ITO material properties, the peak gain of the proposed antenna is 0.3 dBi. It is comparable to the TAs without gain enhancement. Compared with the antenna proposed in Chapter 3.3, this TA has very similar dimension and structure, resulting in comparable bandwidth performance. However, a significant alteration in material choice, utilising ITO, has led to a notable reduction in the antenna's gain. Despite lacking a

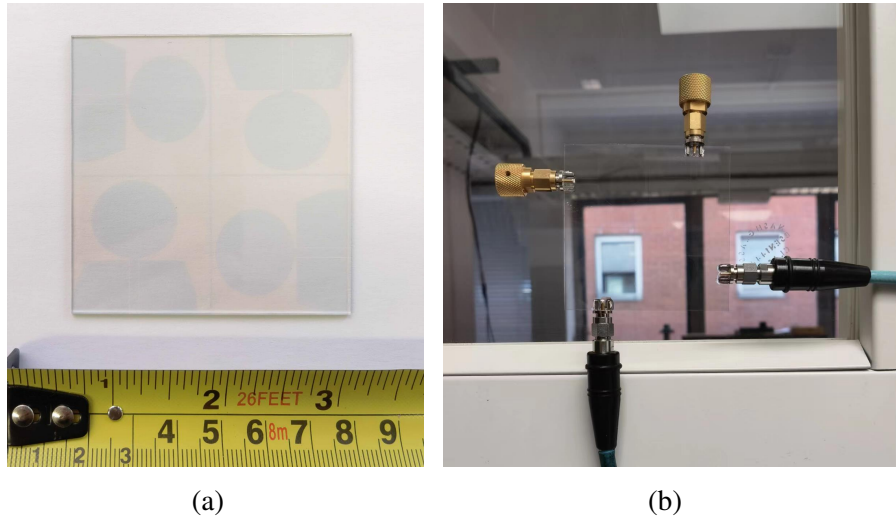


Fig. 4.5 Photograph of proposed antenna: (a) antenna prototype and (b) the visual effect of the TA attaching to the indoor window.

Table 4.1 COMPARISON OF TCF MIMO ANTENNAS

Ref.	[40]	[41]	[69]	TA in Chapter 3.3	This work
Elements	4	2	2	4	4
Material	AgHT-4	ITO	AgHT-8	MM	ITO
Transparency	70%	72%	-	77%	85%
Band (GHz)	2.2-6	2.4-11	3.1-10.6	3.2-11.2	1.6-11
Isolation (dB)	15	20	20	20	23
Peak Gain (dBi)	0.5	2	-2	7.3	0.3

decoupling network akin to the MM TA, the ITO TA capitalizes on its lower conductivity. This attribute translates to a heightened insensitivity to EM wave reflection, consequently enhancing isolation capabilities.

#### 4.1.4 Conclusions

A TA using ITO material for the UWB MIMO application is presented. The visible light transparency of the antenna achieves 85%. The antenna operates over a frequency band from 1.5 to 11 GHz.  $2 \times 2$  CPW-fed elements are placed rotational symmetrically, which can generate dual polarisation and reduce mutual coupling. The mutual coupling among

elements is less than -23 dB. The MIMO performance is guaranteed by excellent MEG ratios, ECC and DG values. The antenna can be easily integrated into many indoor objects with very little virtual effect and is capable of serving the UWB MIMO application. The proposed TA will potentially play an important role in future smart buildings.

## **4.2 High Efficiency and High Gain ITO TA Based on Fabry-Perot Cavity**

### **4.2.1 Introduction**

5G communication will greatly accelerate the development of smart cities and smart homes [25, 140]. To enhance coverage and spectral efficiency of 5G communications in complex application scenarios, especially in buildings, densely deployed base stations and antennas are required. Due to spatial and aesthetic constraints in buildings, increasing the number of conventional antennas is not a preferred solution [141, 142]. Integrating transparent antenna (TA) into the inherent facilities of the building, such as glass windows and facades, can get the base station rid of the spatial and aesthetic limitations [143].

Most TA researches revolve around metal mesh (MM) and transparent conductive films (TCFs) [26]. Although MM antennas have higher conductivity, they are inferior in transparent performance. TAs with higher transparency using TCFs are preferred while integrating with glass. The commonly used TCFs include indium tin oxide (ITO), silver-coated polyester film (AgHT) and fluorine-doped tin oxide (FTO) [144]. In recent years, TCFs have been applied to many scenarios, including automotive windshields [41], handset screen [71] and solar module [68]. TCFs are made extremely thin to achieve higher transparency than meshed metal antennas. However, ultrathin films have high sheet resistance which leads to a large Ohmic loss. The efficiencies and gains of most TCF TAs are much less than conventional metal antennas. To address this issue, various solutions have been proposed. [55, 56, 53] constructed antenna arrays with MM, in which constrained feeding was used. However, the constrained feeding is not suitable for TCFs since TCFs are highly lossy and most of the

power can be dissipated in the complex feeding network. Copper and silver doped TCF materials were used to improve the efficiency of TCF TAs in [44] and [45], respectively. Although metal doping can improve the conductivity of TCF, the optical transmittance will inevitably be affected. In [95] and [96], transparent reflectarray and transmitarray were proposed to improve the gain of TCFs TAs, however, the opaque horn feed makes these antennas bulky and less transparent.

In modern buildings, double glazing is widely used for windows, doors and partitions. The double glazing forms a cavity structure which provides a design space for indoor antennas. Fabry-Perot cavity (FPC) composed of partially reflecting surfaces (PRSs) can enhance the performance of the sandwiched source antennas. In [145], FPC antennas achieved high gain by using frequency-selective surface (FSS) based PRS. Furthermore, profile [146], bandwidth [147] and radar cross section (RCS) [148] can also be optimised by FPC. Developing TA based on FPC structure is potential to improve the radiation performance of TA. In [44], a transparent FPC antenna combined ITO PRSs with a metal feeding network was designed for solar panels. The efficiency and gain of the TA were largely enhanced, however, its opaque metal feeding layer made the antenna not fully transparent.

In this section, a TA based on the FPC structure is proposed. The antenna is composed of a monopole feed source and two PRSs, which are made of ITO films and commercial glass. So the antenna is fully transparent and achieves an overall transparency of 84%. Due to the space feeding strategy and the specially designed FPC structure, the antenna achieves a peak radiation efficiency of 70.4% and a peak gain of 11.7 dBi, and the 3 dB gain bandwidth is from 4.9 to 6.3 GHz (25%). Furthermore, the proposed antenna is based on double glazing structure, which can be integrated with indoor glass facilities seamlessly.

### 4.2.2 Transparent FPC Antenna Design

The geometries and principles of the transparent FPC antenna are explained as follows. The schematic of the proposed FPC antenna is presented in Fig. 4.6. In the conventional FPC antennas, the FPC is formed by a PRS with a large reflection coefficient on the top and a metal ground plane on the bottom. When the FPC is excited by a feed source, the electromagnetic

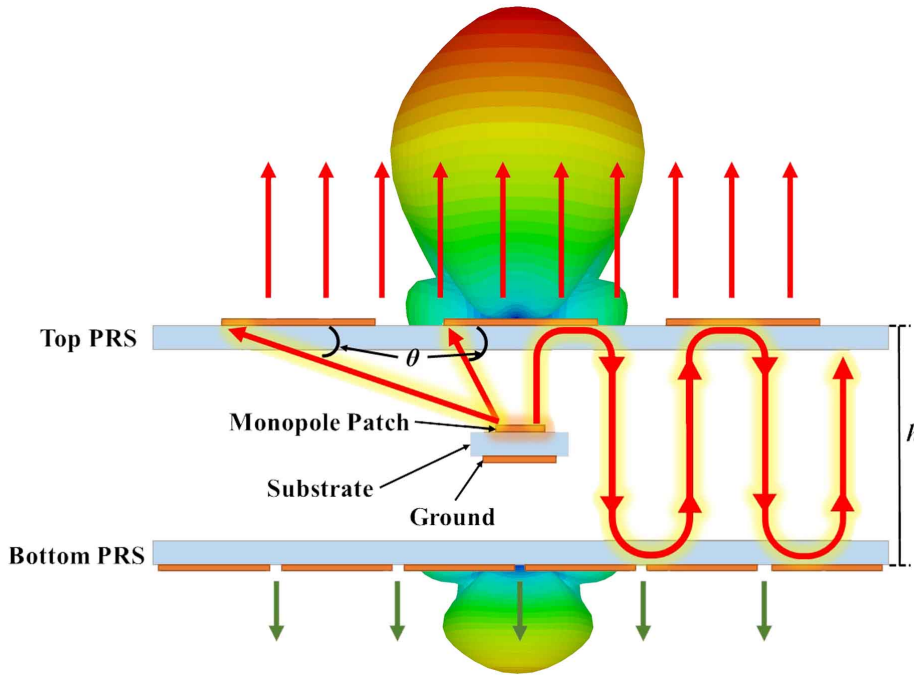


Fig. 4.6 Schematic diagram of the proposed FPC antenna.

(EM) wave from the source will undergo multiple reflections in the cavity and transmissions through the PRS. If the following resonant condition [149] is satisfied, the transmitted wave can be superposed in phase, so that the directivity of the antenna can be enhanced.

$$\frac{-4\pi h}{\lambda} + \varphi_1 + \varphi_2 = 2N\pi, N = 0, \pm 1, \pm 2 \dots \quad (4.1)$$

where  $h$  is the height of FPC,  $\varphi_1$  and  $\varphi_2$  are reflective phases of the PRS and ground plane.

The proposed transparent FPC antenna is constructed by ITO film on glass. To ensure high transparency and efficiency of the antenna, the feed source and PRSs are specially designed. As shown in Fig. 4.6, the feed source is a transparent monopole (TM) antenna with a small ground plane, which is suspended within the cavity to excite it by space feeding strategy. Space feeding eliminates the complex feeding network, which reduces the feeding line loss greatly. Different from conventional FPC antenna, in the proposed FPC, the ground plane on the bottom is replaced by a transparent PRS with high reflectivity to increase the transparency, while the top layer of the proposed FPC is another transparent PRS with low reflectivity to generate a main beam on the top. PRSs are meta structures consisting

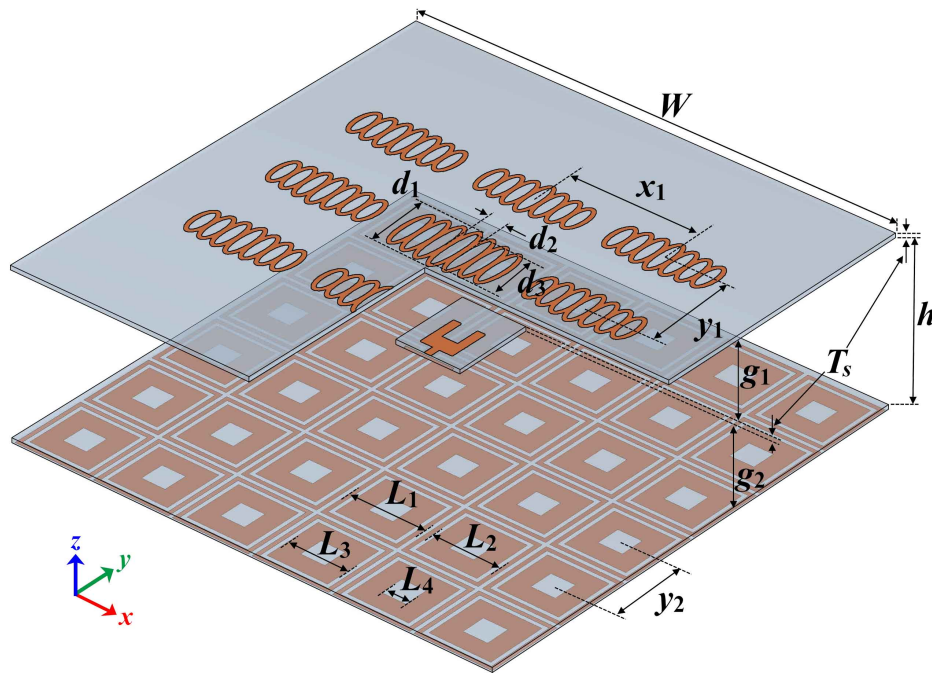


Fig. 4.7 Geometry of the transparent FPC antenna.

of periodic arrays of unit cells. To improve the bandwidth, the unit cells on both PRSs are designed in a multi-resonance structure. Although the two PRSs structure may lead to higher backlobe levels compared to the conventional FPC antenna, the proposed structure reduces the reflection loss caused by the lossy ITO material and thus high efficiency and gain enhancements for the ITO transparent antenna are obtained.

The geometry of the transparent FPC antenna is shown in Fig. 4.7 and the dimension values are shown in Table 4.2. The conductive parts shown in dark orange are ITO films with a sheet resistance of  $4 \Omega/\text{sq}$ , and a thickness of  $0.38 \mu\text{m}$ . The substrates shown in purple are made of glass pieces with a relative dielectric constant of 6.15, and a thickness of 1.1 mm. The antenna model is built and simulated by CST Studio 2022.

### High Efficiency Feeding

For ITO antennas, the feeding line is a main source of energy loss because the current is extremely strong on the feeding line. Especially the efficiency of conventional ITO antenna arrays is very low since most energy dissipates in the constrained feeding network. In the

Table 4.2 DIMENSIONS OF THE PROPOSED FPC TA

Parameter	$T_s$	$h$	$W$	$g_1$	$g_2$	$x_1$	$y_1$	$y_2$	$d_1$	$d_2$	$d_3$	$d_4$	$L_1$
Value(mm)	1.1	30	120	15	13.9	32	24	20	16	3.6	14	2.5	19
Parameter	$L_2$	$L_3$	$L_4$	$W_s$	$W_c$	$W_t$	$W_g$	$W_f$	$H_s$	$H_f$	$H_p$	$H_g$	
Value(mm)	17	15	6	12	4	2	5.2	1.6	20	2.6	10	0.5	

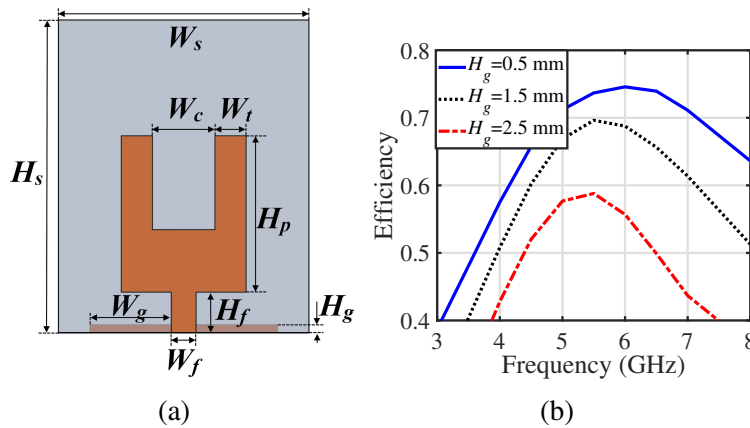


Fig. 4.8 (a) Geometry of the TM feed source, the dimensions are shown in Table 4.2, (b) the efficiencies of the TM with different  $H_g$ .

proposed FPC antenna, the space feeding is employed to excite the arrays on PRSs, which reduces the feeding loss and improves the efficiency greatly. To obtain a transparent FPC antenna with high performance, some requirements are put forward on the feed source design. First, the efficiency of the feed antenna should be high since it will determine the overall efficiency of FPC. Furthermore, the ITO footprint on the feed antenna should be small to increase transparency and reduce the influence on the EM wave propagation within the cavity.

To address this, a high efficiency TM is designed as the feed source. The geometry of the TM is shown in Fig. 4.8(a). A tuning-fork-shaped patch evolved from rectangular patch is used as radiator to maximise transparency and minimise the blockage effect on the EM wave in the cavity. Current is mainly distributed along the vertical edges of the patch and the resonant frequency of the antenna can be tuned by the height of the fork  $H_p$ . Based on this shape, the height of the ground plane  $H_g$  and feeding line  $H_f$  are optimised. A short feeding line is designed to reduce feeding loss. In Fig. 4.8(b), the efficiencies of the TM with

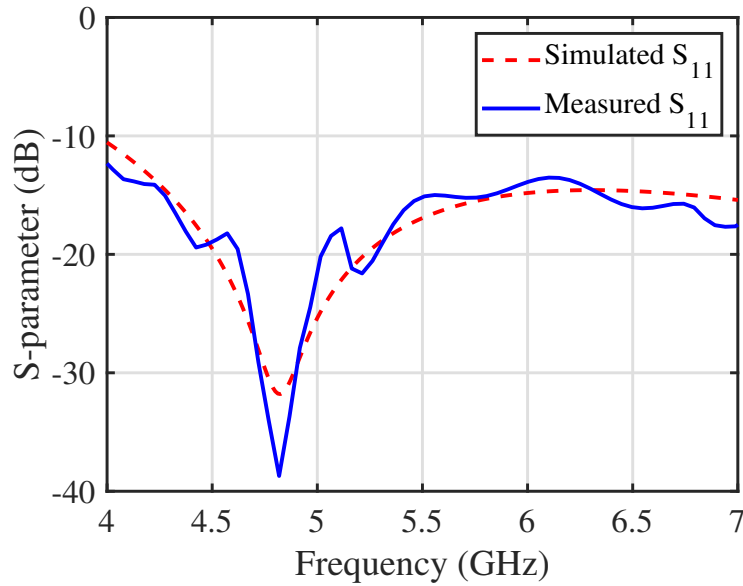


Fig. 4.9 Simulated and measured  $S_{11}$  of TM alone.

different  $H_g$  are shown. It could be seen that the efficiency is improved while using a shorter ground plane. However, the height of ground plane and feeding line cannot be reduced infinitely. A short ground plane may cause impedance matching issues and the connector may affect the radiation of the antenna if the feeding line is too short. So the value of  $H_f$  and  $H_g$  are chosen to be 2.6 mm and 0.5 mm respectively to achieve high efficiency while maintaining good impedance matching. The optimised TM achieves up to 74% radiation efficiency at the operating band. The simulated and measured  $S_{11}$  of the TM alone are shown in Fig. 4.9. The  $S_{11}$  below -10 dB is from 4 GHz to more than 7 GHz. The TM is connected to a SubMiniature version A (SMA) connector by silver conductive glue for measurement.

### Top PRS

The PRSs design is crucial to improve the directivity and gain. Generally, a higher directivity can be generated with highly reflective PRS by multiple in-phase superpositions. In many previously reported metal FPC antennas [95, 145, 148–150], the top PRS is designed to be a double-layer structure in which both layers are etched into some patterns to improve performances of the antennas. In the proposed transparent FPC with two PRSs, the top PRS

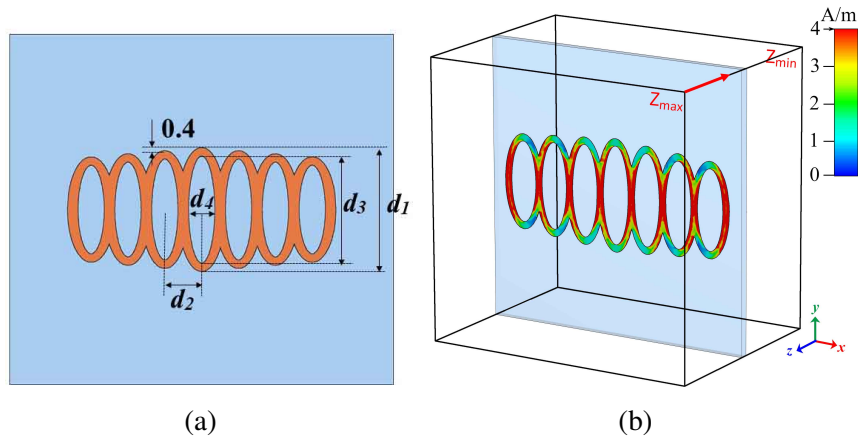


Fig. 4.10 The unit cell of top PRS, (a) geometry, (b) current distribution at 5.6 GHz.

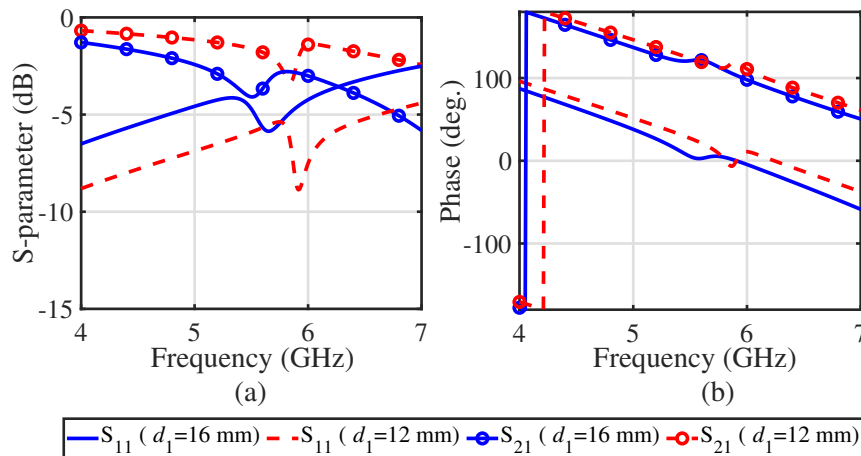


Fig. 4.11  $S$ -parameter of the unit cell on top PRS with different dimensions, (a) magnitude, (b) phase.

is relatively less reflective so that the number of repeated bounces in the cavity can be reduced and the reflection loss can be lowered. Meanwhile, most EM waves will transmit through the low reflective PRS and form a main beam toward the top direction. Considering the transparency requirement, the top PRS is designed in single-layer structure and the footprint of ITO film is minimised.

The unit cell of the top PRS is shown in Fig. 4.10(a). Since the current on the feed antenna is concentrated on the vertical edge of the fork along  $y$ -axis, the shape of the cell is designed to be an elliptical ring with the major axis along  $y$ -axis to obtain the strongest coupling from the source. The inner part of the elliptical ring is hollowed out to increase

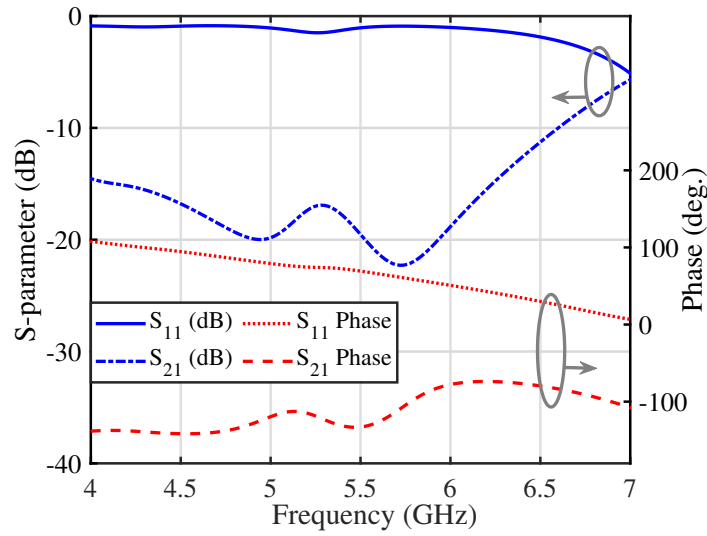


Fig. 4.12 S-parameter of the unit cell on bottom PRS.

optical transmittance. To obtain a gain enhancement over a broad band, 7 similar elliptical rings with different major axes are constructed. These rings are arranged horizontally and the major axes are stepped down from the middle to both sides as shown in Fig. 4.10(a). The outer major and minor axes of the centre ring are  $d_1$  and  $d_2 = 3.6$  mm respectively, while the inner major and minor axes of the centre ring are  $(d_3 = d_1 - 2)$  mm and  $d_4 = 2.5$  mm respectively. The difference of major axes between adjacent rings is 0.8 mm and the minor axes of all the rings are the same. Fig. 4.10(b) shows the current distribution at 5.6 GHz, which indicates the current is distributed vertically along the major axis direction of the elliptical ring. The top PRS is comprised of  $3 \times 3$  cells. The distance between adjacent cells in  $x$ -axis direction is  $x_1 = 32$  mm, while that in  $y$ -axis direction is  $y_1 = 24$  mm. As the distances from the feed antenna to the centre and edge cells are different, the edge cells are resized to compensate for the spatial phase delay. In our design, the major axis  $d_1$  of the centre ring of centre cell is 16 mm, while that of the edge cell is 12 mm. Fig. 4.11(a) shows the magnitudes of reflection coefficients ( $S_{11}$ ) and transmission coefficients ( $S_{21}$ ) of the centre cell ( $d_1 = 16$  mm) and edge cells ( $d_1 = 12$  mm), which reveals the partially reflective effect of the top PRS. When the EM wave incidents upon the top PRS, one part will be reflected back to the cavity to form the resonance, the other part will transmit through the PRS to generate the main radiation beam. Fig. 4.11(b) shows the reflection and transmission phases of cells with different major

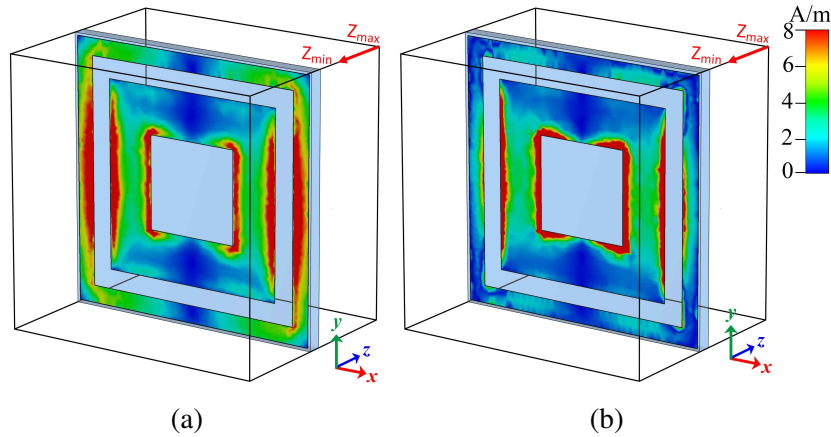


Fig. 4.13 Current distributions of the bottom cell at (a) 4.9 GHz and (b) 6.3 GHz.

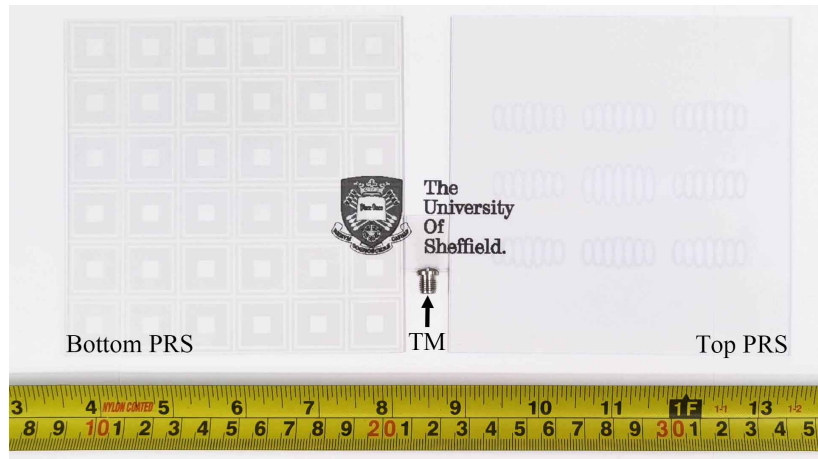
axes, in which the reflection phase satisfies (1) at around 5.6 GHz and the phase difference between different major axes can compensate for spatial phase delay.

### Bottom PRS

Typically, the bottom layer of the FPC is a fully covered conductive plane which acts as a reflective surface. To increase transparency, a highly reflective single-layer metasurface composed of hollowed ITO cells is designed as the bottom PRS. The magnitude and phase of the reflection coefficient are optimised so that most EM waves can be reflected back to generate Fabry-Perot resonance.

A single layer with  $6 \times 6$  ITO cells is designed on the bottom layer of the substrate. The geometry of the bottom unit cell can be seen in Fig. 4.7. It consists of two concentric hollowed out square rings. The outer and inner side lengths of the outer ring are  $L_1=19$  mm and  $L_2=17$  mm respectively, while these lengths of the inner ring are  $L_3=15$  mm and  $L_4=6$  mm respectively. The distance between adjacent cells is  $y_2 = 20$  mm. The hollowed area occupies 35% area of the bottom PRS, which increases 3% optical transparency of the TA compared with a fully covered ITO film.

The magnitude and phase of  $S$ -parameters of the bottom cell are shown in Fig. 4.12. Large  $S_{11}$  indicates high reflectivity of the bottom PRS. The reflective band of the cell (transmission coefficient lower than -10 dB) spans a wide range from 3.3 GHz to 6.6 GHz. The wideband



(a)



(b)

Fig. 4.14 Prototypes of the antenna, (a) components, (b) transparency comparison.

performance is attributed to the nested square rings which form a multi-resonance structure. The resonant frequency of the bottom cell can be adjusted by the side lengths ( $L_1$  and  $L_3$ ) of the square rings. The phase of the reflection coefficient satisfies (1) to form the FPC. Fig. 4.13 shows the current distribution on the bottom cell at 4.9 GHz and 6.3 GHz. It can be observed that at the lower frequency band, the current is mainly distributed on the outer ring; while the inner ring has strong current distribution at the higher frequency band.

### 4.2.3 Results and Discussion

The fabricated components are shown in Fig. 4.14(a). The ITO films are printed on the glass by magnetron sputtering and the shape is obtained by laser engraving technology. The

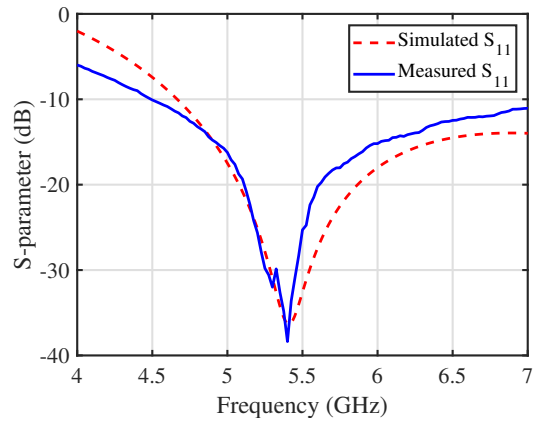


Fig. 4.15  $S_{11}$  of the FPC TA assembled together.

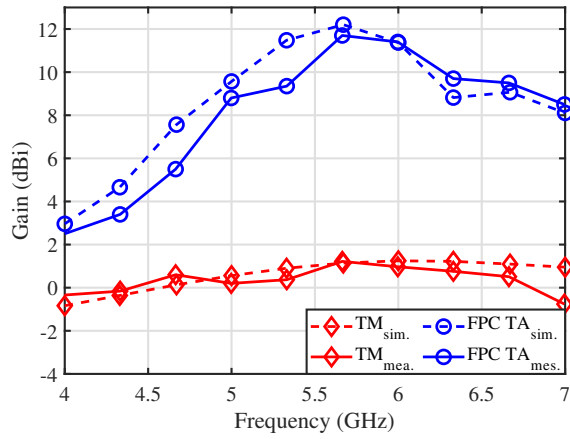


Fig. 4.16 Simulated and measured gains of the TM alone and the FPC TA.

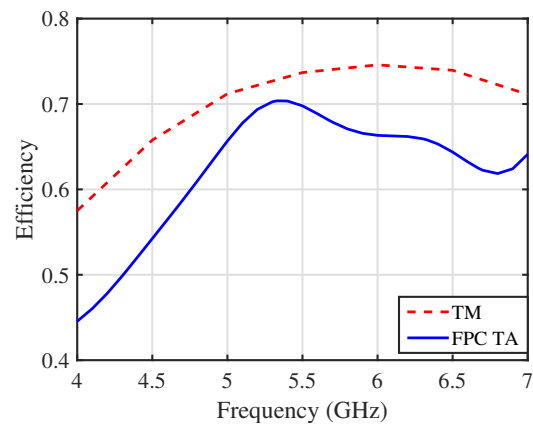


Fig. 4.17 Efficiencies of the TM alone and the FPC TA.

measured optical transparency of the whole transparent FPC antenna is 84%. As a reference, the transparency of the commercial double-layer window glass is up to 92%. Fig. 4.14(b) is the comparison of the proposed TA and commercial double-layer glass pieces on a window sill. The proposed TA shows its high transparency in the practical environment. The line of sight is clear through the antenna and the scenery seen through the antenna does not produce chromatic aberration.

The simulated and measured  $S_{11}$  parameters of the TA assembled together are shown in Fig. 4.15. The operating bandwidth for  $S_{11}$  lower than -10 dB is from 4.6 GHz to more than 6.5 GHz, which fully covers the 3 dB gain bandwidth discussed below.

In Fig. 4.16, the simulated and measured gains of the TM alone and the proposed FPC TA are shown. The gain of TM is low because of the omnidirectional radiation and large Ohmic loss. By using FPC, a directional radiation is generated and the gain is greatly improved from 1 dBi to 11.7 dBi around 5.6 GHz. The 3 dB gain bandwidth is from 4.9 GHz to 6.3 GHz. Compared to the TM, the FPC TA has obtained an average gain enhancement of 9.5 dB in the bandwidth.

In Fig. 4.17, the simulated radiation efficiencies of the TM and FPC TA are shown. Compared to the TM, the efficiency of FPC TA only degrades 3%-8% within the band of 4.9 GHz-6.3 GHz due to the reflection loss of the ITO PRSs. Although the efficiency of the FPC TA is reduced to 64%-70%, it outperforms most previously reported ITO antennas.

The simulated and measured radiation patterns of the FPC TA at 4.9 GHz, 5.6 GHz and 6.3 GHz are shown in Fig. 4.18, in which an apparent directional radiation pattern is observed. Although some EM waves can leak from the bottom PRS, a front-to-back ratio of 10 dB is achieved. The measured 3 dB beamwidths in E-plane are 20°, 17° and 15° at 4.9 GHz, 5.6 GHz and 6.3 GHz, respectively, while these values in H-plane are 16°, 14° and 14°, respectively.

In Table 4.3, the proposed TA is compared with the other high efficiency and high gain TAs. All the works in Table 4.3 utilised antenna arrays to enhance the gain of TAs. Micro-MM with high conductivity is used in [56] and [53] to construct transparent antenna arrays at millimetre wave band, however the constrained feeding network made the radiation efficiency

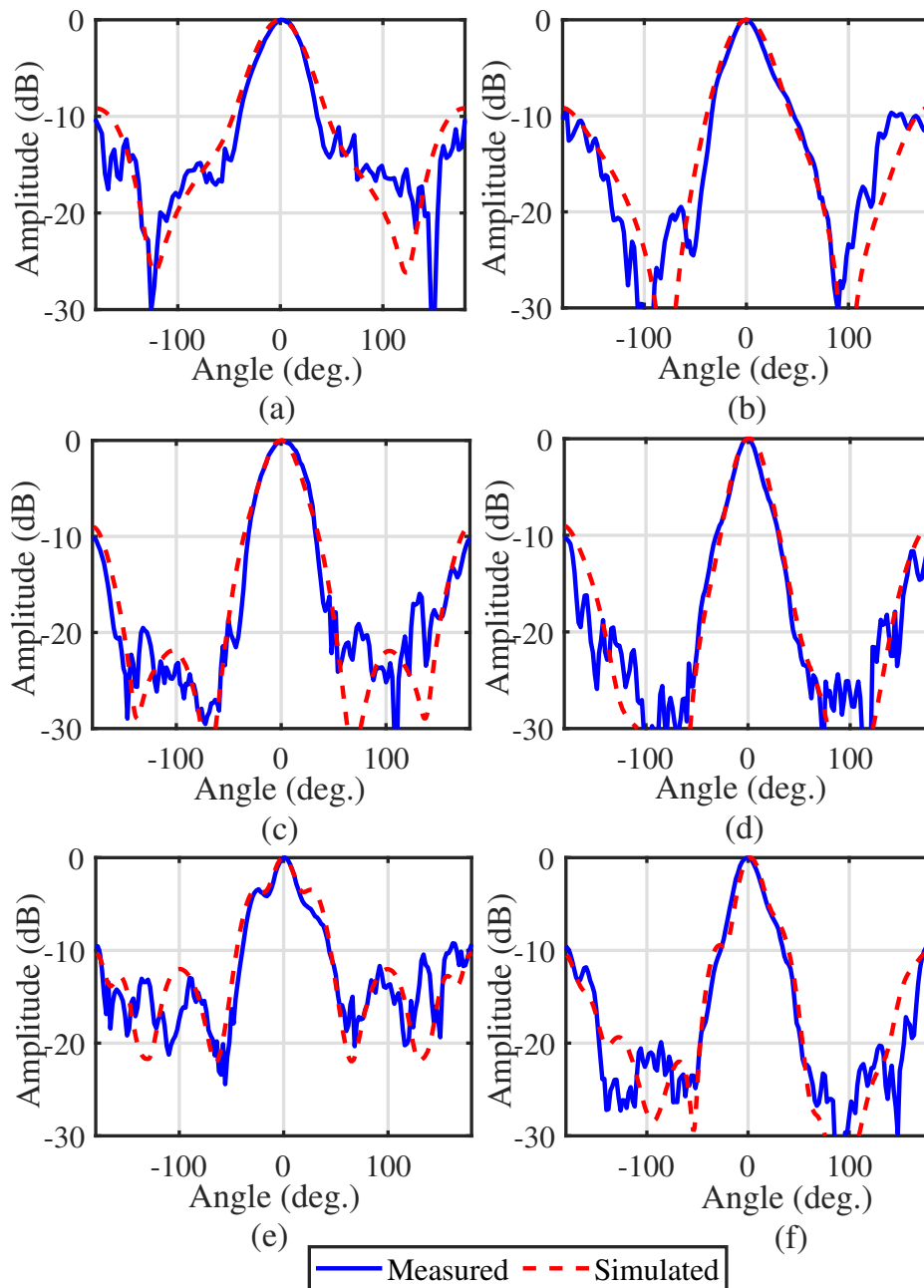


Fig. 4.18 Normalised radiation pattern: (a) E-plane at 4.9 GHz, (b) H-plane at 4.9 GHz, (c) E-plane at 5.6 GHz, (d) H-plane at 5.6 GHz, (e) E-plane at 6.3 GHz, (f) H-plane at 6.3 GHz.

Table 4.3 COMPARISONS OF HIGH EFFICIENCY AND HIGH GAIN TA

Ref.	Material	Transparency	3 dB Gain Bandwidth	Peak Gain (dBi)	Area ( $\lambda_0^2$ )	Radiation Efficiency	Feeding Type
[56]	MM antenna array	68%	58-61 (7.0%)	13.6	5×5	60%	Constrained feeding
[53]	Ni-embedded MM array	86%	24-28 (15.4%)	9.7	4×2	61%	Constrained feeding
[44]	ITO-copper FPC	90%	9-10.5 (15.4%)	15	3.2×3.2	65%	Constrained feeding (non-transparent source)
[45]	ITO-Ag microstrip array	45%	4.6-6.8 (38.6%)	5	0.9×0.5	70.8%	Constrained feeding
[96]	ITO reflectarray	-	25.5-32.5 (24.1%)	25.8	8.9×8.9	73%	Space feeding (non-transparent source)
[95]	MM transmitarray	-	27-29.5 (8.8%)	24.7	9.9×9.9	75.9%	Space feeding (non-transparent source)
<b>This work</b>	<b>ITO FPC</b>	<b>84%</b>	<b>4.9-6.3 (25.0%)</b>	<b>11.7</b>	<b>2.2×2.2</b>	<b>70.4%</b>	<b>Space feeding (transparent source)</b>

relatively low. In addition, the fabrication process of micro-MM in these works is complex and costly compared to that of ITO film. Metal doping technology is employed in [44] and [45] to improve the conductivity of ITO. In [44], although the PRS is made by Cu doped ITO with high optical transparency, the feeding network is based on non-transparent metal which makes the antenna not fully transparent. In [45], the efficiency is enhanced by silver sandwiched ITO, however the transparency is seriously degraded which limits its application. Based on spacing feeding, transparent reflectarray and transmitarray are proposed in [96] and [95], in which the radiation efficiencies are greatly enhanced. However, the feed sources in these works are non-transparent horn antenna and microstrip patch, respectively, which affects the transparency of the whole system and the overall transparency cannot be evaluated. In comparison, the proposed antenna is a fully transparent FPC antenna which obtains a good compromise between transparency and efficiency, and it achieves a high gain enhancement from 1 dBi of the feed source to 11.7 dBi of the FPC antenna with a relatively small aperture size. In addition, the proposed TA exhibits outstanding 3 dB gain bandwidth due to the specially designed PRSs. Furthermore, the source and PRSs of the proposed FPC antenna are based on a single-layer ITO structure, facilitating ease of manufacturing and seamless integration with indoor double glazing.

#### 4.2.4 Conclusion

In this section, a high efficiency and high gain transparent FPC antenna using ITO films has been proposed. A high efficiency TM is designed as the source antenna and two transparent PRSs are developed with ITO to construct FPC. The cells of the top PRS consist of multiple elliptical rings of different sizes to enhance the gain and extend gain bandwidth. The cells of the bottom PRS are in a hollowed-out square structure for high reflection and transparency. The proposed TA is fully transparent with an optical transparency of 84%. The 3 dB gain bandwidth is from 4.9 GHz to 6.3 GHz which serves for the middle band of 5G communication. The antenna achieves 64%-70% radiation efficiency within the operating band and a peak gain of 11.7 dBi without using any metal structure. With the densification of the wireless network deployment, reducing spatial congestion and visual obstruction are always expected for antenna design. The proposed TA serves as an excellent candidate in future indoor communications due to its high radiation performance and good integration with glass facilities.

# Chapter 5

## All-Dielectric Transparent Lens Antenna

### Overview

In this communication, an all-dielectric transparent lens (ADTL) using transparent resin for beamforming technologies are proposed. The ADTLs are optimised from the 3-D cosine surfaces, the conditions for beamforming can be satisfied by adjusting the wavelength and the amplitude of the cosine surface. A transparent monopole antenna is set as the source and overall 63-81% optical transparency is achieved. The circularly polarised incident wave can be formed to a gain enhanced pencil beam, flat-top beam and adjustable dual-beam in different wavelengths and amplitude. Three ADTL prototypes are fabricated by 3-D printing and measured to verify the beamforming functions. The 1st ADTL forms a single beam to 8.6 dBi gains with 7.5 dB enhancement, the 2nd ADTL achieves about 48° flat-top beam within 1 dB beamwidth and the 3rd ADTL generates a dual-beam with maximum 90° deflection angle.

### 5.1 Introduction

Wireless communication happens most in buildings, where always have many obstacles including walls and furniture [151]. The escalating demand for indoor communication devices poses a significant challenge due to the exorbitant costs associated with limited indoor space [143]. Nevertheless, conventional antennas that without integrating with the

environment or customized features exclusively designed for indoor usage are incapable of fulfilling the impending requirements. To address this, environmental adaptive antennas with customized radiations must be valued, such as the high-gain pencil beam antenna for corridors, the flat-top beam antenna for rectangular rooms, and the multi-beam antenna for corners.

Lens antennas are optimally compatible for indoor environment in wireless functions. The recent publications have reported the lenses for beamforming on radiation patterns. [152] reports the gain enhancement and through-the-wall method using lens on Vivaldi antenna. Beam-steering is achieved using fluidically reconfigurable lens in [153] and metamaterial Luneburg lens in [154]. In [155, 156], dielectric materials are applied to design compact lenses for flat-top radiation patterns. Multiple-beam are generated by dual-layer Rotman lens in [157] and compact geodesic-lens antennas [158]. The characteristics of directionality, interference reduction capacity, higher gain, compact dimensions and low profile endow lens antennas with significant utility for wireless communication in indoor settings. However, most lens antennas target to a single scene, consume significant space and detract from the aesthetic appeal of the interior, which runs counter to the principles underlying the advancement of smart building technology. The lens antenna with customized radiation properties and can seamlessly integrated with indoor settings has not been investigated.

In recent year, TAs are favoured by space-constrained environments due to their high concealment [159]. However, the application of TAs is limited primarily by low efficiency and low gain, which stem from the high resistance of TCFs [144]. The incorporation of a transparent dielectric as the lens body can mitigate losses while preserving transparency [160]. Thus, a lens antenna with beamforming functions based on transparent dielectric materials is expected to meet the requirements.

This communication proposes the dielectric cosinusoidal transparent lens antenna for multiple-purpose beamforming techniques. Assembling with a transparent monopole source antenna using ITO film, it achieves 63-81% transparency. Gain enhancement, flat-top beam and dual-beam of beamforming technologies are realised by adjusting the parameters of the cosinusoidal surface. The lens antenna operates at around 6 GHz for middle band 5G

communication to benefit indoor applications. The fabrication of the metasurfaces uses 3-D printing technology with low cost transparent resin material.

## 5.2 Cosinusoidal Lens Mechanism

Referring to the conductive metasurfaces, when the metasurface is excited, the radiation pattern generated by its surface current superimposes with that of the source antenna to achieve beamforming. Similarly, the forced electric field in a dielectric material obstructs the incident field and causes refraction. Assume a surface is represented by  $r(\eta)$ , Snell's law on the interface is given by [161]

$$\frac{\partial r}{\partial \eta} = \frac{nr(\eta)\sin(\theta - \eta)}{1 - n\cos(\theta - \eta)} \quad (5.1)$$

where  $n$  is the refractive index of the media,  $\theta$  denotes the angles between the incident ray and reference plane, and  $\theta$  denotes the angles between the output ray and reference plane. Different surface structures can act as converging, diverging or non-refracting. In optics, the hyperbolic lens is the most effective converging lens, the inner surface, which is closer to the feeding source, is expressed in polar coordinates as

$$r_1(\eta) = \frac{F(n-1)}{n\cos(\eta) - 1} \quad (5.2)$$

where  $F$  is the focal distance of the surface. A flat plane outer surface which only increases the angle of refraction can be expressed as

$$r_2(\eta) = \frac{1}{\cos(\eta)} \quad (5.3)$$

The surface that is always perpendicular to incident rays, for example, the inner surface of the elliptical lens remains the transmission direction [162].

The combination of the above three surfaces enables purposeful modification of the beam shape. However, as a transparent metasurface, the transparent effect must be considered.

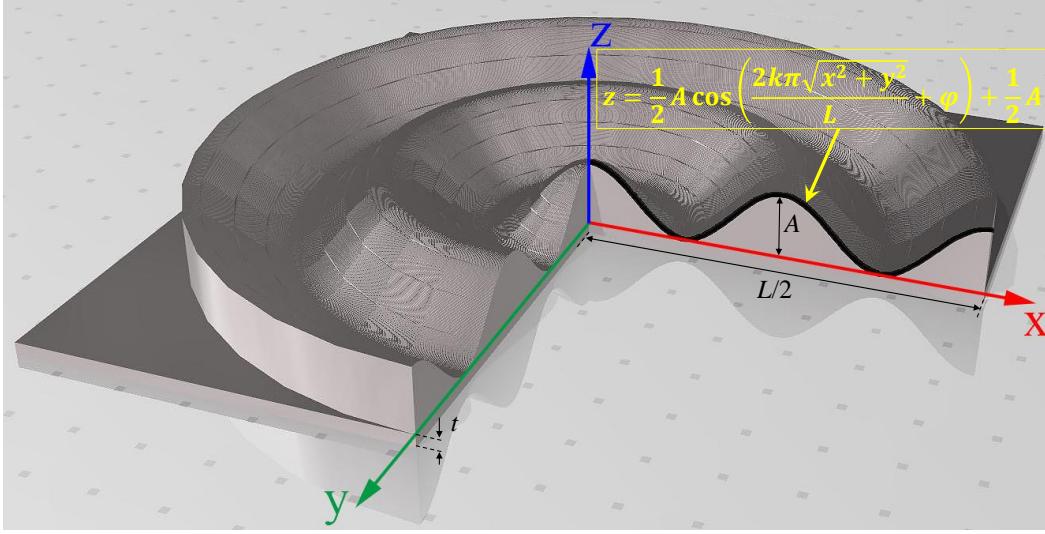


Fig. 5.1 The 3-D geometry of the dielectric ADTL.

Simply arranging the hyperbolic and elliptic surfaces on a flat plane will leave shadows and gaps at the boundaries. Using continuous and smooth surfaces to approximate the combination of them is an optimal choice for balancing performance and visual effects. A continuous curved surface constructed using the cosine function is one of the potential surfaces to meet all conditions. Physically, the surface is continuous and smooth transition, which does not produce shadows with clear boundaries. In the EM theory, its impedance changes gradually with the thickness of the medium. In optics, it can approximate hyperbolic surface and ellipsoid for ray refraction. Though the EM wave may have interference and diffraction, the main lobes can be predicted.

The proposed ADTLs are constructed by a 3-D cosine surface ( $S_1$ ) from the centre outward and a square base with thickness  $t = 2$  mm as shown in Fig. 5.1. The surface  $S_1$  is expressed as

$$z = \frac{1}{2} A \cos\left(\frac{2k\pi\sqrt{x^2+y^2}}{L} + \varphi\right) + \frac{1}{2} A \quad (5.4)$$

where  $A$ ,  $k$ ,  $\varphi$  and  $L$  denote the amplitude, period, phase and diameter, respectively. By a comprehensive analysis of the feasibility of gain enhancement, flat-top beam and dual-beam realisation condition, as well as parameter sweeps,  $L$  is set to 120 mm and  $\varphi$  is set to 0. A metasurface of this size can be easily installed indoors without being crowded.

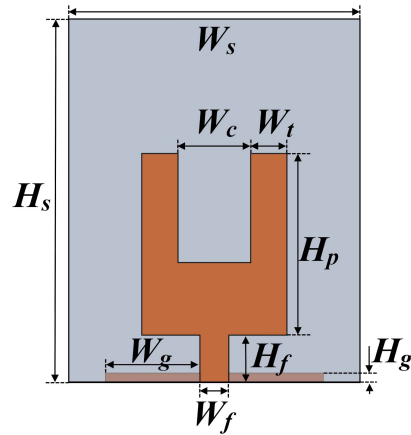


Fig. 5.2 The geometry of transparent monopole feeding antenna, the dimension is shown in Table I.

Table 5.1 DIMENSIONS OF THE TRANSPARENT MONOPOLE

Parameter	$W_s$	$W_c$	$W_t$	$W_g$	$W_f$	$H_s$	$H_f$	$H_p$	$H_g$
Value(mm)	16	4	2	5.2	1.6	20	2.6	10	0.5

## 5.3 ADTLs Antenna Design

The ADTLs are made of transparent resin with a dielectric constant of 4. An optimal illuminate distance  $d = 50$  mm between the source and  $S_2$  of ADTLs at 6 GHz is determined by parametric sweep. All the radiation patterns are simulated in CST 2021 Microwave Studio.

### 5.3.1 Feeding Antenna

To keep the overall miniaturization and transparency of the antenna with ADTLs, a transparent monopole feeding antenna is designed. The antenna uses  $4 \Omega/\text{sq}$  ITO film and glass substrate with 6.15 dielectric constant and 1.1 mm thickness. The antenna geometry is shown in Fig. 2 and its dimension is shown in Table I. The patch in the shape of a tuning fork can generate a broadside polarisation in  $yz$ -plane at 6 GHz. As the radiation pattern in  $xz$ -plane can be deviated by the cable and connector and the metasurfaces are rotationally symmetric, all the radiation pattern simulation are performed in  $yz$ -plane.

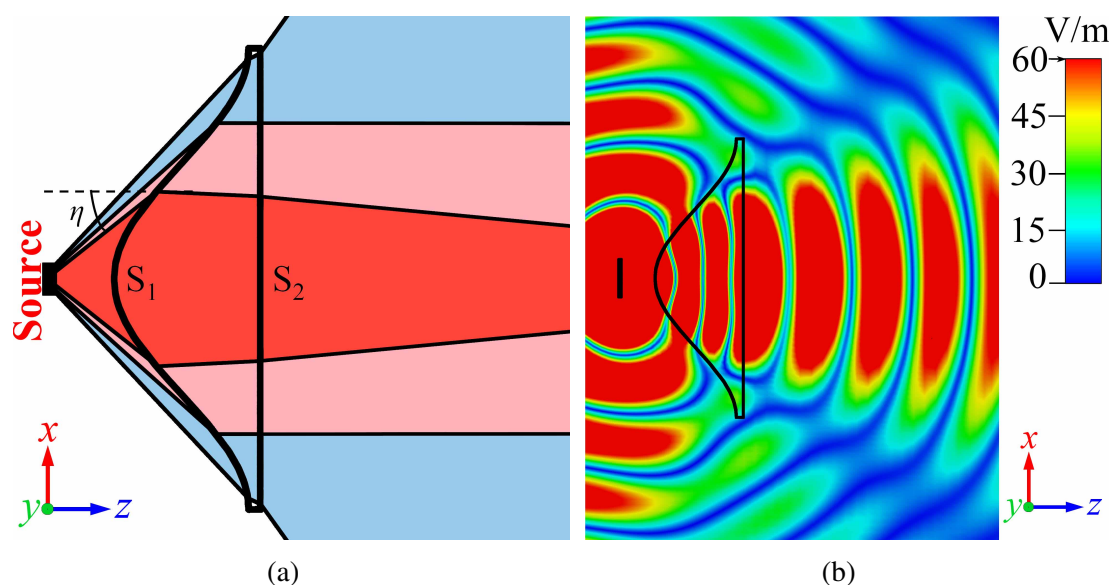


Fig. 5.3 (a) Ray tracing schematic diagrams of ADTL 1 ( $A = 26$  mm and  $k = 0.33$ ) at 6 GHz. Red, pink and blue zones denote the radiation intensity of the beam from strong to weak and the thin black lines represent the rays. (b) Electric field distribution on  $xz$ -plane of ADTL 1.

### 5.3.2 ADTL 1

Fig. 5.3(a) presents the ray tracing schematic diagrams of ADTL 1 with  $A = 26$  mm and  $k = 0.33$ . The peak of surface  $S_1$  approximates the ellipsoid with a focal length  $F$  of 52 mm and a major axis of 60 mm. Combined (5.1) and (5.2), the path of the rays can be obtained. In the transition from peak to trough, a large area of  $S_1$  approximates an inclined plane. Compared with the spherical surface, the inclined surface can obtain a larger radiation area. Therefore, ADTL 1 shows converging ability in a wide radiation range. The rays within  $\pm\eta = 53^\circ$  are focused, which greatly increases gain and presents a pencil beam. Fig. 5.3(b) shows the electric field of ADTL 1 at 6 GHz. The TM generates a circular electric field on  $xz$ -plane, it is obviously affected after entering  $S_1$ . The continuous circular electric field is broken by the low electric field in the direction of about  $50^\circ$  with the  $z$  axis, which is consistent with the ray tracing diagram. A strong electric field is generated in the  $z$ -axis direction.

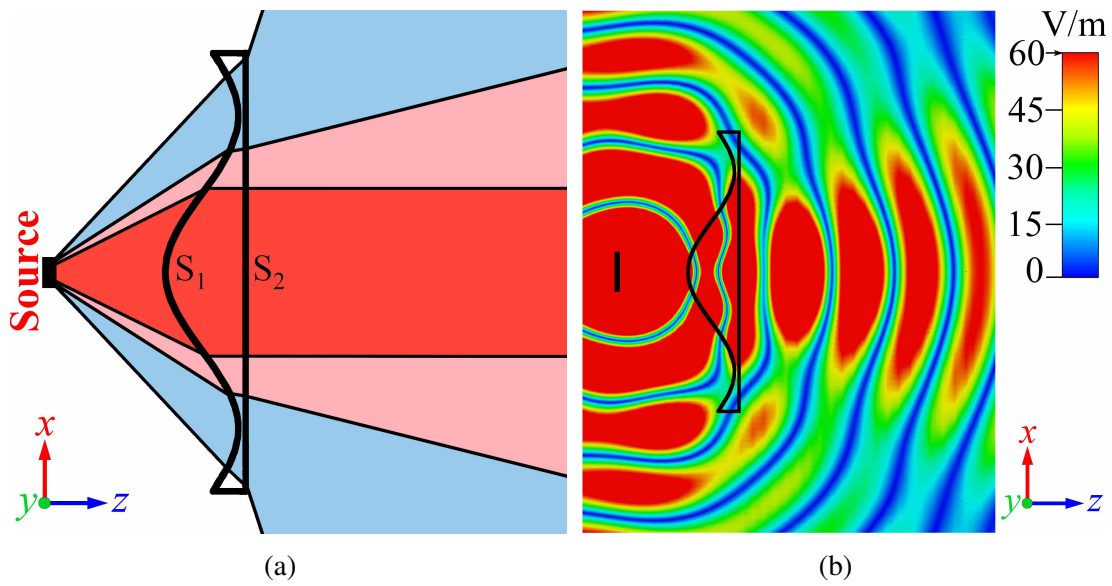


Fig. 5.4 (a) Ray tracing schematic diagrams of ADTL 2 ( $A = 20$  mm and  $k = 0.7$ ) at 6 GHz, (b) electric field distribution on  $xz$ -plane of ADTL 2.

### 5.3.3 ADTL 2

Fig. 5.4(a) shows the rays refracted by ADTL 2 with  $A = 26$  mm and  $k = 0.6$ . The peak of ADTL 2 is approximate to the ellipse with a focal length of 74 mm and a major axis of 85 mm. Compared with ADTL 1, the centre of ADTL 2 is slightly less refractive, and the refracted rays in the red zone are almost parallel to the  $z$ -axis rather than focusing on a point. Beam power gradually decreases as the rays diverge slowly in the pink zone. The radiation power through ADTL 2 toward  $z$ -axis direction is uniform in a wide range which produces a flat-top beam. Fig. 5.4(b) shows its electric field on  $xz$ -plane at 6 GHz. On surface  $S_2$ , a strong and flat electric field can be observed and it spreads toward  $z$ -axis direction. The main lobe is from concentration on  $S_2$  to divergent as the transmission distance increase. The electric field decreases slowly with blurred edges. Compared with ADTL 1, the high level of ADTL 2 in the  $z$ -axis direction has a larger distribution angle to the  $x$ -axis direction and decreases slower. Thus, ADTL 2 can provide a much wider beamwidth with a flat top. The simulated electric field agrees with the ray tracing diagram of ADTL 2.

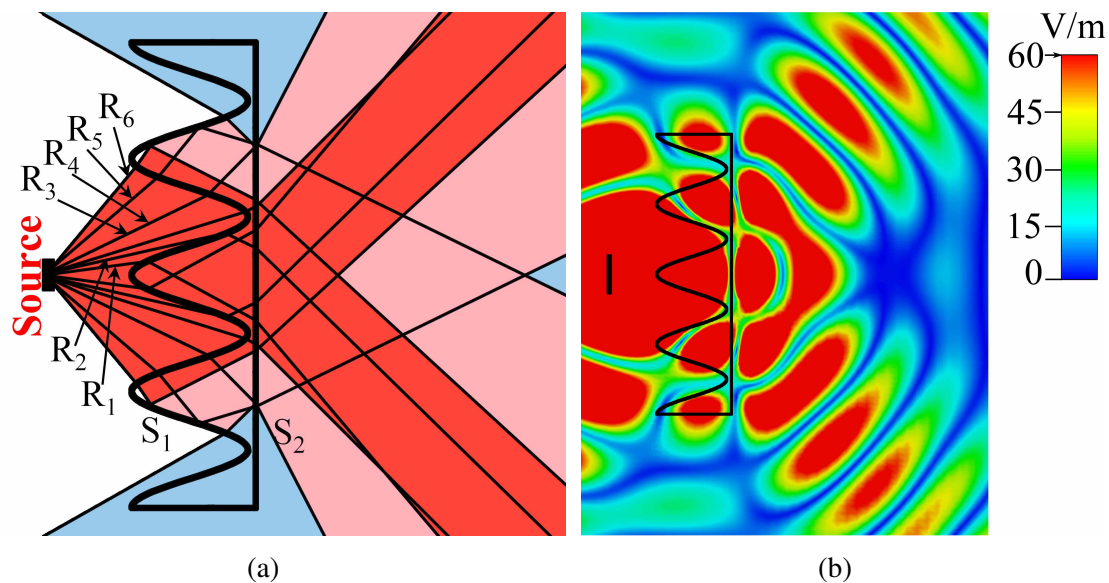


Fig. 5.5 (a) Ray tracing schematic diagrams of ADTL 3 ( $A = 30$  mm and  $k = 2$ ) at 6 GHz, (b) electric field distribution on  $xz$ -plane of ADTL 3.

### 5.3.4 ADTL 3

Increasing the incidence angle using a cosine surface with a shorter wavelength, the main beam can be split to dual-beam and the deflection angles can be adjusted by the surface parameters. Fig. 5.5(a) presents the ray tracing diagram of ADTL 3 with  $A = 30$  mm and  $k = 2$ . The focus of the centre peak is inside the ADTL, the incident rays represented by  $R_1$  and  $R_2$  are refracted cross the metasurface centre. Rays  $R_3$  and  $R_4$  inject at the troughs with the small incident angle at  $S_1$  and further refracted by  $S_2$  away from the  $z$ -axis. At  $S_2$ , the incident angle of  $R_4$  is the critical angle, thus total internal reflection will occur on the rays with a larger incident angle than that of  $R_4$ . The peaks beside the centre peak reduce the number of escaping rays as they have a large incident angle from dielectric to air. The rays represented by  $R_5$  and  $R_6$  are totally reflected while trying to exit the dielectric from  $S_1$ . The total reflected rays shoot out from  $S_2$  and then merge into the direction of the dual-beam. The deflection angle of the beams can be adjusted by  $A$  and  $k$ . Increasing  $k$  can have a stronger refractive ability which increases the deflection angle but decreases the irradiated area. Adjusting  $A$  can effectively reduce the side lobe. Fig. 5.5(b) shows the electric field

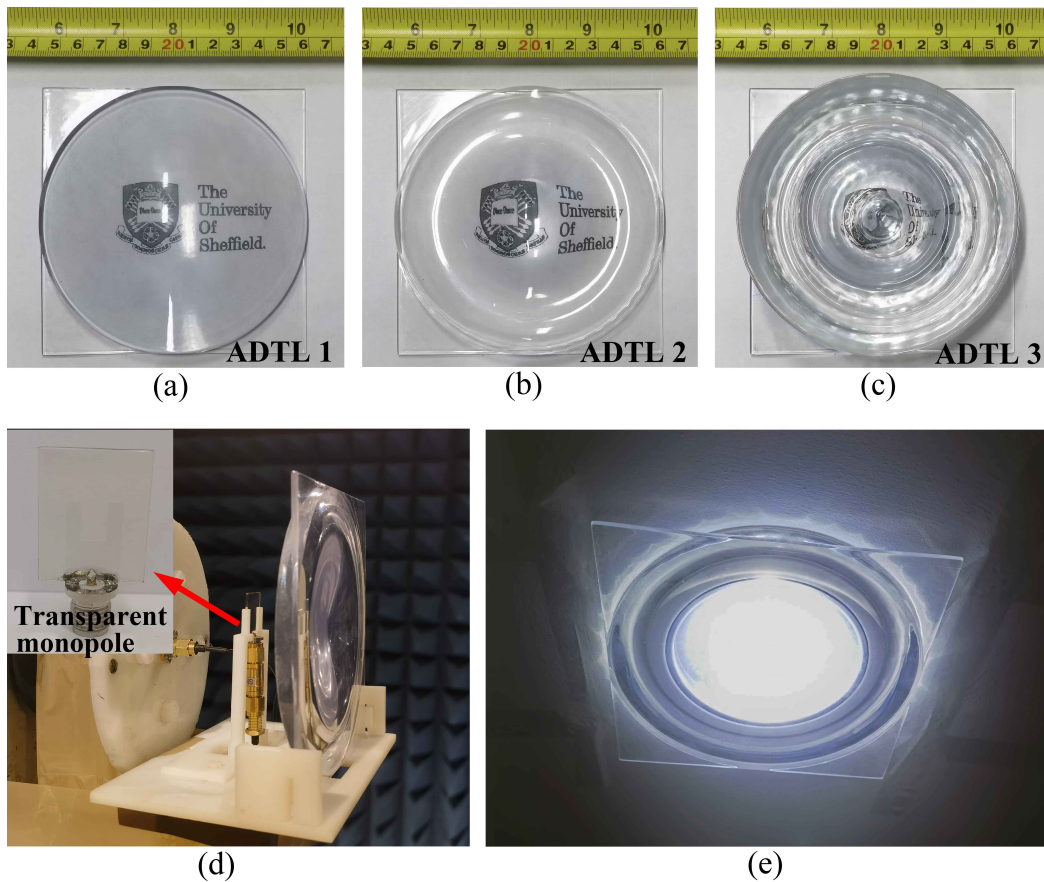


Fig. 5.6 The prototypes of (a) ADTL 1, (b) ADTL 2 and (c) ADTL 3. (d) The measurement setup and TM prototype. (e) The application on spotlight.

through ADTL 3. Corresponding to the ray tracing diagram, the electric field is separated after output from the ADTL 3 and radiated two ways with a similar angle.

## 5.4 Experiment Results

The ADTL prototypes are fabricated using transparent UV curable resin by stereolithography (SLA) 3-D printing. The fast curing reaction by UV irradiation allows printing of high resolution with edge accuracy of 0.1 mm. The model is then polished and sprayed UV high-transparency oil to achieve high transparency. Fig. 5.6(a)-(c) show the prototypes of ADTLs, ADTL 1 and 2 show good visualisation ability to the logo content. Though the logo is distorted by ADTL 3, it is still can be read. Their optical transparency is obtained

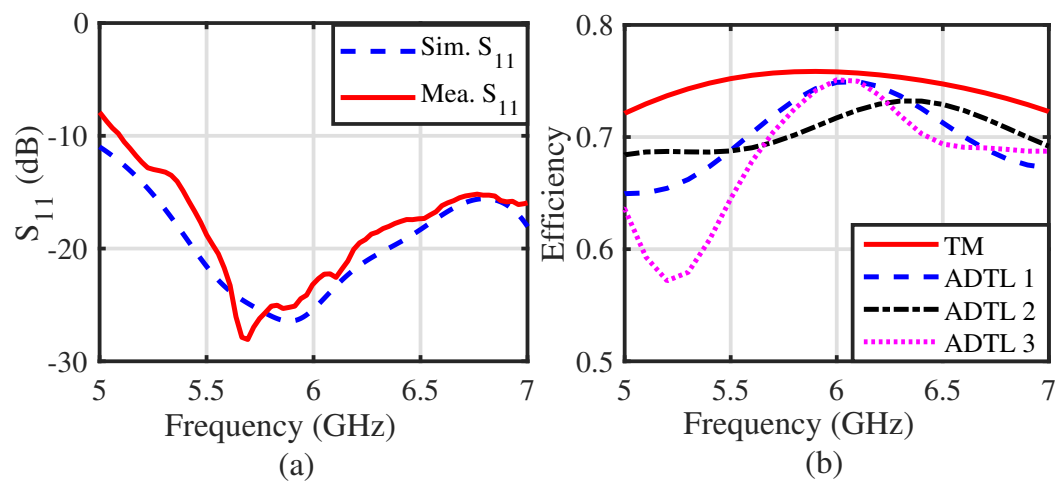


Fig. 5.7 (a) The reflective coefficients of the proposed antenna, (b) radiation efficiencies of feeding and with ADTLs.

by taking the average value of multi-point measurements, which are 74% (ADTL 1), 81% (ADTL 2) and 63% (ADTL 3). Fig. 5.6(d) shows the radiation pattern measurement setup and the prototypes of feeding antenna. Fig. 5.6(e) shows the real time applications of the ADTLs integrated in spotlight. In practice, the feeding and circuit can be hidden within the lampshade to achieve real invisible antenna.

Fig. 5.7(a) presents the simulated and measured reflective coefficients of the feeding antenna with ADTL 1. The other surfaces have almost identical  $S$ -parameter, so only the ADTL 1's is shown. The desirable metasurface operating band 5.6-6.4 GHz is covered by the measured band from 5.1 to 7 GHz. Fig. 5.7(b) shows the radiation efficiency of the feeding antenna and with the ADTLs. Low efficiency is the main problem plaguing TAs, using transparent conductive materials such as ITO as a metasurface will greatly reduce the efficiency. Fig. 5.7(b) shows the maximum efficiency of the feeding antenna is 75% and the combination with ADTLs only results in about 2% reduction. The efficiency drop is usually more than 20% while using transparent conductive film as metasurface. The radiation efficiencies of the antennas are 67%-73% from 5.6 to 6.4 GHz.

Fig. 5.8(a), (b) and (c) shows the simulated and measured radiation pattern of ADTL 1 at 5.6 GHz, 6 GHz and 6.4 GHz. The source antenna provides uniform irradiation at this band then the ADTL 1 forms the pattern to a sharp beam. Fig. 5.8(d) presents the gains of feeding

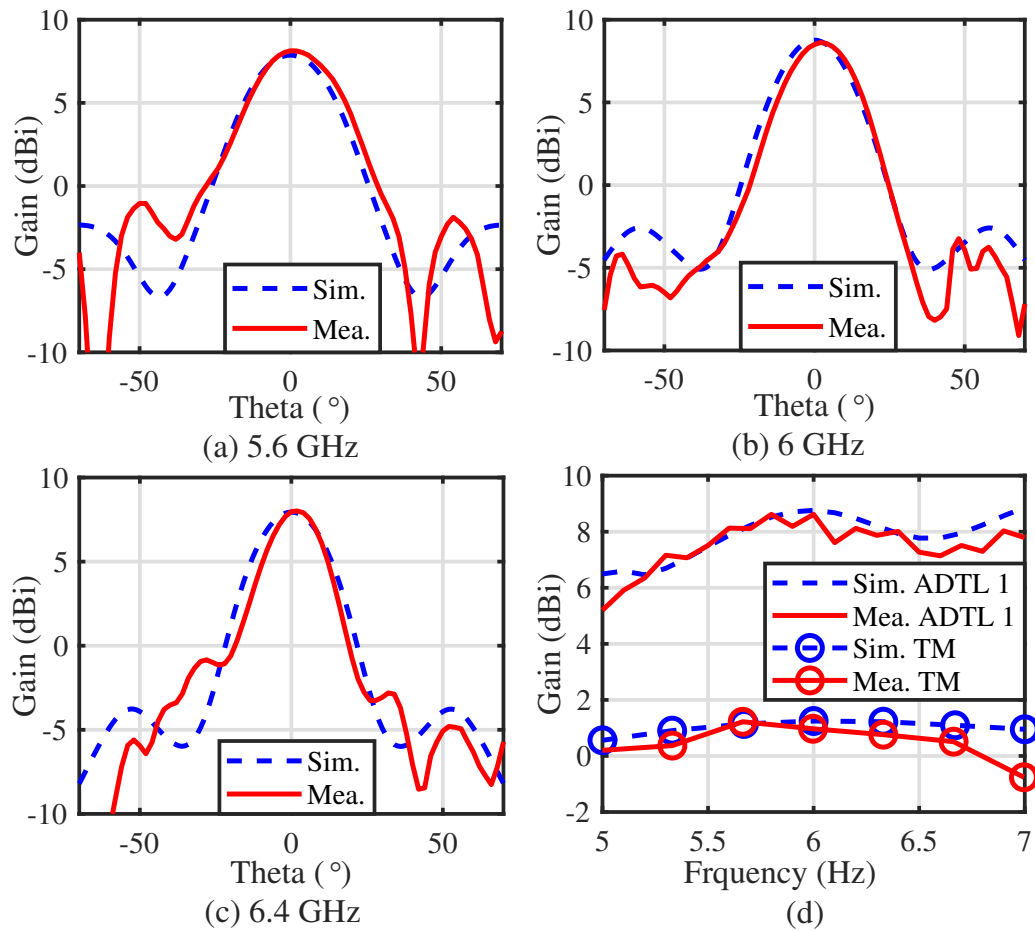


Fig. 5.8 Radiation pattern of ADTL 1 and feeding antenna at (a) 5.6 GHz, (b) 6 GHz and (c) 6.4 GHz. (d) The gains of feeding antenna and with ADTL 1

and feeding with ADTL 1. The measured peak gain has been enhanced from 1.1 to 8.6 dBi. The gains fluctuate within 1 dB from 5.6 to 6.4 GHz and it achieves 8.1 dBi at 5.6 GHz, a maximum 8.6 dBi at 6 GHz and 8 dBi at 6.4 GHz. The simulated and measured results are matched.

Fig. 5.9 shows the simulated and measured radiation patterns generated by ADTL 2. The simulated 1 dB beamwidths are  $54^\circ$  at 5.6 GHz in Fig. 5.9(a),  $50^\circ$  at 6 GHz in Fig. 5.9(b) and  $49^\circ$  at 6.4 GHz in Fig. 5.9(c), while the corresponding measured achieves  $48^\circ$ ,  $44^\circ$  and  $46^\circ$ . The measured maximum gains are 2.8 dBi, 4.1 dBi and 3.8 dBi. Over the band of 5.6-6.4 GHz, ADTL 2 provides a stable flat-top effect and the spanned angle of the flat-top beam fluctuates at  $46 \pm 2^\circ$ . As the frequency rises, the refractive ability of the surface is enhanced.

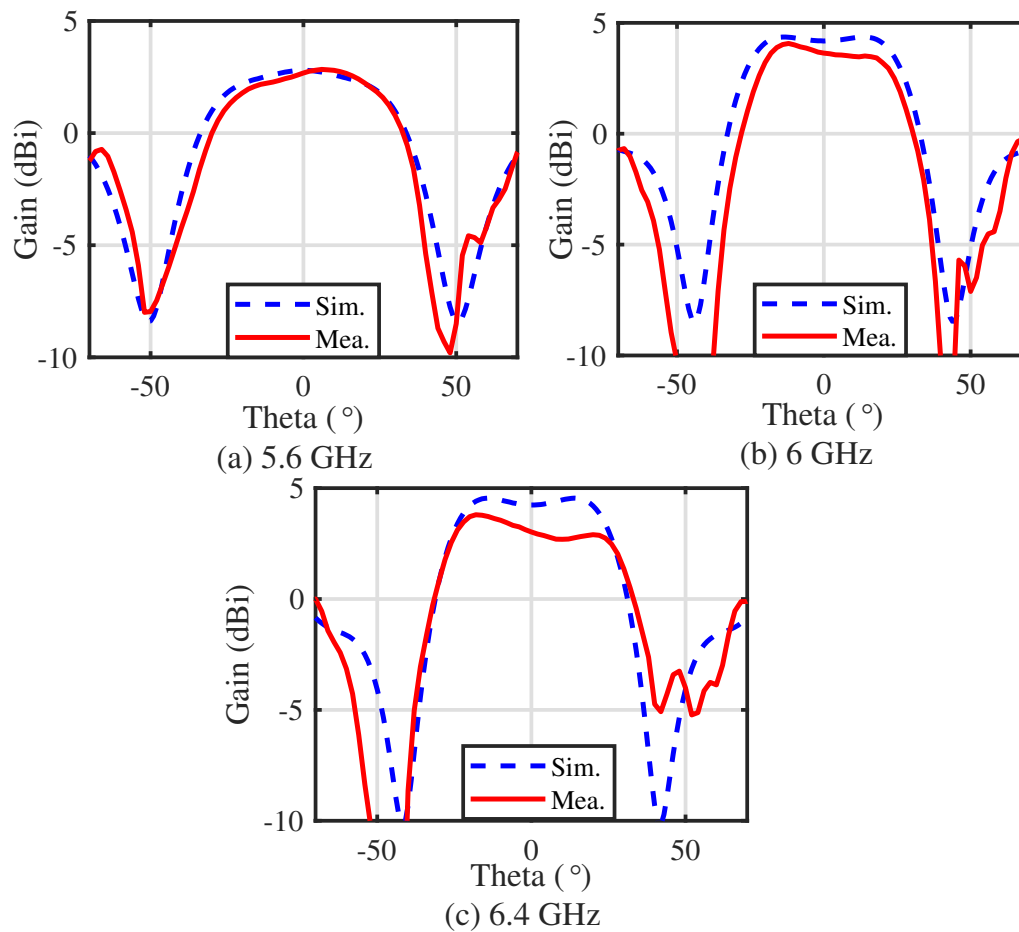


Fig. 5.9 Radiation patterns of ADTL 2 at (a) 5.6 GHz, (b) 6 GHz and (c) 6.4 GHz.

It can be seen that the direction of maximum gain points deviates symmetrically from the  $0^\circ$  to outward. At higher frequencies, the rays are excessively refracted and the trend of dual-beam can be seen. This means that a proper increase in the refractive capability of the ADTL can produce dual-beam or even multiple beams.

In Fig. 5.10(a), the normalised dual-beam radiation patterns of the ADTLs with different  $A$  and  $k$  are shown. ADTL 3a ( $A = 28$  mm and  $k = 1$ ) converts the flat top wave of ADTL 2 into a dual-beam with a minimum deflection angle  $\pm 25^\circ$  between the beams. By continuous increasing  $k$ , ADTL 3b ( $A = 15$  mm,  $k = 1.5$ ) produces dual-beam with  $\pm 35^\circ$  at 6 GHz. ADTL 3 ( $A = 30$  mm,  $k = 2$ ) achieves the maximum angle  $\pm 45^\circ$  of the dual-beam polarisation. The radiation patterns of ADTL 3 are shown in Fig. 5.10(b), (c) and (d). The simulated and measured deflection angles of ADTL 3 are about  $\pm 46^\circ$  at 5.6 GHz,  $\pm 45^\circ$  at 6 GHz and

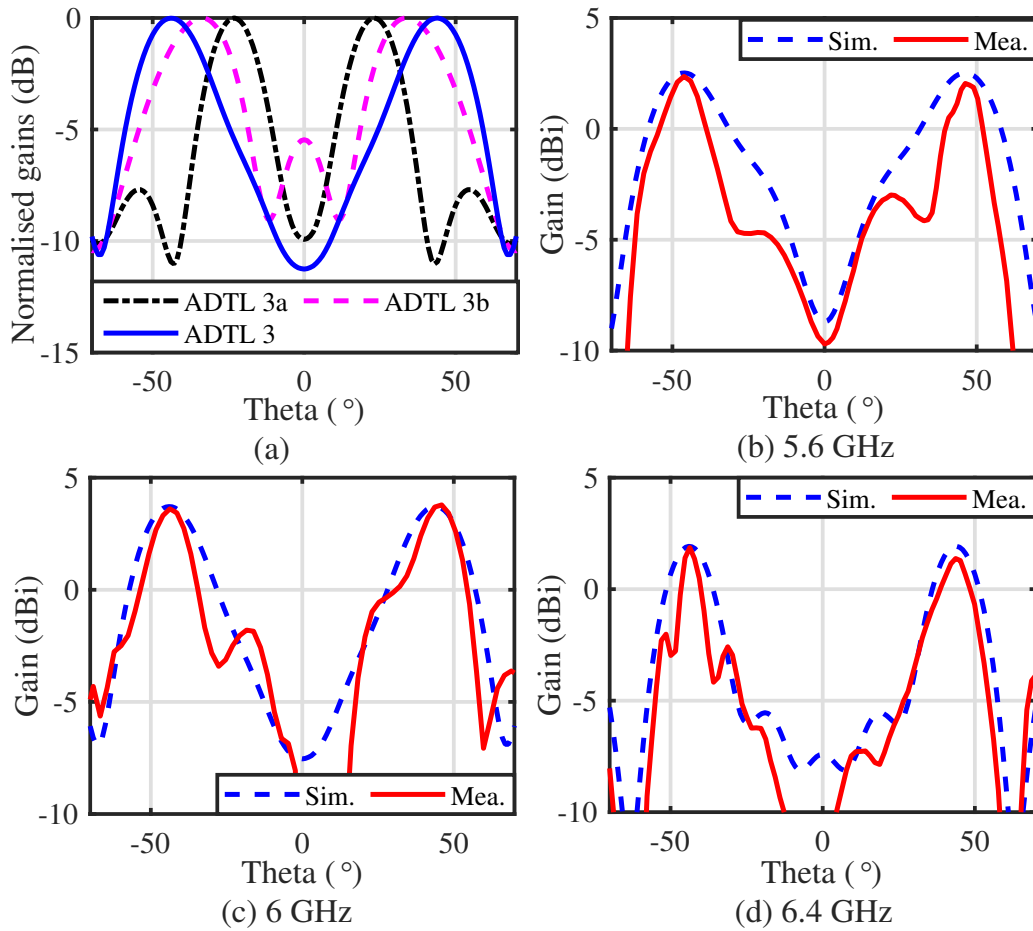


Fig. 5.10 (a) Dual-beam radiation patterns of ADTL 3a ( $A = 28$  mm and  $k = 1$ ), ADTL 3b ( $A = 15$  mm,  $k = 1.5$ ) and ADTL 3 ( $A = 30$  mm and  $k = 2$ ) at 6 GHz. Simulated and measured radiation pattern of ADTL 3 at (b) 5.6 GHz, (c) 6 GHz and (d) 6.4 GHz.

$\pm 43^\circ$  at 6.4 GHz, respectively. The angle variation is limited within  $\pm 3^\circ$  over the operating band. The corresponding gains achieve 2.4 dBi, 3.8 dBi and 1.9 dBi. Moreover, a continued increase in  $k$  will result in more beams. More peaks on the surface will lead to complex refraction and reflection. It is not conducive to independent adjustment of the beams and the gains are reduced.

Table 5.2 shows the comparison between the proposed ADTLs and related metasurface research. ADTL 1 is compared with an all-dielectric metasurface for gain enhancement. Although the EM waves in the low frequency band are less sensitive to the refraction of the medium, the proposed ADTL 1 still achieves a good gain enhancement of 7.5 dB compared to [108, 163, 164]. As the dielectric metasurface for flat top radiation pattern

Table 5.2 COMPARISONS OF SIMILAR DESIGNS

Ref.	Structure	Bands (GHz)	Enhanced gain	Transparent
[108]	GA optimised	9-20	7-12 dB	No
[163]	Comb mushroom-like	14-20	4.7	No
[164]	Permittivity varies	6.3-8.2	4.7-8 dB	No
<b>ADTL 1</b>	<b>3-D Cosine surface</b>	<b>5.6-6.4</b>	<b>7.5 dB</b>	<b>Yes</b>
Ref.	Structure	Bands (GHz)	BW <sub>(1dB)</sub>	Transparent
[165]	2-D leaky-wave	9.6-10.2	40°	No
[166]	Nonuniform leaky-wave	5.8	33°	No
[167]	8×8 array	1.7-2.7	50°	No
<b>ADTL 2</b>	<b>3-D Cosine surface</b>	<b>5.6-6.4</b>	<b>48°</b>	<b>Yes</b>
Ref.	Structure	Bands (GHz)	Beam span	Transparent
[168]	Huygens' structure	58.5-61	12°	No
[169]	Spherical particles	3.2	120°	No
[170]	Grating	60	50°	No
<b>ADTL 3</b>	<b>3-D Cosine surface</b>	<b>5.6-6.4</b>	<b>90°</b>	<b>Yes</b>

has not been explored beyond 10 GHz, ADTL 2 is compared with the antennas with metal metasurfaces. ADTL 2 achieves larger beamwidth than the antennas in [165, 166] and comparable beamwidth with [167]. The proposed work is not inferior to the traditional metal antenna in terms of beamwidth performance. ADTL 3 is compared with other all-dielectric designs. [168] can achieve gain enhancement and dual-beam, however, the beams can only be separated by 12°. [169] achieves the spanned angle that increases with frequency and reaches the maximum of 120° at 3.2 GHz. Based on the dielectric grating, [170] achieves a fixed beam span angle of 50°. The proposed ADTL 3 achieves adjustable beams from 50° to 90° at a fixed frequency band. The angle of dual-beam controllability of ADTL 3 is better than the others. The excellent beam adjustment capability enables ADTLs to achieve outstanding results in terms of gain enhancement, flat-top beamwidth and dual-beam angle

adjustment. More importantly, the ADTLs achieve unprecedented transparency effects in the case of multi-purpose beamforming metasurfaces.

## 5.5 Conclusion

A kind of ADTL using optics lens mechanism is proposed. The ADTLs based on 3-D cosine surface realise 8.6 dBi gain with 7.5 dB enhancement, flat-top beam with  $48^\circ$  1 dB beamwidth and adjustable dual-beam within  $90^\circ$ . The fabricated prototypes remain at least 63% optical transparency. According to the application environment, the optimal beamforming function can be adapted by matching the suitable phase and amplitude of the ADTLs and the transparency effect can relieve the difficulties of deployment in compact space. The proposed work can promote adaptive beamforming services for a variety of complex environments, especially indoors.



# Chapter 6

## Conclusions and Future Work

### Overview

**Section 6.1** firstly summarises the achievements of each effort. Their connections, different challenges and solutions are disclosed. Secondly, the novelties of the thesis are summarised. Finally, the promotion of the thesis is emphasised. In **section 6.2**, the continuation of TA work and the framework required to support future TAs applications are described and envisioned.

### 6.1 Conclusions

In Chapter 1, the author expounds that TA has broad application prospects but faces many challenges. The indoor wireless devices must conform to the compact space and aesthetic requirements. Embedded, on-wall and on-glass BSs are introduced to address the problem and correspondingly, material-integrated antenna and TAs are introduced. Thus, four objectives are proposed: 1. propose a method of designing material-integrated antennas; 2. propose TAs with comparable performance to traditional antennas; 3. optimise the efficiency and gain of TA using TCF; 4. establish a theory for ADTL antenna.

In Chapter 2, the current research on material-integrated antennas, TAs and transparent metasurfaces are reviewed. Firstly, two kinds of material-integrated antennas include embedded antennas and glass-integrated antennas are introduced. Embedded antennas usually have

strong hiding ability, but they have the following defects: 1. they may affect the stability of the building structures; 2. it is not easy to install and repair the embedded devices; 3. the EM characteristics of the embedded antennas are easily affected by the age of the buried materials. The glass-integrated metal antennas degrade the transparency and may affect the normal use of the glass. Secondly, the properties of TCFs and MM materials are analysed and the TAs are reviewed. The TAs using TCFs commonly show high transparency and good visualisation effect, but very low gains and low efficiencies. As a comparison, MM sacrifices the visualisation effect to improve efficiency. Thirdly, transparent metasurfaces are reviewed. The transparent metasurfaces using TCFs are suitable for indoor applications but also face gain and efficiency challenges. The all-dielectric metasurface is potential, but the dielectric transparent materials have not been attempted. Additionally, there are few theories available for all-dielectric metasurface. This chapter summarises the current representative TAs, paving the way for indoor friendly TAs' development.

In Chapters 3, 4 and 5, six original works are proposed. 1. Glass-integrated antenna based on large mesh-grid structure provides GSM, WLAN and 5G band service for indoor applications. Based on CMA, the antenna achieves triple-band resonance with thin wires. 2. CPW-fed TAA using wired MM that developed from mesh-grid structure has excellent performance on gain and efficiency. However, it has a high cost to spray metal straight onto glass surfaces. 3. The first UWB MIMO TA with meshed FR-4 substrate and wired MM structure is developed. It gains advantages against other types of TAs and achieves comparable performance to the conventional metal antennas while remaining a high transparency. The first effective decoupling structure for the MM is applied. Current and electric field analysis is applied to determine the mesh density and size, and then the transparency and the efficiency performance are balanced. 4. The UWB MIMO TA using ITO demonstrates the gain and efficiency of ITO antennas in conventional. 5. Without changing the material, the ITO TA using FPC achieves a breakthrough the gain and efficiency. It demonstrates that the potential of the antenna shape and implementation is very important. 6. The ADTLs are the first transparent lens for wireless communication. They realise the beamforming functions with low efficiency reduction and improved gain. By changing the material of the antenna,

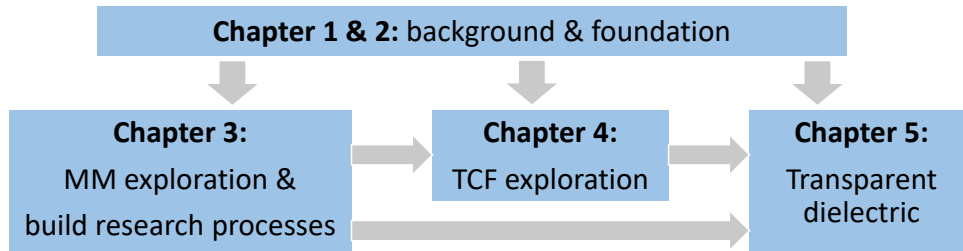


Fig. 6.1 The relationship between the chapters.

various forms of TAs are obtained. The functions such as multiband, UWB, MIMO, gain and efficiency enhanced and beamforming are realised. Furthermore, prototype fabrications and measurements bridge the gap between theory and practice.

Fig. 6.1 illustrates the relationship between the chapters. Chapters 1 and 2 are the background and supporting research of the whole thesis. Chapter 3 explores MM TAs from simple to complex. Following the research processes established in Chapter 3, Chapters 4 and 5 further develops TAs by changing materials and mathematics methods.

In general, the thesis:

- discusses the advantages and disadvantages of various TAs;
- proposes solutions to the defects;
- further completes the TA research and verifies the feasibility of TA applications;
- and leaving reference implementation methods for various types of TAs.

The arrival of the smart era is the general trend, and communication equipment such as antennas have an irreplaceable position. The perfections of TA contributed by the thesis are promoting the applications of smart devices and thus affecting the process of the smart era.

## 6.2 Future Work

This thesis comprehensively discusses the TA from the aspect of device design and provides TA options with different performances and transparency. However, to promote the TA applications, the researches on indoor beamforming, more transparent device design, antenna

performance and transparency balance and application scenarios combination have not been discussed. The future work can be described as follows.

### **1). Indoor beamforming using TA:**

Using indoor beamforming technology can accurately and efficiently deliver information to users. Precise delivery can improve information security and reduce power consumption. The proposed FPC TA and ADTLs have beam adjustment capabilities. How to realise the beamforming function of single or multiple TA and TA arrays should be explored. Then designing more devices for indoor communications will not stop. Furthermore, research on TA with dynamically adjustable gain and polarisation direction should also be taken into consideration.

### **2). Design RIS using transparent material:**

RIS can make the beam more flexible and controllable and have low power consumption in short-distance communication. It is promising for the indoor environment. However, the real-time application is also facing space limitations. Designing and fabricating transparent RIS devices can promote the applications.

### **3). TA performance balance:**

Different application environments have different requirements for antenna functions, exterior and transparency. More transparent materials are worth to attempt. The suitable method for different materials can be explored. It is important to propose a reference model of transparency and performance for selection among the various materials.

### **4). TA deployment:**

The purpose of indoor TAs is to integrate with structures to hide, so most TAs will not stand alone in the air. However, different installation methods, materials and building structures attached will have different effects on the TA. There may be a completely different radiation effect of the TA attached to the surface with or without the gap. Power consumption is an important factor affecting the construction of small BSs. Based on the indoor layout, the properties of building materials and TA performance, the TA location should be calculated. The algorithm of the deployment that meets coverage requirements and consumes minimum power should be explored.

The study of a single antenna has limitations. A small improvement on a single device is not enough to drive the development of the industry because it may be replaced by other devices at any time. Future work should pay more attention to method research, so as to benefit multiple TAs and even have an impact on the antenna research and development industry.



# Appendix A

## Matlab Code for CMA

### A.1 Main Function of Sweeping Modes for Specific Band

```
clear all WireLength = 0.08;
    WireRadius = 0.001;
    NumGauss = 5;
    TotalSegments = 60;
    ExcitationType = 1;
    ThetaIn = pi;
    NumTheta = 300;
    Modes=zeros(TotalSegments-1);
    Frequency = 0.9e9;
    for b = 1:74
        Frequency=Frequency+1e8;
        [Zin, Current, ERadiated, A] = ATWStraightWireTriangle(TotalSegments, NumGauss,
WireLength, WireRadius, Frequency, ExcitationType, ThetaIn, NumTheta);
        Z = A;
        [lambda,Jb,R,X,MS]= CM(Z,TotalSegments);
        Jb = Normalise(Jb,TotalSegments,R);
        [Track]=Tracking(TotalSegments,Modes,Jb,ranklambda,lambda,MS);
```

```

for j = 1:5
[row, col(j)]=find(j==Track(1,1:5));
[ev(j,b)]=Track(4,col(j));
[ms(j,b)]=Track(5,col(j));
end
end Hz=linspace(1,8.4,b);
plot(Hz,ms(1,:));hold on;
plot(Hz,ms(2,:));hold on;
plot(Hz,ms(3,:));hold on;
plot(Hz,ms(4,:));hold on;
plot(Hz,ms(5,:));hold on;
xlabel('Frequency(GHz)');
ylabel('Modes Significance');
legend('Mode 1','Mode 2','Mode 3','Mode 4','Mode 5','Mode 6');
save('Modes.mat','Modes');

```

## A.2 Function ATWStraightWireTriangle For MoM Using Triangle Function

```

function [Zin, Current, ERadiated, A] = ATWStraightWireTriangle(TotalSegments, Num-
Gauss, WireLength, ... WireRadius, Frequency, ExcitationType, ThetaIn, NumTheta)
c = 299792458;
Mu = 4.0e-7*pi;
Epsilon = 1.0/(Mu*c*c);
w = 2.0*pi*Frequency;
k = w*sqrt(Mu*Epsilon);
Eta = sqrt(Mu/Epsilon);
TotalElements = TotalSegments - 1;
DeltaX = WireLength/TotalSegments;

```

```

for i x = 1:TotalSegments
x(i x) = (i x - 0.5)*DeltaX - WireLength/2;
end
[GaussX, GaussW] = lgwt(NumGauss, 0.0, 1);
GaussX = GaussX*DeltaX;
GaussW = GaussW*DeltaX;
tri(1,:) = (GaussX)/DeltaX;
tri(2,:) = (DeltaX - GaussX)/DeltaX;
nds = 20;
ds = DeltaX/nds;
sx = linspace(0.5*ds, DeltaX - 0.5*ds, nds);
tris(1,:) = sx/DeltaX;
tris(2,:) = (DeltaX - sx)/DeltaX;
A = zeros(TotalElements);
m tri = 1;
ms(1) = m tri; ms(2) = m tri + 1; xms(1) = x(ms(1)) - 0.5*DeltaX; xms(2) = x(ms(2)) -
0.5*DeltaX;
for n tri = m tri:TotalElements
ns(1) = n tri; ns(2) = n tri + 1; xns(1) = x(ns(1)) - 0.5*DeltaX; xns(2) = x(ns(2)) -
0.5*DeltaX;
for im = 1:2
xm = xms(im) + GaussX;
if im == 1 sm = 1.0; else sm = -1.0; end
for in=1:2
xn = xns(in) + GaussX;
if in == 1 sn = 1.0; else sn = -1.0; end
if ms(im) == ns(in)
for i gm = 1:nds
[s1, s2] = ATWTriangleAnalyticTerms(sx(i gm), DeltaX, WireRadius, k);

```

```

if (im == 1 & in == 1) | (im == 2 & in == 2)
A(m tri,n tri) = A(m tri,n tri) + k*k*ds*tris(1,i gm)*s1 - sm*sn*ds*s2;
else
A(m tri,n tri) = A(m tri,n tri) + k*k*ds*tris(2,i gm)*s1 - sm*sn*ds*s2;
end
end
else
sv = 0.0;
ss = 0.0;
for i gm = 1:NumGauss
for i gn = 1:NumGauss
r = sqrt((xm(i gm) - xn(i gn))^2 + WireRadius^2);
expterm = exp(-i*k*r)/r;
sv = sv + GaussW(i gm)*GaussW(i gn)*tri(im,i gm)*tri(in,i gn)*expterm;
ss = ss + GaussW(i gm)*GaussW(i gn)*expterm/DeltaX/DeltaX;
end
end A(m tri,n tri) = A(m tri,n tri) + k*k*sv - sm*sn*ss;
end
end
end
end
A = toeplitz(real(A(1,:))) + i*toeplitz(imag(A(1,:)));
A = A/4/pi*1i/w/Epsilon;
mids = floor(TotalSegments/2) + 1;
rhs = zeros(TotalElements,1);
for m tri = 1:TotalElements
ms(1) = m tri;
ms(2) = m tri + 1;
xms(1) = x(ms(1)) - 0.5*DeltaX;

```

```

xms(2) = x(ms(2)) - 0.5*DeltaX;
for im=1:2
if ExcitationType == 0
if ms(im) == mids
for i gm = 1:NumGauss
rhs(m tri) = rhs(m tri) - GaussW(i gm)*tri(im,i gm)*(1.0/DeltaX);
end
end
elseif ExcitationType == 1
rhs(m tri) = rhs(m tri) - quad(@TriangleFrill, 0, DeltaX, [], [], xms(im), k, WireRadius,
DeltaX, im);
elseif ExcitationType == 2
rhs(m tri) = rhs(m tri) - quad(@TrianglePlaneWave, 0, DeltaX, [], [], xms(im), k, WireRa-
dius, DeltaX, im, ThetaIn);
end
end
end
Ainv = inv(A);
b = Ainv*rhs;
theta = linspace(0.0, 2.0*pi, NumTheta);
for iTheta = 1:NumTheta
costheta = cos(theta(iTheta));
sintheta = sin(theta(iTheta));
ERadiated(iTheta) = 0.0;
for m tri = 1:TotalElements
ms(1) = m tri;
ms(2) = m tri + 1;
xms(1) = x(ms(1)) - 0.5*DeltaX;
xms(2) = x(ms(2)) - 0.5*DeltaX;

```

```

for im=1:2
xm = xms(im) + GaussX;
for i gm = 1:NumGauss
ERadiated(iTheta) = ERadiated(iTheta) + GaussW(i gm)*tri(im,i gm)*b(m tri)*sintheta*exp(i*k*xm(i
gm)*costheta);
end
end
end
ERadiated(iTheta) = -(i*w*Mu/(4.0*pi))*ERadiated(iTheta);
end
Zin = 1.0 / (0.5*(b(mids) + b(mids+1)));
Current = zeros(TotalSegments,1);
for j=1:TotalSegments
if j == 1
Current(j) = 0.5*b(j);
elseif j == TotalSegments
Current(j) = 0.5*b(TotalSegments - 1);
else
Current(j) = 0.5*(b(j-1) + b(j));
end
end
return
function [s1, s2] = ATWTriangleAnalyticTerms(x, DeltaX, a, k)
num = x + sqrt(a2 + x2);
denom = x - DeltaX + sqrt(a2 + (x - DeltaX)2);
logterm = log(num/denom);
s1 = (1/DeltaX)*sqrt(a2 + (x - DeltaX)2) - (1/DeltaX)*sqrt(a2 + x2) + (x/DeltaX)*logterm
- i*k*DeltaX/2;
s2 = (1/DeltaX/DeltaX)*(logterm - i*k*DeltaX);

```

```

return;

function [e z] = TriangleFrill(z, z s, k, a, delta z, tri)

z1 = z + z s;
b = 3.0*a;
z2 = z1.*z1;
r1 = sqrt(z2 + a*a);
r2 = sqrt(z2 + b*b);
e z = 1.0/(2.0*log(b/a)).*(exp(-i*k*r1)/r1 - exp(-i*k*r2)/r2);

if tri == 1
t = z/delta z;
else
t = (delta z - z)/delta z;
end
e z = e z.*t;

return;

function [e z] = TrianglePlaneWave(z, z s, k, a, delta z, tri, theta)

z1 = z + z s;
e z = sin(theta)*exp(i*k*z*cos(theta));

if tri == 1
t = z/delta z;
else
t = (delta z - z)/delta z;
end
e z = e z.*t;

return;

```

### A.3 Function CM for Characteristic Mode Algorithm

```
function [lambda,J,R,X,MS] = CM(Z,TotalSegments)
```

```

R = (Z+conj(Z))/2;
X = (Z-conj(Z))/2/i;
[J,lamb] = eig(X,R);
t = zeros(TotalSegments-1);
for q = 1:TotalSegments-1
t(1,q) = lamb(q,q);
end
lambda = t(1,:);
for r = 1:TotalSegments-1
MS(r)=abs(1/(1+i*lambda(r)));
end

```

## A.4 Function Normalise For Modes Normalisation

```

function [NJ] = Normalise(J,TotalSegments,R)
c = zeros(1,TotalSegments-1);
NJ = zeros(TotalSegments-1,TotalSegments-1);
for k = 1:TotalSegments-1
c(1,k) = abs(J(:,k)'R*J(:,k));
NJ(:,k) = J(:,k)/sqrt(c(1,k));
end
end

```

## A.5 Function Tracking For Mode Tracking

```

function [Track]=Tracking(TotalSegments,J1,J2,lambda1,lambda,MS)
N = TotalSegments-1;
N1=size(J1);
N2=size(J2);

```

```

p1=0; p2=0; p3=0; p4=0; p5=0; p6=0; p7=0;
for i = 1:N1(1,2)
for j = 1:N2(1,2)
for k = 1:N
p1 = p1+N*J1(k,i)*J2(k,j);
p2 = p2+J1(k,i);
p3 = p3+J2(k,j);
p4 = p4+N*J1(k,i)*J1(k,i);
p5 = p2*p2;
p6 = p6+N*J2(k,j)*J2(k,j);
p7 = p3*p3;
end
p(i,j) = (p1-p2*p3)/(sqrt(p4-p5)*sqrt(p6-p7));
c(i,j) = abs(p(i,j));
p1=0; p2=0; p3=0; p4=0; p5=0; p6=0; p7=0;
end
end
c1 = c;
for a = 1:N1(1,2)
M=max(max(c));
[row,col]=findlocation(M,c);
Track(1,a)=row;
Track(2,a)=lambda1(row);
Track(3,a)=col;
Track(4,a)=lambda(col);
Track(5,a)=MS(col);
c(row,:)=0;
c(:,col)=0;
end

```

```
function[row, col] = findlocation(M,c)
[ row,col]=find(M==c);
row = row(1,1);
col = col(1,1);
end
end
```

# References

- [1] J. Zhang, A. A. Glazunov, Y. Wang *et al.*, “Fundamental wireless performance of a building,” *IEEE Wireless Commun.*, vol. 29, no. 1, pp. 186–193, Feb. 2022.
- [2] M. Nemati, B. Maham, S. R. Pokhrel *et al.*, “Modeling RIS empowered outdoor-to-indoor communication in mmWave cellular networks,” *IEEE Trans. Commun.*, vol. 69, no. 11, pp. 7837–7850, Aug. 2021.
- [3] A. J. A. Al-Gburi, Z. Zakaria, H. Alsariera *et al.*, “Broadband circular polarised printed antennas for indoor wireless communication systems: A comprehensive review,” *Micromachines*, vol. 13, no. 7, p. 1048, Jun. 2022.
- [4] K. He, S.-X. Gong, and D. Guo, “Broadband omnidirectional distributed antenna for indoor wireless communication systems,” *Electron. Lett.*, vol. 52, no. 16, pp. 1361–1362, Aug. 2016.
- [5] L. Yu, J. Song, Y. Gao *et al.*, “Low-profile dual-polarized omnidirectional antenna for broadband indoor distributed antenna system,” *Prog. Electromagn. Res. Lett.*, vol. 67, pp. 39–45, 2017.
- [6] X. W. Dai, S. W. Mao, and T. Zhou, “Broadband circular patch antenna with monopolar radiation pattern for indoor wireless communication,” *Int. J. Microw. Wirel. Technol.*, vol. 9, no. 4, pp. 953–958, May 2017.
- [7] H. H. Tran and I. Park, “A dual-wideband circularly polarized antenna using an artificial magnetic conductor,” *IEEE Antennas Wirel. Propag. Lett.*, vol. 15, pp. 950–953, Oct. 2015.

- [8] G. Feng, L. Chen, X. Wang *et al.*, “Broadband circularly polarized crossed bowtie dipole antenna loaded with parasitic elements,” *IEEE Antennas Wirel. Propag. Lett.*, vol. 17, no. 1, pp. 114–117, Nov. 2017.
- [9] R. K. Saini and S. Dwari, “CPW-fed broadband circularly polarized rectangular slot antenna with L-shaped feed line and parasitic elements,” *Microw. Opt. Technol. Lett.*, vol. 57, no. 8, pp. 1788–1794, Aug. 2015.
- [10] K. M. Shams and M. Ali, “Wireless power transmission to a buried sensor in concrete,” *IEEE Sens. J.*, vol. 7, no. 12, pp. 1573–1577, Oct. 2007.
- [11] G. Mauro, G. Castorina, A. Morabito *et al.*, “Effects of lossy background and rebars on antennas embedded in concrete structures,” *Microwave Opt. Technol. Lett.*, vol. 58, no. 11, pp. 2653–2656, Nov. 2016.
- [12] M. F. Rad and L. Shafai, “Embedded microstrip patch antenna for structural health monitoring applications,” in *2008 IEEE Antennas and Propagation Society International Symposium (ISAP)*, Jun. 2008, pp. 1–4.
- [13] P. Soontornpipit, C. M. Furse, Y. C. Chung *et al.*, “Optimization of a buried microstrip antenna for simultaneous communication and sensing of soil moisture,” *IEEE Trans. Antennas Propag.*, vol. 54, no. 3, pp. 797–800, Mar. 2006.
- [14] S. Yuan, X. Lai, X. Zhao *et al.*, “Distributed structural health monitoring system based on smart wireless sensor and multi-agent technology,” *Smart Mater. Struct.*, vol. 15, no. 1, p. 1, Dec. 2005.
- [15] J. Lynch, “Overview of wireless sensors for real-time health monitoring of civil structures,” in *Proceedings of the 4th International Workshop on Structural Control*, Jun. 2004, pp. 189–194.
- [16] G. Artner, W. Kotterman, G. Del Galdo *et al.*, “Automotive antenna roof for cooperative connected driving,” *IEEE Access*, vol. 7, pp. 20 083–20 090, Feb. 2019.

- [17] W. Kang and H. Choo, "Design of vertical lines for vehicle rear window antennas," *Microwave Opt. Technol. Lett.*, vol. 52, no. 6, pp. 1445–1449, Jun. 2010.
- [18] F. G. Bogdanov, D. D. Karkashadze, R. G. Jobava *et al.*, "Validation of hybrid mom scheme with included equivalent glass antenna model for handling automotive emc problems," *IEEE Trans. Electromagn. Compat.*, vol. 52, no. 1, pp. 164–172, Jan. 2010.
- [19] G. Byun, Y. Noh, I. Park *et al.*, "Design of rear glass-integrated antennas with vertical line optimization for FM radio reception," *Int. J. Automot. Technol.*, vol. 16, no. 4, pp. 629–634, Aug. 2015.
- [20] S. Ahn and H. Choo, "A systematic design method of on-glass antennas using mesh-grid structures," *IEEE Trans. Veh. Technol.*, vol. 59, no. 7, pp. 3286–3293, Sep. 2010.
- [21] D. Jang, N. K. Kong, and H. Choo, "Design of an on-glass 5G monopole antenna for a vehicle window glass," *IEEE Access*, vol. 9, pp. 152 749–152 755, Nov. 2021.
- [22] S. Hong, S. H. Kang, Y. Kim *et al.*, "Transparent and flexible antenna for wearable glasses applications," *IEEE Trans. Antennas Propag.*, vol. 64, no. 7, pp. 2797–2804, Jul. 2016.
- [23] E. Cil and S. Dumanli, "The design of a reconfigurable slot antenna printed on glass for wearable applications," *IEEE Access*, vol. 8, pp. 95 417–95 423, May 2020.
- [24] D. S. Hecht, L. Hu, and G. Irvin, "Emerging transparent electrodes based on thin films of carbon nanotubes, graphene, and metallic nanostructures," *Adv. Mater.*, vol. 23, no. 13, pp. 1482–1513, Apr. 2011.
- [25] R. B. Green, M. Guzman, N. Izyumskaya *et al.*, "Optically transparent antennas and filters: A smart city concept to alleviate infrastructure and network capacity challenges," *IEEE Antennas Propag. Mag.*, vol. 61, no. 3, pp. 37–47, Apr. 2019.
- [26] Z. J. Silva, C. R. Valenta, and G. D. Durgin, "Optically transparent antennas: A survey of transparent microwave conductor performance and applications," *IEEE Antennas Propag. Mag.*, vol. 63, no. 1, pp. 27–39, May 2020.

- [27] Y. Lin, T. Chen, L. Wang *et al.*, “Comparison of AZO, GZO, and AGZO thin films TCOs applied for a-Si solar cells,” *J. Electrochem. Soc.*, vol. 159, no. 6, p. H599, Apr. 2012.
- [28] H. J. Song, T. Y. Hsu, D. F. Sievenpiper *et al.*, “A method for improving the efficiency of transparent film antennas,” *IEEE Antennas Wirel. Propag. Lett.*, vol. 7, pp. 753–756, Oct. 2008.
- [29] M. Rani, S. K. A. Rahim, M. R. Kamarudin *et al.*, “Electromagnetic behaviors of thin film CPW-fed CSRR loaded on UWB transparent antenna,” *IEEE Antennas Wirel. Propag. Lett.*, vol. 13, pp. 1239–1242, Jun. 2014.
- [30] M. Malek, S. Hakimi, S. A. Rahim *et al.*, “Dual-band CPW-fed transparent antenna for active RFID tags,” *IEEE Antennas Wirel. Propag. Lett.*, vol. 14, pp. 919–922, Dec. 2014.
- [31] O. Tuna, Y. Selamet, G. Aygun *et al.*, “High quality ITO thin films grown by DC and RF sputtering without oxygen,” *J. Phys. D: Appl. Phys.*, vol. 43, no. 5, p. 055402, Jan. 2010.
- [32] USGS, “Minerals information: Indium,” Accessed on: Nov. 1, 2022. [Online]. Available: <https://minerals.usgs.gov/minerals/pubs/commodity/indium/index.html>.
- [33] R. B. Green, M. Toporkov, M. Ullah *et al.*, “An alternative material for transparent antennas for commercial and medical applications,” *Microwave Opt. Technol. Lett.*, vol. 59, no. 4, pp. 773–777, Apr. 2017.
- [34] M. Zamudio, M. Behzadirad, C. Christodoulou *et al.*, “Optimization of AZO films for integrating optically transparent antennas with photovoltaics,” *Appl. Phys. Lett.*, vol. 110, no. 23, p. 234101, Jun. 2017.
- [35] R. Kainikkara Vatakketath, “Investigation of the transparent conducting oxide (TCO) material used in CIGS thin film solar cell in midsummer AB,” Master dissertation, Dept. Elect. Eng., Uppsala Univ., Uppsala, 2020.

- [36] D. M. Pozar, *Microwave engineering*. John Wiley & sons, 2011.
- [37] F. Feldmann, K.-U. Ritzau, M. Bivour *et al.*, “High and low work function materials for passivated contacts,” *Energy Procedia*, vol. 77, pp. 263–270, Aug. 2015.
- [38] H. Hosono, H. Ohta, M. Orita *et al.*, “Frontier of transparent conductive oxide thin films,” *Vacuum*, vol. 66, no. 3-4, pp. 419–425, Aug. 2002.
- [39] J.-L. Wu, H.-Y. Lin, Y.-C. Chen *et al.*, “Effects of ZnO buffer layer on characteristics of ZnO: Ga films grown on flexible substrates: Investigation of surface energy, electrical, optical, and structural properties,” *ECS J. Solid State Sci. Technol.*, vol. 2, no. 4, p. P115, Jan. 2013.
- [40] A. Desai, M. Palandoken, J. Kulkarni *et al.*, “Wideband flexible/transparent connected-ground MIMO antennas for sub-6 GHz 5G and WLAN applications,” *IEEE Access*, vol. 9, pp. 147 003–147 015, Oct. 2021.
- [41] D. Potti, Y. Tusharika, M. G. N. Alsath *et al.*, “A novel optically transparent UWB antenna for automotive MIMO communications,” *IEEE Trans. Antennas Propag.*, Jan. 2021.
- [42] H. J. Song, C. R. White, and E. Yasan, “Challenges in glass integrated optically transparent antennas,” in *2011 International Symposium on Antennas and Propagation (ISAP)*, Oct. 2011.
- [43] T.-H. Chang, C.-S. Hsu, C. Wang *et al.*, “Onboard measurement and warning module for irregular vehicle behavior,” *IEEE Trans. Intell. Transp. Syst.*, vol. 9, no. 3, pp. 501–513, Aug. 2008.
- [44] S. Zarbakhsh, M. Akbari, M. Farahani *et al.*, “Optically transparent subarray antenna based on solar panel for Cubesat application,” *IEEE Trans. Antennas Propag.*, vol. 68, no. 1, pp. 319–328, Jan. 2020.

- [45] N. A. Eltresy, M. Abd Elhamid, D. M. Elsheakh *et al.*, “Silver sandwiched ITO based transparent antenna array for RF energy harvesting in 5G mid-range of frequencies,” *IEEE Access*, vol. 9, pp. 49 476–49 486, Sep. 2021.
- [46] S. Sheikh, M. Shokooh-Saremi, and M.-M. Bagheri-Mohagheghi, “Transparent microstrip antenna made of fluorine doped tin oxide: a comprehensive study,” *J. Electromagn. Waves Appl.*, vol. 29, no. 12, pp. 1557–1569, Aug. 2015.
- [47] C.-T. Wu, Y.-R. Ho, D.-Z. Huang *et al.*, “AZO/silver nanowire stacked films deposited by RF magnetron sputtering for transparent antenna,” *Surf. Coat. Technol.*, vol. 360, pp. 95–102, Feb. 2019.
- [48] M. R. Haraty, M. Naser-Moghadasi, A. A. Lotfi-Neyestanak *et al.*, “Improving the efficiency of transparent antenna using gold nanolayer deposition,” *IEEE Antennas Wirel. Propag. Lett.*, vol. 15, pp. 4–7, Apr. 2015.
- [49] A. Rashidian, L. Shafai, and C. Shafai, “Miniaturized transparent metallodielectric resonator antennas integrated with amorphous silicon solar cells,” *IEEE Trans. Antennas Propag.*, vol. 65, no. 5, pp. 2265–2275, Mar. 2017.
- [50] H. Sharifi, H. J. Song, M. Yajima *et al.*, “Semi-transparent and conformal antenna technology for millimeter-wave intelligent sensing,” in *2018 IEEE MTT-S International Conference on Microwaves for Intelligent Mobility (ICMIM)*, Apr. 2018, pp. 1–4.
- [51] P.-C. Yu, C.-C. Hong, and T.-M. Liou, “Bendable transparent conductive meshes based on multi-layer inkjet-printed silver patterns,” *J. Micromech. Microeng.*, vol. 26, no. 3, p. 035012, Feb. 2016.
- [52] J. Park, S. Y. Lee, J. Kim *et al.*, “An optically invisible antenna-on-display concept for millimeter-wave 5G cellular devices,” *IEEE Trans. Antennas Propag.*, vol. 67, no. 5, pp. 2942–2952, Feb. 2019.

- [53] H. Qiu, H. Liu, X. Jia *et al.*, “Compact, flexible, and transparent antennas based on embedded metallic mesh for wearable devices in 5G wireless network,” *IEEE Trans. Antennas Propag.*, vol. 69, no. 4, pp. 1864–1873, Nov. 2021.
- [54] Q. Li, S. Cheung, D. Wu *et al.*, “Optically transparent dual-band MIMO antenna using micro-metal mesh conductive film for WLAN system,” *IEEE Antennas Wirel. Propag. Lett.*, vol. 16, pp. 920–923, Sep. 2016.
- [55] J. L. Kubwimana, N. J. Kirsch *et al.*, “Dual-polarized 5.75 GHz optically transparent antenna arrays,” *IEEE Antennas Wirel. Propag. Lett.*, vol. 18, no. 7, pp. 1512–1516, Jul. 2019.
- [56] A. Martin, O. Lafond, M. Himdi *et al.*, “Improvement of 60 GHz transparent patch antenna array performance through specific double-sided micrometric mesh metal technology,” *IEEE Access*, vol. 7, pp. 2256–2262, Dec. 2018.
- [57] X. Liu, D. R. Jackson, J. Chen *et al.*, “Transparent and nontransparent microstrip antennas on a Cubesat: Novel low-profile antennas for Cubesats improve mission reliability,” *IEEE Antennas Propag. Mag.*, vol. 59, no. 2, pp. 59–68, Apr. 2017.
- [58] T. Yasin, R. Baktur, T. Turpin *et al.*, “Analysis and design of highly transparent meshed patch antenna backed by a solid ground plane,” *Prog. Electromagn. Res. M*, vol. 56, pp. 133–144, May 2017.
- [59] B. Xi, X. Liang, Q. Chen *et al.*, “Optical transparent antenna array integrated with solar cell,” *IEEE Antennas Wirel. Propag. Lett.*, vol. 19, no. 3, pp. 457–461, Jan. 2020.
- [60] T. W. Turpin and R. Baktur, “Meshed patch antennas integrated on solar cells,” *IEEE Antennas Wirel. Propag. Lett.*, vol. 8, pp. 693–696, Jun. 2009.
- [61] T. Yasin and R. Baktur, “Circularly polarized meshed patch antenna for small satellite application,” *IEEE Antennas Wirel. Propag. Lett.*, vol. 12, pp. 1057–1060, Aug. 2013.

- [62] Y.-X. Sun, D. Wu, X. S. Fang *et al.*, “On-glass grid structure and its application in highly-transparent antenna for internet of vehicles,” *IEEE Trans. Veh. Technol.*, Sep. 2022.
- [63] N. Neveu, M. Garcia, J. Casana *et al.*, “Transparent microstrip antennas for CubeSat applications,” in *IEEE International Conference on Wireless for Space and Extreme Environments*, Nov. 2013, pp. 1–4.
- [64] R. Yazdani, M. Yousefi, H. Aliakbarian *et al.*, “Miniaturized triple-band highly transparent antenna,” *IEEE Trans. Antennas Propag.*, vol. 68, no. 2, pp. 712–718, Feb. 2020.
- [65] S. Hakimi, S. K. A. Rahim, M. Abedian *et al.*, “CPW-fed transparent antenna for extended ultrawideband applications,” *IEEE Antennas Wirel. Propag. Lett.*, vol. 13, pp. 1251–1254, Jun. 2014.
- [66] T. Peter, T. Abd Rahman, S. Cheung *et al.*, “A novel transparent UWB antenna for photovoltaic solar panel integration and RF energy harvesting,” *IEEE Trans. Antennas Propag.*, vol. 62, no. 4, pp. 1844–1853, Apr. 2014.
- [67] S. Hong, Y. Kim, and C. W. Jung, “Transparent microstrip patch antennas with multilayer and metal-mesh films,” *IEEE Antennas Wirel. Propag. Lett.*, vol. 16, pp. 772–775, Aug. 2016.
- [68] M. Roo-Ons, S. Shynu, M. Ammann *et al.*, “Transparent patch antenna on a-Si thin-film glass solar module,” *Electron. Lett.*, vol. 47, no. 2, pp. 85–86, Jan. 2011.
- [69] T. Peter, R. Nilavalan, H. F. AbuTarboush *et al.*, “A novel technique and soldering method to improve performance of transparent polymer antennas,” *IEEE Antennas Wirel. Propag. Lett.*, vol. 9, pp. 918–921, Sep. 2010.
- [70] T. Peter, T. Yuk, R. Nilavalan *et al.*, “A novel technique to improve gain in transparent UWB antennas,” in *2011 Loughborough Antennas and Propagation Conference*, Nov. 2011, pp. 1–4.

- [71] K. K. So, B.-J. Chen, and C. H. Chan, "Microwave and millimeter-wave MIMO antenna using conductive ITO film," *IEEE Access*, vol. 8, pp. 207 024–207 033, Nov. 2020.
- [72] N. Jizat, S. Rahim, Y. Lo, and M. Mansor, "Compact size of CPW dual-band meanderline transparent antenna for WLAN applications," in *2014 IEEE Asia-Pacific Conference on Applied Electromagnetics (APACE)*, Dec. 2014, pp. 20–22.
- [73] Y. Yao, W. Chen, X. Chen *et al.*, "Design of optically transparent antenna with directional radiation patterns," *Int. J. Antennas Propag.*, vol. 2017, Aug. 2017.
- [74] G. Sun, B. Muneer, and Q. Zhu, "A study of microstrip antenna made of transparent ITO films," in *2014 IEEE Antennas and Propagation Society International Symposium (APSURSI)*. IEEE, Jul. 2014, pp. 1867–1868.
- [75] A. Desai, C. D. Bui, J. Patel *et al.*, "Compact wideband four element optically transparent MIMO antenna for mm-wave 5G applications," *IEEE Access*, vol. 8, pp. 194 206–194 217, Oct. 2020.
- [76] S. H. Kang and C. W. Jung, "Transparent patch antenna using metal mesh," *IEEE Trans. Antennas Propag.*, vol. 66, no. 4, pp. 2095–2100, Apr. 2018.
- [77] W. Hong, S. Lim, S. Ko *et al.*, "Optically invisible antenna integrated within an OLED touch display panel for IoT applications," *IEEE Trans. Antennas Propag.*, vol. 65, no. 7, pp. 3750–3755, May 2017.
- [78] M. Kim, D. Lee, Y. Oh *et al.*, "Antenna-on-display concept on an extremely thin substrate for sub-6 GHz wireless applications," *IEEE Trans. Antennas Propag.*, vol. 70, no. 7, pp. 5929–5934, Mar. 2022.
- [79] J. Hautcoeur, L. Talbi, and K. Hettak, "Feasibility study of optically transparent CPW-fed monopole antenna at 60-GHz ISM bands," *IEEE Trans. Antennas Propag.*, vol. 61, no. 4, pp. 1651–1657, Dec. 2012.

- [80] M. M. Rabie, H. El-Henawy, F. El-Hefnawy *et al.*, “Meshed conductor and meshed substrate GPS L1 band microstrip antenna for Cubesat applications,” in *Natl. Radio Sci. Conf. Proc.*, Mar. 2018, pp. 55–62.
- [81] Q. Dao, T. Cherogony, and B. Geck, “Optically transparent and circularly polarized patch antenna for K-band applications,” in *2016 German Microwave Conference (GeMiC)*, Mar. 2016, pp. 247–250.
- [82] J. Wang, Y. Li, Z. H. Jiang *et al.*, “Metantenna: When metasurface meets antenna again,” *IEEE Trans. Antennas Propag.*, vol. 68, no. 3, pp. 1332–1347, Mar. 2020.
- [83] C. L. Holloway, E. F. Kuester, J. A. Gordon *et al.*, “An overview of the theory and applications of metasurfaces: The two-dimensional equivalents of metamaterials,” *IEEE Antennas Propag. Mag.*, vol. 54, no. 2, pp. 10–35, Apr. 2012.
- [84] Y. Pan, P. Hu, X. Zhang *et al.*, “A low-profile high-gain and wideband filtering antenna with metasurface,” *IEEE Trans. Antennas Propag.*, vol. 64, no. 5, pp. 2010–2016, Feb. 2016.
- [85] F. H. Lin and Z. N. Chen, “Low-profile wideband metasurface antennas using characteristic mode analysis,” *IEEE Trans. Antennas Propag.*, vol. 65, no. 4, pp. 1706–1713, Feb. 2017.
- [86] W. E. Liu, Z. N. Chen, X. Qing *et al.*, “Miniaturized wideband metasurface antennas,” *IEEE Trans. Antennas Propag.*, vol. 65, no. 12, pp. 7345–7349, Oct. 2017.
- [87] W. Zhu, I. D. Rukhlenko, F. Xiao *et al.*, “Multiband coherent perfect absorption in a water-based metasurface,” *Opt. Express*, vol. 25, no. 14, pp. 15 737–15 745, Jul. 2017.
- [88] M. Yan, J. Wang, Y. Pang *et al.*, “An FSS-backed dual-band reflective polarization conversion metasurface,” *IEEE Access*, vol. 7, pp. 104 435–104 442, Jul. 2019.
- [89] X. Liu, J. Gao, L. Xu *et al.*, “A coding diffuse metasurface for RCS reduction,” *IEEE Antennas Wirel. Propag. Lett.*, vol. 16, pp. 724–727, Aug. 2016.

- [90] J. Zhang, W. Jiang, and K. Wei, "A switchable polarisation conversion/in-phase reflection metasurface and its application," *IET Microwaves Antennas Propag.*, vol. 15, no. 13, pp. 1688–1698, Oct. 2021.
- [91] A. H. Naqvi and S. Lim, "A beam-steering antenna with a fluidically programmable metasurface," *IEEE Trans. Antennas Propag.*, vol. 67, no. 6, pp. 3704–3711, Mar. 2019.
- [92] L. Bao, R. Y. Wu, X. Fu *et al.*, "Multi-beam forming and controls by metasurface with phase and amplitude modulations," *IEEE Trans. Antennas Propag.*, vol. 67, no. 10, pp. 6680–6685, Oct. 2019.
- [93] C. Kocia and S. V. Hum, "Design of an optically transparent reflectarray for solar applications using indium tin oxide," *IEEE Trans. Antennas Propag.*, vol. 64, no. 7, pp. 2884–2893, Apr. 2016.
- [94] L. Li, P. Zhang, F. Cheng *et al.*, "An optically transparent near-field focusing metasurface," *IEEE Trans. Microwave Theory Tech.*, vol. 69, no. 4, pp. 2015–2027, Mar. 2021.
- [95] G. Liu, M. R. D. Kodnoeih, K. T. Pham *et al.*, "A millimeter-wave multibeam transparent transmitarray antenna at Ka-band," *IEEE Antennas Wirel. Propag. Lett.*, vol. 18, no. 4, pp. 631–635, Feb. 2019.
- [96] J.-J. Peng, S.-W. Qu, and M. Xia, "Optically transparent reflectarray based on indium tin oxide with improved efficiency," *IEEE Trans. Antennas Propag.*, vol. 68, no. 4, pp. 3289–3294, Apr. 2019.
- [97] R. Orr, G. Goussetis, and V. Fusco, "Design method for circularly polarized Fabry–Perot cavity antennas," *IEEE Trans. Antennas Propag.*, vol. 62, no. 1, pp. 19–26, Oct. 2013.

- [98] N. Wang, Q. Liu, C. Wu *et al.*, “Wideband Fabry-Perot resonator antenna with two complementary FSS layers,” *IEEE Trans. Antennas Propag.*, vol. 62, no. 5, pp. 2463–2471, Feb. 2014.
- [99] S. Kabiri, E. Kornaros, and F. De Flaviis, “Wideband circular polarized Fabry-Perot cavity antennas for V-band indoor point-to-point communications,” *Electromagnetics*, vol. 39, no. 3, pp. 198–216, Apr. 2019.
- [100] Z. M. Razi, P. Rezaei, and A. Valizade, “A novel design of Fabry-Perot antenna using metamaterial superstrate for gain and bandwidth enhancement,” *AEU Int. J. Electron. Commun.*, vol. 69, no. 10, pp. 1525–1532, Oct. 2015.
- [101] F. Qin, S. Gao, G. Wei *et al.*, “Wideband circularly polarized Fabry-Perot antenna [antenna applications corner],” *IEEE Antennas Propag. Mag.*, vol. 57, no. 5, pp. 127–135, Nov. 2015.
- [102] J. Ren, W. Jiang, K. Zhang *et al.*, “A high-gain circularly polarized Fabry-Perot antenna with wideband low-RCS property,” *IEEE Antennas Wirel. Propag. Lett.*, vol. 17, no. 5, pp. 853–856, Mar. 2018.
- [103] T. Akalin, J. Danglot, O. Vanbesien *et al.*, “A highly directive dipole antenna embedded in a Fabry-Perot type cavity,” *IEEE Microwave Wireless Compon. Lett.*, vol. 12, no. 2, pp. 48–50, Aug. 2002.
- [104] N. Hussain, M.-J. Jeong, J. Park *et al.*, “A broadband circularly polarized Fabry-Perot resonant antenna using a single-layered PRS for 5G MIMO applications,” *IEEE Access*, vol. 7, pp. 42 897–42 907, Apr. 2019.
- [105] R. Guzmán-Quirós, A. Weily, J. Gómez-Tornero *et al.*, “A Fabry-Pérot antenna with two-dimensional electronic beam scanning,” *IEEE Trans. Antennas Propag.*, vol. 64, no. 4, pp. 1536–1541, Feb. 2016.

- [106] A. Ghasemi, S. N. Burokur, A. Dhouibi *et al.*, “High beam steering in Fabry–Pérot leaky-wave antennas,” *IEEE Antennas Wirel. Propag. Lett.*, vol. 12, pp. 261–264, Feb. 2013.
- [107] B. Ratni, W. A. Merzouk, A. de Lustrac *et al.*, “Design of phase-modulated metasurfaces for beam steering in Fabry–Perot cavity antennas,” *IEEE Antennas Wirel. Propag. Lett.*, vol. 16, pp. 1401–1404, Dec. 2016.
- [108] X. Liu, L. Peng, Y.-f. Liu *et al.*, “Ultrabroadband all-dielectric transmitarray designing based on genetic algorithm optimization and 3-D print technology,” *IEEE Trans. Antennas Propag.*, vol. 69, no. 4, pp. 2003–2012, Oct. 2020.
- [109] H. Giddens and Y. Hao, “Multibeam graded dielectric lens antenna from multimaterial 3-D printing,” *IEEE Trans. Antennas Propag.*, vol. 68, no. 9, pp. 6832–6837, May 2020.
- [110] F. Wei, J.-W. Hao, L. Xu *et al.*, “A circularly polarized 3-D printed dielectric transmitarray antenna at millimeter-wave band,” *IEEE Antennas Wirel. Propag. Lett.*, vol. 20, no. 7, pp. 1264–1268, May 2021.
- [111] V. M. Pepino, A. F. da Mota, A. Martins *et al.*, “3-D-printed dielectric metasurfaces for antenna gain improvement in the Ka-band,” *IEEE Antennas Wirel. Propag. Lett.*, vol. 17, no. 11, pp. 2133–2136, Jul. 2018.
- [112] M. K. T. Al-Nuaimi, Y. He, and W. Hong, “Design of inhomogeneous all-dielectric electromagnetic-wave diffusive reflectarray metasurface,” *IEEE Antennas Wirel. Propag. Lett.*, vol. 18, no. 4, pp. 732–736, Feb. 2019.
- [113] A. Lalbakhsh, M. U. Afzal, K. P. Esselle *et al.*, “Wideband near-field correction of a Fabry–Perot resonator antenna,” *IEEE Trans. Antennas Propag.*, vol. 67, no. 3, pp. 1975–1980, Jan. 2019.
- [114] A. O. Diallo, R. Czarny, B. Loiseaux *et al.*, “Comparison between a thin lens antenna made of structured dielectric material and conventional lens antennas, in Q-band in a

- compact volume,” *IEEE Antennas Wirel. Propag. Lett.*, vol. 17, no. 2, pp. 307–310, Dec. 2017.
- [115] N. Bhushan, J. Li, D. Malladi *et al.*, “Network densification: the dominant theme for wireless evolution into 5G,” *IEEE Commun. Mag.*, vol. 52, no. 2, pp. 82–89, Feb. 2014.
- [116] Y. Zhang, C. Chen, S. Yang *et al.*, “How friendly are building materials as reflectors to indoor LOS MIMO communications?” *IEEE Internet Things J.*, vol. 7, no. 9, pp. 9116–9127, Sep. 2020.
- [117] Y. Noh, Y. Kim, and H. Ling, “Broadband on-glass antenna with mesh-grid structure for automobiles,” *Electron. Lett.*, vol. 41, no. 21, pp. 1148–1149, Oct. 2005.
- [118] Y. Chen and C.-F. Wang, *Characteristic modes: Theory and applications in antenna engineering*. John Wiley & Sons, Jun. 2015.
- [119] S. Caorsi, D. Moreno, and F. Sidoti, “Theoretical and numerical treatment of surface integrals involving the free-space green’s function,” *IEEE Trans. Antennas Propag.*, vol. 41, no. 9, pp. 1296–1301, Sep. 1993.
- [120] Ş. Karan, “Method of moments analysis of microstrip antennas in cylindrically stratified media using closed-form Green’s functions,” Ph.D. dissertation, bilkent university, 2012.
- [121] S. Rao, D. Wilton, and A. Glisson, “Electromagnetic scattering by surfaces of arbitrary shape,” *IEEE Trans. Antennas Propag.*, vol. 30, no. 3, pp. 409–418, May 1982.
- [122] S. Makarov, “MoM antenna simulations, with matlab: RWG basis functions,” *IEEE Antennas Propag. Mag.*, vol. 43, no. 5, pp. 100–107, Oct. 2001.
- [123] R. Harrington and J. Mautz, “Theory of characteristic modes for conducting bodies,” *IEEE Trans. Antennas Propag.*, vol. 19, no. 5, pp. 622–628, Sep. 1971.

- [124] X.-L. Huang, J. Wu, F. Hu, *et al.*, “Optimal antenna deployment for multiuser MIMO systems based on random matrix theory,” *IEEE Trans. Veh. Technol.*, vol. 65, no. 10, pp. 8155–8162, Dec. 2015.
- [125] P. Borah and T. Bezboruah, “A review on optically transparent antenna,” *Adv. Electr. Electron. Eng.*, vol. 3, no. 5, 2016.
- [126] D. Muirhead, M. A. Imran, and K. Arshad, “Insights and approaches for low-complexity 5G small-cell base-station design for indoor dense networks,” *IEEE Access*, vol. 3, pp. 1562–1572, Aug. 2015.
- [127] G. R. Maccartney, T. S. Rappaport, S. Sun *et al.*, “Indoor office wideband millimeter-wave propagation measurements and channel models at 28 and 73 GHz for ultra-dense 5G wireless networks,” *IEEE Access*, vol. 3, pp. 2388–2424, Oct. 2015.
- [128] Y. Yao, Y. Shao, J. Zhang *et al.*, “Design of glass-integrated grid antenna using CMA for multiband indoor network,” in *2020 IEEE Antennas and Propagation Society International Symposium (ISAP)*, Jan. 2021, pp. 481–482.
- [129] W. Kang, Y. Noh, and H. Choo, “Design of vehicle rear window antenna with mesh-grid structure,” *Electron. Lett.*, vol. 46, no. 22, pp. 1479–1480, Oct. 2010.
- [130] T. Yekan and R. Baktur, “Conformal integrated solar panel antennas: Two effective integration methods of antennas with solar cells,” *IEEE Antennas Propag. Mag.*, vol. 59, no. 2, pp. 69–78, Apr. 2017.
- [131] S. Zhang, Z. Ying, J. Xiong *et al.*, “Ultrawideband MIMO/diversity antennas with a tree-like structure to enhance wideband isolation,” *IEEE Antennas Wirel. Propag. Lett.*, vol. 8, pp. 1279–1282, Nov. 2009.
- [132] J.-M. Lee, K.-B. Kim, H.-K. Ryu *et al.*, “A compact ultrawideband MIMO antenna with WLAN band-rejected operation for mobile devices,” *IEEE Antennas Wirel. Propag. Lett.*, vol. 11, pp. 990–993, Aug. 2012.

- [133] J.-F. Li, Q.-X. Chu, Z.-H. Li *et al.*, “Compact dual band-notched UWB MIMO antenna with high isolation,” *IEEE Trans. Antennas Propag.*, vol. 61, no. 9, pp. 4759–4766, Jun. 2013.
- [134] C.-X. Mao and Q.-X. Chu, “Compact coradiator UWB-MIMO antenna with dual polarization,” *IEEE Trans. Antennas Propag.*, vol. 62, no. 9, pp. 4474–4480, Sep. 2014.
- [135] X. Zhao, S. P. Yeo, and L. C. Ong, “Planar UWB MIMO antenna with pattern diversity and isolation improvement for mobile platform based on the theory of characteristic modes,” *IEEE Trans. Antennas Propag.*, vol. 66, no. 1, pp. 420–425, Jan. 2018.
- [136] D. Gao, Z.-X. Cao, S.-D. Fu *et al.*, “A novel slot-array defected ground structure for decoupling microstrip antenna array,” *IEEE Trans. Antennas Propag.*, vol. 68, no. 10, pp. 7027–7038, Oct. 2020.
- [137] T. Taga, “Analysis for mean effective gain of mobile antennas in land mobile radio environments,” *IEEE Trans. Veh. Technol.*, vol. 39, no. 2, pp. 117–131, May 1990.
- [138] R. Cornelius, A. Narbudowicz, M. J. Ammann *et al.*, “Calculating the envelope correlation coefficient directly from spherical modes spectrum,” in *Proc. EUCAP*, May 2017, pp. 3003–3006.
- [139] R. Tian, B. K. Lau, and Z. Ying, “Multiplexing efficiency of MIMO antennas,” *IEEE Antennas Wirel. Propag. Lett.*, vol. 10, pp. 183–186, 2011.
- [140] M. J. Shehab, I. Kassem, A. A. Kutty *et al.*, “5G networks towards smart and sustainable cities: A review of recent developments, applications and future perspectives,” *IEEE Access*, Dec. 2021.
- [141] J. Zhang, A. A. Glazunov, W. Yang *et al.*, “Fundamental wireless performance of a building,” *IEEE Wireless Commun.*, vol. 29, no. 1, pp. 186–193, Feb. 2022.

- [142] J. Zhang, A. A. Glazunov, and J. Zhang, “Wireless performance evaluation of building layouts: closed-form computation of figures of merit,” *IEEE Trans. Commun.*, vol. 69, no. 7, pp. 4890–4906, Apr. 2021.
- [143] Y. Yao, Y. Shao, J. Zhang *et al.*, “A transparent antenna using metal mesh for UWB MIMO applications,” *IEEE Trans. Antennas Propag.*, Feb. 2023.
- [144] Y. Yao, Y. Shao, and J. Zhang, “UWB MIMO optical transparent antenna based on ITO film,” *IEICE Electron. Expr.*, vol. 20, no. 5, pp. 20 230 022–20 230 022, Mar. 2023.
- [145] Z. Liu, S. Liu, X. Zhao *et al.*, “Wideband gain enhancement and RCS reduction of Fabry–Perot antenna using hybrid reflection method,” *IEEE Trans. Antennas Propag.*, vol. 68, no. 9, pp. 6497–6505, Apr. 2020.
- [146] Z. Liu, S. Liu, B. Bian *et al.*, “Metasurface-based low-profile high-gain substrate-integrated Fabry–Pérot cavity antenna,” *Int. J. RF Microwave Comput.*, vol. 29, no. 4, p. e21583, Apr. 2019.
- [147] C. Mateo-Segura, A. P. Feresidis, and G. Goussetis, “Bandwidth enhancement of 2-D leaky-wave antennas with double-layer periodic surfaces,” *IEEE Trans. Antennas Propag.*, vol. 62, no. 2, pp. 586–593, Nov. 2013.
- [148] H. Jiang, Z. Xue, W. Li *et al.*, “Low-RCS high-gain partially reflecting surface antenna with metamaterial ground plane,” *IEEE Trans. Antennas Propag.*, vol. 64, no. 9, pp. 4127–4132, Jul. 2016.
- [149] P. Xie, G. Wang, H. Li *et al.*, “Circularly polarized Fabry–Perot antenna employing a receiver–transmitter polarization conversion metasurface,” *IEEE Trans. Antennas Propag.*, vol. 68, no. 4, pp. 3213–3218, Apr. 2020.
- [150] Y. Zheng, J. Gao, Y. Zhou *et al.*, “Wideband gain enhancement and RCS reduction of Fabry–Perot resonator antenna with chessboard arranged metamaterial superstrate,” *IEEE Trans. Antennas Propag.*, vol. 66, no. 2, pp. 590–599, Feb. 2018.

- [151] I. Yoo and D. R. Smith, “Dynamic metasurface antennas for higher-order mimo systems in indoor environments,” *IEEE Wireless Commun. Lett.*, vol. 9, no. 7, pp. 1129–1132, Jul. 2020.
- [152] R. Cicchetti, V. Cicchetti, A. Faraone *et al.*, “A compact high-gain wideband lens vivaldi antenna for wireless communications and through-the-wall imaging,” *IEEE Trans. Antennas Propag.*, vol. 69, no. 6, pp. 3177–3192, Jun. 2021.
- [153] I. Goode and C. E. Saavedra, “Millimeter-wave beam-steering antenna using a fluidically reconfigurable lens,” *IEEE Trans. Antennas Propag.*, vol. 69, no. 2, pp. 683–688, Feb. 2021.
- [154] R. Xu and Z. N. Chen, “A hemispherical wide-angle beamsteering near-surface focal-plane metamaterial Luneburg lens antenna using transformation-optics,” *IEEE Trans. Antennas Propag.*, vol. 70, no. 6, pp. 4224–4233, Jun. 2022.
- [155] X.-M. Zheng, Y.-F. Liu, and L. Peng, “A millimeter-wave lens antenna with flat-top radiation pattern based on hybrid optimization algorithm,” in *2022 IEEE 9th International Symposium on Microwave, Antenna, Propagation and EMC Technologies for Wireless Communications (MAPE)*. IEEE, Aug. 2022, pp. 240–243.
- [156] N. T. Nguyen, R. Sauleau, and L. Le Coq, “Reduced-size double-shell lens antenna with flat-top radiation pattern for indoor communications at millimeter waves,” *IEEE Trans. Antennas Propag.*, vol. 59, no. 6, pp. 2424–2429, Jun. 2011.
- [157] J. Li, C. He, H. Fan *et al.*, “Gain-equalized multibeam antenna fed by a compact dual-layer rotman lens at Ka-band,” *IEEE Trans. Antennas Propag.*, vol. 70, no. 3, pp. 2307–2311, Mar. 2022.
- [158] Q. Liao, N. J. Fonseca, M. Camacho *et al.*, “Ray-tracing model for generalized geodesic lens multiple beam antennas,” *IEEE Trans. Antennas Propag.*, Mar. 2023.
- [159] J. R. Saberlin and C. Furse, “Challenges with optically transparent patch antennas,” *IEEE Antennas Propag. Mag.*, vol. 54, no. 3, pp. 10–16, Jun. 2012.

- [160] E. H. Lim and K. W. Leung, “Transparent dielectric resonator antennas for optical applications,” *IEEE Trans. Antennas Propag.*, vol. 58, no. 4, pp. 1054–1059, Apr. 2010.
- [161] Z. N. Chen, D. Liu, H. Nakano *et al.*, *Handbook of antenna technologies*. Springer Publishing Company, Incorporated, Sep. 2016.
- [162] P. Piksa, S. Zvanovec, and P. Cerny, “Elliptic and hyperbolic dielectric lens antennas in mmwaves,” *Radioengineering*, vol. 20, no. 1, pp. 270–275, Apr. 2011.
- [163] Y.-X. Zhang, Y.-C. Jiao, and S.-B. Liu, “3-D-printed comb mushroom-like dielectric lens for stable gain enhancement of printed log-periodic dipole array,” *IEEE Antennas Wirel. Propag. Lett.*, vol. 17, no. 11, pp. 2099–2103, Nov. 2018.
- [164] E.-S. Jo and D. Kim, “3-D printer based lens design method for integrated lens antennas,” *IEEE Antennas Wirel. Propag. Lett.*, vol. 17, no. 11, pp. 2090–2093, Nov. 2018.
- [165] F. Scattoni, M. Ettorre, R. Sauleau *et al.*, “Optimization procedure for planar leaky-wave antennas with flat-topped radiation patterns,” *IEEE Trans. Antennas Propag.*, vol. 63, no. 12, pp. 5854–5859, Dec. 2015.
- [166] C. Chen, B. Zhang, and K. Huang, “Nonuniform Fabry–Perot leaky-wave antenna with flat-topped radiation patterns for microwave wireless power transmission,” *IEEE Antennas Wirel. Propag. Lett.*, vol. 18, no. 9, pp. 1863–1867, 2019.
- [167] C. Wang, Y. Chen, and S. Yang, “Dual-band dual-polarized antenna array with flat-top and sharp cutoff radiation patterns for 2G/3G/LTE cellular bands,” *IEEE Trans. Antennas Propag.*, vol. 66, no. 11, pp. 5907–5917, Nov. 2018.
- [168] M. K. Emara, T. Tomura, J. Hirokawa *et al.*, “All-dielectric Fabry–Pérot-based compound Huygens’ structure for millimeter-wave beamforming,” *IEEE Trans. Antennas Propag.*, vol. 69, no. 1, pp. 273–285, Jan. 2021.

- 
- [169] A. Monti, A. Alù, A. Toscano *et al.*, “Surface impedance modeling of all-dielectric metasurfaces,” *IEEE Trans. Antennas Propag.*, vol. 68, no. 3, pp. 1799–1811, Mar. 2020.
- [170] Z. L. Ma, K. B. Ng, C. H. Chan *et al.*, “A novel supercell-based dielectric grating dual-beam leaky-wave antenna for 60-GHz applications,” *IEEE Trans. Antennas Propag.*, vol. 64, no. 12, pp. 5521–5526, Dec. 2016.